

DAMAGE BEHAVIOR OF GLASS FIBER REINFORCED PLASTIC
LAMINATE AND BOVINE-DERIVED HYDROXYAPATITE UNDER
LOW-VELOCITY IMPACT LOADING

SADJAD NADERI

THESIS SUBMITTED IN FULFILLMENT
OF THE REQUIREMENTS
FOR THE DEGREE OF DOCTOR OF PHILOSOPHY

FACULTY OF ENGINEERING
UNIVERSITY OF MALAYA
KUALA LUMPUR

2015

UNIVERSITI MALAYA

ORIGINAL LITERARY WORK DECLARATION

Name of Candidate: **SADJAD NADERI** (I.C/Passport No: **I95755943**)

Registration/Matric No: **KHA110029**

Name of Degree: **DOCTOR OF PHILOSOPHY (PhD)**

Title of Project Paper/Research Report/Dissertation/Thesis ("this Work"):

DAMAGE BEHAVIOR OF GLASS FIBER REINFORCED PLASTIC LAMINATE AND BOVINE-DERIVED HYDROXYAPATITE UNDER LOW-VELOCITY IMPACT LOADING

Field of Study: **MECHANICAL ENGINEERING**

I do solemnly and sincerely declare that:

- (1) I am the sole author/writer of this Work;
- (2) This Work is original;
- (3) Any use of any work in which copyright exists was done by way of fair dealing and for permitted purposes and any excerpt or extract from, or reference to or reproduction of any copyright work has been disclosed expressly and sufficiently and the title of the Work and its authorship have been acknowledged in this Work;
- (4) I do not have any actual knowledge nor do I ought reasonably to know that the making of this work constitutes an infringement of any copyright work;
- (5) I hereby assign all and every rights in the copyright to this Work to the University of Malaya ("UM"), who henceforth shall be owner of the copyright in this Work and that any reproduction or use in any form or by any means whatsoever is prohibited without the written consent of UM having been first had and obtained;
- (6) I am fully aware that if in the course of making this Work I have infringed any copyright whether intentionally or otherwise, I may be subject to legal action or any other action as may be determined by UM.

Candidate's Signature

Date

Subscribed and solemnly declared before,

Witness's Signature

Date

Name:

Designation:

ABSTRACT

Modeling and simulation of mechanical behavior of biomaterials is a very important topic. Until now, there is no single simulation model valid for the wide range of biomaterial, which includes metal alloys, composite and porous materials. Therefore the objective of the present study is to develop a numerical model to cover evaluation of mechanical properties for two types of brittle biomaterials: hydroxyapatite (HA) as a porous material for hard tissue replacement and Glass Fiber Reinforced Plastic laminates (GFRPs) as a layered composite for dental applications. The plastic behavior of HA and the effect of porosity on the elastic-plastic behavior of HA have not been well studied and fully discovered. On the other hand, biomedical and industrial applications have focused to detect the effect of low-velocity impact on mechanical response of GFRP materials under fatigue loading.

Finite element simulation models have been developed using MSC. MARC[®] to study on mechanical response of these brittle materials under impact and nanoindentation. The FE-inverse technique and semi-empirical method was introduced to infer the most suitable elastoplastic material model for HA. In addition, an effective approach is proposed to design irregular porous media using MATLAB code for HA with controllable pore shapes and distributions, without requiring any prior microscopic information. The impact damage process and contact stiffness for GFRP samples were investigated incrementally until when the composites were perforated. A Fatigue Damage index (FD) was introduced to capture the unique GFRP composite characteristics. Nanoindentation on HA and low-velocity impact, tensile static and fatigue tests on GFRP were performed to verify the numerical methods.

The elastic-plastic material model has shown more reasonable mechanical behavior of HA. Proposed approach for generating irregular porous structures is easier and faster

than the other existing approaches and constructed model appears more natural and realistic. The influence of low-velocity impact should be reflected in the design of GFRP structures. Even by increasing laminate thickness, the effect of impact is higher than the effect of thickness on the fatigue behavior of glass/epoxy laminates.

ABSTRAK

Pemodelan dan simulasi kelakuan mekanik bahan bio adalah satu topik yang sangat penting. Sehingga kini, tidak ada model simulasi tunggal sah untuk pelbagai jenis biobahan, yang merangkumi aloi logam, komposit dan bahan-bahan berliang. Oleh itu, objektif kajian ini adalah untuk membangunkan satu model berangka untuk meliputi penilaian sifat-sifat mekanik untuk dua jenis bahan bio rapuh: hydroxyapatite (HA) sebagai bahan berliang untuk penggantian keras tisu dan Glass Fiber Reinforced Plastic laminates (GFRPs) sebagai komposit berlapis untuk aplikasi gigi. Kelakuan plastik HA dan kesan keliangan pada tingkah laku elastic-plastic HA belum dikaji dengan baik dan ditemui sepenuhnya. Sebaliknya aplikasi bioperubatan dan perindustrian telah memberi tumpuan untuk mengesan kesan-kesan halaju rendah kepada sambutan mekanik bahan GFRP di bawah pembebanan keletihan.

Model simulasi unsur terhingga telah dibangunkan dengan menggunakan MSC. MARC® untuk belajar kepada sambutan mekanikal bahan-bahan rapuh di bawah kesan dan nanoindentation. Teknik FE-songsang dan kaedah separa empirik telah diperkenalkan untuk membuat kesimpulan model bahan anjal-plastik yang paling sesuai untuk HA. Juga pendekatan yang berkesan adalah dicadangkan untuk mereka bentuk media berliang tidak teratur menggunakan kod MATLAB untuk HA dengan bentuk liang dikawal dan pengagihan, tanpa memerlukan apa-apa maklumat mikroskopik terlebih dahulu. Proses rosak akibat dan ketegangan hubungan untuk sampel GFRP telah disiasat secara berperingkat sehingga apabila komposit telah berlubang. A indeks Kerosakan Keletihan (FD) diperkenalkan untuk menangkap unik ciri-ciri komposit GFRP. Nanoindentation pada HA dan kesan-halaju rendah, tegangan statik dan keletihan ujian ke atas GFRP telah dijalankan untuk mengesahkan kaedah berangka.

Model bahan elastic-plastic telah menunjukkan tingkah laku mekanikal lebih munasabah HA. Pendekatan yang dicadangkan untuk menjana struktur berliang yang tidak teratur adalah lebih mudah dan lebih cepat daripada pendekatan lain yang sedia ada dan model dibina kelihatan lebih semula jadi dan realistik. Pengaruh berimpak halaju rendah harus dicerminkan dalam reka bentuk struktur GFRP . Walaupun dengan meningkatkan ketebalan lamina, kesan kesan adalah lebih tinggi daripada kesan ketebalan ke atas tingkah laku lesu bagi laminates glass/epoxy.

ACKNOWLEDGEMENT

“He who taught by the pen, taught man that which he knew not” 4-5, Sura 'Alaq (The Clot) No. 96. Thank you, Lord, for helping and protecting me.

My dear supervisors, Prof. Dr. Mohsen, and Dr. Bushroa, thank you for your full support, fruitful and deep discussion and guidance throughout my PhD research work. Thank you for showing me routes to success, such as applying numerical and analytical methods in biomaterials. I feel that I could never sufficiently acknowledge your impact on my life.

My gratitude also goes to the center of advanced manufacturing and material processing (AMMP), its members, and staff for their support.

Last not the least; Countless and special thanks go to my mother in Iran, who have supported and motivated me morally and financially. My special thanks extend to my beloved brother, who has been always there and motivated me. So that I would stay on a straight path and pursue my goal. Thanks to Dr. Reza Mahmoudian, Dr. Ali Dabbagh, Dr. Sadjad Jamalpour and all the people and friends who have assisted me.

TABLE OF CONTENTS

ABSTRACT.....	II
ABSTRAK.....	V
ACKNOWLEDGEMENT	VII
TABLE OF CONTENTS	VIII
LIST OF TABLES	XIII
LIST OF FIGURES	XIV
LIST OF SYMBOLS AND ABBREVIATIONS	XX
CHAPTER 1: INTRODUCTION	1
1.1 General Background	1
1.2 Problem Statement.....	2
1.3 Motivation	3
1.4 Importance of porous structure	4
1.4.1 Biomaterials.....	7
1.4.2 Energy absorbers.....	8
1.4.3 Lightweight structures.....	8
1.4.4 Thermal insulators	9
1.4.5 Electrode of fuel cells	9
1.4.6 Filters	9
1.5 Objectives and basic ideas of this work.....	10
1.6 Scope of the present investigation.....	11

1.7 Layout of the thesis.....	11
CHAPTER 2: LITERATURE REVIEW.....	13
2.1 Introduction	13
2.2 Mechanical properties of HA	13
2.3 Background on porous structures	15
2.3.1 Unit cell based approach	16
2.3.2 Function based approach.....	16
2.3.3 Computational design approach	17
2.3.4 Mechanical properties of porous structure	17
2.4 Low-velocity impact on GFRP	19
2.5 Aim of the present work	22
CHAPTER 3: METHODOLOGY	24
3.1 Materials	24
3.1.1 HA powder preparation.....	24
3.1.2 HA powder characterization.....	25
3.1.3 HA Sample preparation.....	32
3.1.4 Preparation of GFRP samples	32
3.2 Mechanical testing methods	33
3.2.1 Nanoindentation test	33
3.2.2 Impact test configuration.....	34
3.2.3 Tensile Static test	36
3.2.4 Fatigue loading	36

3.3 Evaluation of mechanical properties for HA	37
CHAPTER 4: FINITE ELEMENT SIMULATION AND MODELS FOR GFRP.....	41
4.1 FE simulation for low-velocity impact	41
4.2 Calculating the energy absorbed or dissipated for impacted laminate	42
4.3 Fatigue failure model for composite materials.....	44
4.3.1 The Broutman and Sahu Model.....	45
4.3.2 The Halverson Model.....	45
CHAPTER 5: FINITE ELEMENT MODEL FOR HA	47
5.1.1 Direct model for nanoindentation	47
5.1.2 Inverse FE model for nanoindentation (for given material properties.....	49
CHAPTER 6: POROUS STRUCTURE MODELING BASED ON CENTROIDAL VORONOI TESSELLATION.....	52
6.1.1 Introduction	53
6.1.2 A simple concept to generate irregular porous structure modeling	53
6.1 Centroidal Voronoi tessellation.....	54
6.1.1 Random aggregation model.....	55
6.1.2 A hybrid Voronoi tessellation and B-Spline based representation for pore shape and pore distribution modeling	56
6.2 Control of pore size	59
6.3 Boundary and edge control algorithm	61

6.3.1 Geometric model of 2D irregular porous structures	67
6.4 3D geometrical model for irregular porous structures.....	69
CHAPTER 7: RESULTS AND DISSCUSSION.....	72
7.1 Introduction	72
7.2 Hardening parameters for HA	72
7.2.1 Force displacement curves	73
7.2.2 Mesh deformation	76
7.2.3 Effect of sintering temperature on σ - ϵ curves	77
7.2.4 Effect of sintering temperature on hardening parameters	79
7.3 Effect of porous geometry on indentation of HA.....	81
7.3.1 Topologies and porosities for 2D	82
7.3.2 2D finite element analysis of nanoindentation on a porous HA sample..	84
7.3.3 Results of a 3D HA porous solids.....	88
7.4 Impact induced damage and failure modes in GFRP samples	92
7.4.1 Force-deflection diagram	92
7.4.2 Force-time diagram.....	101
7.4.3 Deflection-time diagram	104
7.4.4 Velocity-time diagrams	105
7.4.5 Velocity-deflection diagram.....	107
7.4.6 Energy-time diagram.....	110
7.4.7 Energy absorption versus number of layers	112

7.5 Effect of damage on residual tensile properties of GFRP	114
7.6 The Effects of Impact Energy and Thickness on Fatigue Life of GFRP samples	116
7.7 Modification of the failure criteria of GFRP under low-velocity impact .	117
7.8 Effective stress-strain correlation with damage index	119
7.9 Effective failure criteria based on damage index	121
7.10 S-N Curve.....	122
CHAPTER 8: CONCLUSION AND SUGGESTION FOR FURTHER WORK.....	124
8.1 Conclusion	124
8.2 Suggestions for further work.....	128
REFERENCES.....	129
LIST OF PUBLICATIONS	150
Published Papers	150
Related Published Paper	150
Papers in Review Process	150
Paper to be submitted soon	151

LIST OF TABLES

Table 1.1. The typical applications and advantages of porous artifacts.	7
Table 3.1. Peaks position of HA powder and HA JCPDS 9-432.	28
Table 3.2. Geometrical properties and number of layers.	32
Table 6.1. The characteristics and advantages of hexagons in porous structure design.	54
Table 6.2. An analogy of physical/chemical polymerization and the nature inspired counter- part.....	56
Table 7.1. Work hardening parameters of hydroxyapatite at different sintering temperatures as calculated from the semi-empirical model.	73
Table 7.2: Hardening parameters determined by the inverse technique for 2D and 3D models	73
Table 7.3: Bending stiffness for different thickness (in parentheses an amount of k_b per number of layers)	96
Table 7.4: Lamina stiffness and strength properties of GFRP (Hosseinzadeh et al., 2006).	123

LIST OF FIGURES

Figure 2.1. Classification of porous structure design approaches based on the previous literatures.....	15
Figure 3.1. The microstructure of raw bovine bone after heating at 900 °C for 2 h shows numerous pores and few small pores.	25
Figure 3.2. XRD pattern of bovine HA obtained from heated bovine bone at 900 °C shows that this material is highly crystalline and correspond to the characteristic peak of HA (JCPDS No. 9-432).....	26
Figure 3.3. FTIR spectra of HA obtained from heated bovine bone at 900 °C shows characteristic of IR spectroscopy of HA.	29
Figure 3.4. Bovine-driven HA particle size distribution shows that the average size of the powder used in this research was between 45 µm and 150 µm.	30
Figure 3.5. Scanning electron micrograph of bovine HA powder exhibiting the irregular particles shape.....	30
Figure 3.6. X-ray diffraction pattern of bovine HA sintered for 2 h at (a) 1000 °C; (b)1100 °C; (c) 1300 °C; (d) 1400 °C (∇ =TTCP).....	31
Figure 3.7. The intensity of the three main peaks of HA as a function of sintering temperature.....	31
Figure 3.8. The stacking sequence for GFRP laminates.	33
Figure 3.9. Geometry of Berkovich indenter with 65.3° angle according to ISO 14577.	34
Figure 3.10. Fixtures and locations of samples under fixture.	35
Figure 3.11. The schematic of the drop-weight machine.....	36

Figure 3.12. Composite plate location between the fixtures of the fatigue test machine.	37
Figure 4.1. Finite element model with 12647 solid elements.	42
Figure 4.2. Estimating absorbed energy from a typical impact response of a composite laminate (David-West et al., 2008).	44
Figure 5.1. Finite element mesh for the Berkovich indentation test and solid structure: (a) 2D model, (b) 3D model.	48
Figure 5.2. Effect of mesh size on the force-displacement curves obtained by incremental displacement solution method for: (a) 2D model, and (b) 3D model.	49
Figure 5.3. Outline of the inverse FE technique to determine the plastic properties of HA from nanoindentation experimental data.	51
Figure 5.4. Procedure to determine the hardening parameters through a force displacement curve using nanoindentation data and inverse finite element technique.	52
Figure 6.1. Examples of irregular porous structures. (a) and (b) are adapted from (Sirivithayapakorn et al., 2003; Wong et al., 2007) respectively.	54
Figure 6.2. A ‘minimum-length’ connection of random points in a plan	55
Figure 6.3. Voronoi diagram and B-Spline curves fitted from Voronoi polygon vertices.	58
Figure 6.4. Different orders of B-Spline curves and the control polygon.	59
Figure 6.5. Modeling increased pore interstices using scaled control polygons. (a) Scale factor $t = 1.0$; (b) Scale factor $t = 0.8$; (c) Scale factor $t = 0.6$.	60
Figure 6.6. Cell attributes association and concave pore modeling. (a) A Voronoi diagram with no attributes associated. (b) Each cell is randomly associated with an integer attribute, represented with a fill color. (c) A zoomed view of three Voronoi	

polygons to be merged. (d) Adjacent same-attributed Voronoi polygons are merged to form a bigger polygon. (e) The fitted B-Spline curves and their control polygons. Note that the cell attribute of the merged cell shown in (d) may not be exactly the same as the attributes of the child cells in (b), and attributes are used only for classification purposes..... 65

Figure 6.7. Scaling of convex polygons and closed B-Spline fitting. (a) The down-scaled point set is not a subset of the original point set. (b) The proposed polygon shrinking scheme. (c) A problematic case of using naive scaling operation. (d) The desired increment of pore interstices. 66

Figure 6.8. An irregular porous structure model. (a) The control polygons used for B-Spline curve fitting. (b) The pore geometries represented by B-Spline curves. (c) Boolean subtraction of the pores from the external geometry and the resultant 2D representation of the irregular porous structure..... 69

Figure 6.9. Different extruded 2D porous layers (a, b, c and d) and merging layers (e) to generate 3D structure implemented to finite element analysis for Berkovich nanoindentation problem on HA model. 71

Figure 7.1. Force displacement curves obtained from the nanoindentation test of HA and finite element analysis; material parameters are based on Table 7.2 for different sintering temperatures, 1000, 1100, 1200, 1300 and 1400°C in 2D and 3D..... 76

Figure 7.2. (a) AFM image of indented sample, (b) FE deformed mesh for 3D model. 77

Figure 7.3. Equivalent stress-strain responses of the different sintered hydroxyapatite extracted from 2D and 3D numerical analyses in comparison with the formula ($\sigma = K\epsilon^n$). 79

Figure 7.4. (a) Elastic modulus E and average values of K, (b) average n value versus sintering temperature for the hydroxyapatite samples. 81

Figure 7.5. Porous structures with different topologies. (a) An irregular porous structure with many concave-shaped pores, the model is constructed with 150 generator points are randomly associated with the Voronoi cells. (b) An irregular porous structure with many convex shaped pores, the model is constructed with same 150 generator points are randomly associated with the Voronoi cells.....	83
Figure 7.6. Porous structures with different porosities. (a) A porous structure modeled with the scaling factor $t = 0.4$. (b) A porous structure modeled with the scaling factor.....	83
Figure 7.7. Microstructure of fracture surfaces of porous HA samples sintered at (a) 1000 °C, (b) 1100 °C (c) 1200°C and 1300 °C (d) (Goller et al., 2006).	84
Figure 7.8. FE model of a designed irregular porous structures for different point generators (a) $n=10$, (b) $n=20$, (c) $n=30$ and (d) $n=40$	85
Figure 7.9. Equivalent Von Mises stress distribution [MPa] for indented HA sintered at 1200°C 2D models for different point generators, (a) $n=10$, (b) $n=20$, (c) $n=30$, (d) $n=40$ and (e) $n=0$ (non-porous).	87
Figure 7.10. Effect of porosity on predicted force-displacement curves obtained from 2D finite element analysis of indentation (HA material properties at 1200 °C and n , number of point generator).....	88
Figure 7.11. Equivalent Von Mises stress distribution [MPa] on the top surface and at the end of indentation (left), and maximum load/depth (right) for HA sintered at 1200°C 3D models for (a) porous and (b) solid geometries.....	91
Figure 7.12. Expected stress-strain curve of the central point in indentation zone obtained from FE-model for solid and porous HA model.	92
Figure 7.13: F-d diagrams for impact energies of 9.8 and 19.6 J on samples with thicknesses of: (a) 2mm, and (b) 3 mm.	94

Figure 7.14: Photographs of front and back surfaces of the impacted samples with 2mm thickness after impact with different impact energy and damage propagation values in the 45° direction in woven fiber laminate. (a) Initial energy=9.8 J, and (b) Initial energy=19.6 J.	95
Figure 7.15: Photographs of the front and back surfaces of impacted samples with 3mm thickness after impact with different impact energy and damage propagation values in the 45° direction in woven fiber laminate. (a) Initial energy=9.8 J, and (b) Initial energy=19.6 J.	97
Figure 7.16: F-d graph for sample with 4 mm thickness and impact energy: (a) 9.8 J, (b) 19.6 J, and (c) 29.4 J.	98
Figure 7.17: Photographs of front and back surface of the impacted samples with 4 mm thickness after impact with different impact energy and damage propagation values in the 45° direction in woven fiber laminate. (a) Initial energy=9.8J, (b) Initial energy=19.6J and (c) 29.4 J.....	99
Figure 7.18: F-d diagram in loading phase with impact energy of 9.8J for: (a) 2mm, (b) 3mm, and (c) 4mm thickness.....	100
Figure 7.19: Experimental force-time curve for different impact energies and thicknesses: (a) 2 mm, (b) 3 mm, and (c) 4 mm.	102
Figure 7.20: FE-simulation results for force-time curve under different impact energies and thicknesses: (a) 2 mm, (b) 3 mm, and (c) 4 mm.	103
Figure 7.21: Maximum contact force–banding stiffness for Glass/Epoxy laminate for impact energies of 9.8 J and 19.6 J.....	104
Figure 7.22: Variation of deflection versus time under different impact energies for the samples with different thickness: (a) 2 mm, (b) 3 mm, and (c) 4 mm.	105

Figure 7.23: Variation of velocity versus time under different impact energies for the samples with different thicknesses: (a) 2 mm, (b) 3 mm, and (c) 4 mm.	106
Figure 7.24: Velocity-time diagram for the samples with different thicknesses: (a) 2 mm, (b) 3 mm, and (c) 4 mm; (follow-up of curve is estimated).	109
Figure 7.25: Ratio of return velocity to initial velocity versus plate thickness for different impact energies.	110
Figure 7.26: Curve of the transferred energy to the composite specimens versus time for different sample thicknesses: (a) 2 mm, (b) 3 mm, and (c) 4 mm.	111
Figure 7.27: The schematic of K-t Curve for 2 mm perforated specimen by 19.6 J impact energy.	113
Figure 7.28: Absorption energy respect to ratio of initial impact energy to number of layers.	113
Figure 7.29. Typical failures in GFRP laminates for tension static and fatigue tests...	115
Figure 7.30: Number of cycles to fracture to initial impact energy for different GFRP laminate thicknesses.	116
Figure 7.31: Specimen life varies with thickness for different initial impact energy values.	117
Figure 7.32: FD slope variations to impact energy for different thicknesses.	118
Figure 7.33: The stress-fatigue life curve for woven E-glass/epoxy with 2mm thickness.	123

LIST OF SYMBOLS AND ABBREVIATIONS

Symbols and Abbreviation	Description
$^{\circ}\text{C}$	Degrees Celsius
E_a	Absorbed Impact Energy
E_e	Elastic Impact Energy
E_i	Initial Impact Energy
\bar{E}	Reduced Elastic Modulus
F_a	Normalized Applied Load
F_{exp}	Experimental Impact Force
F_r	Normalized Residual Strength
G_{ext}	External Geometry of An Object
K_b	Bending Stiffness
R^m	m-Dimensional Space
v_0	Initial velocity
v_r	Return Velocity
X_r	Residual Strength
ε_y	Yield Strain
σ_{eff}	Effective Stress
σ_y	Yield Stress
\backslash	Boolean Subtraction
2D	Two Dimension
3D	Threes Dimension
AMMP	Center of Advanced Manufacturing & Material Processing
C	Curvature
CAD	Computer-Aided Design
CT	Computed Tomography
d	Displacement
D	Damage Parameter
E	Elasticity Modulus
F	Force

FD	Fatigue Damage
FE	Finite Element
FEA	Finite Element Analysis
FEM	Finite Element Model
FTIR	Fourier Transform Infrared
GFRP	Glass Fiber Reinforced Plastic
H	Hardness
h	Indentation Depth
HA	Hydroxyapatite
ISO	International Organization for Standardization
K	Strength Coefficient
KE	Kinematic Energy
MRI	Magnetic resonance imaging
n	Hardening Exponent
N	Number of Load Cycle to Fatigue Failure
S	Fatigue Stress
SAXS	Small-Angle X-ray
SEM	Scanning Electron Microscopy
X	Initial Static Strength
XRD	X-Ray Diffraction
ε	Strain
ρ	Density
σ	Stress
Ω	Porous Structure

CHAPTER 1:INTRODUCTION

1.1 General Background

Hard tissue replacement materials and synthetic bone are widely considered owing to the lack of autograft materials and health risks posed by allograft. Hydroxyapatite is the dominant inorganic phase in natural bone. Synthetic hydroxyapatite particles, film, coating, fiber and porous skeleton are used broadly. HA has been extensively investigated recently due to its chemical and structural similarities to naturally occurring biological apatite in hard tissues. The main weakness of HA is that its mechanical properties are not as good as bone tissue, particularly the plastic behavior. Nonetheless, HA has a much higher elastic modulus (~ 120 GPa (Suchanek et al., 1998)) than bone (<30 GPa for trabecular bone (Zysset et al., 1999)). Besides, HA is known as a brittle material while bone shows significant plastic behavior (Bembey et al., 2006; Mercer et al., 2006).

Structural components manufactured from fiber-reinforced plastic are increasingly used in situation where high strain loading is present. The relative importance and increasing demand for composites in the aircraft industry illustrated that the next generation of military and civil aircraft structures are likely to be made from composites. The behavior of GFRP composites under high strain loading such as impact, slam etc is more complex than monolithic materials because of the factors that influence the damage mechanism, which include the fiber material, matrix material, volume fraction, fiber orientation, moisture content, porosity, strain rate etc. Composites are generally used because they have desirable properties. Although the continuous fiber laminate is used expensively, the potential for delamination or separation of the

laminate, is still a major problem because the interlinear strength is matrix dominated. This sensitivity to damage is often a handicap in structural applications.

Composite structural elements are now used in a variety of components for biomedical, automotive, aerospace, marine and architectural structures. Composites applications in commercial aircraft have been steadily increasing as material cost comes down, as design and manufacturing technology evolves, and as the experience in composites technology continues to increase. Recently GFRP is used clinically in posts for orthopedic implant applications and root canals. Although the mechanical properties of GFRP posts are important not only for their durability but also for the prevention of root fractures (Inami et al., 2015; Kaur et al., 2012; Latour et al., 1993; Naumann et al., 2012; Pereira et al., 2013). Due to a combination of strength and modulus, the majority of fiber-reinforced and laminated composite materials are either equivalent to or better than traditional metallic materials. Owing to their low densities, the specific strength and modulus of these composite materials seem to be significantly superior to those of metallic materials. Besides, the fatigue strength-to-weight ratio, as well as fatigue damage tolerance of many composite laminates, is excellent.

1.2 Problem Statement

The large differences in elastic modulus between HA and bone, as well as lack of plastic ability of HA result in greater stress concentration and fracture at the bone-material interface. Furthermore, from a material properties point of view, the elastoplastic behavior of HA remains unknown, including various hardening parameters and how to identify them. These factors define the mechanical behavior of HA and they are important to a material for bone substitution.

The application of composite materials in industrial structures is projected to increase over the next couple of decades. The dynamic mechanical behavior of

composite materials is considered one of the most important properties by structural engineers. For instance, plastic behavior and damage under low-velocity impact can possibly ensue during production, maintenance, repair, or the lifetime of structural composite components. A number of factors which can seriously damage composites include tool drop, flying debris, foreign object damage, etc. However, damage from low-velocity impact is not visible to the naked eye but may affect the material's residual mechanical properties. The residual strength has been considered for the damage composite materials.

1.3 Motivation

This study is motivated to cover different aspects of macro-mechanical properties of two common brittle biomaterials, HA and GFRP as a porous and layered materials respectively. Recently, HA has been frequently used for tissue replacement since it is compatible with in-vivo environment, which includes chemical, mechanical and morphological conditions in addition to the biological and physiological considerations. GFRP composites have been also extensively used in dental applications due to their higher strength and lower weights compared to metal structures.

Therefore damage behavior, static and dynamic response of GFRP composites under low-velocity impact and cyclic loading; and the mechanical properties of bovine-derived HA porous bone graft under nanoindentation receive great attention of research.

An effective numerical model was developed to evaluate mechanical response of the brittle biomaterials. An elastic-plastic material model was presented for HA considering an irregular porous geometry in order to characterize the plastic behavior. The typical types of low-velocity impact damages in GFRP composites are mainly caused during production, repair, maintenance, or by particle crashes during function, and collisions between different structures. Impact damages reduce the residual strength of the

composites significantly, hence combination of low-velocity impact and fatigue loading is required to be investigated. The mechanical behavior and damage mechanisms of GFRP composites were characterized using different curves and the developed fatigue damage parameter.

The present research has done under Center of Advanced Manufacturing and Material Processing (AMMP). AMMP Centre is a leading research center in the University of Malaya specializing in areas of precision manufacturing, machining technology, material processing and biomaterial developments. The materials, which are investigated in this study, are considered by AMMP Center in order to research and find the mechanical behavior of them.

1.4 Importance of porous structure

Porous structures are a particular type of solids, where a large number of pores, either regular or irregular shaped, separate or interconnected, uniform or randomly distributed, exist in the geometric domain of interest.

A porous structures can be modeled clumsily with classical solid modeling techniques. Besides the available classical models reveal generally different features from the porous structures in real. Classical solid modeling requires a complete representation of the physical solid objects and is focused on the shape and spatial relations of the assembly parts (Requicha et al., 1982), while also the internal structure of porous model need to be considered.

The difference between porous structure modeling and solid object modeling is the structure heterogeneities where voids are formed. The structure heterogeneity of porous structures brings many problems in modeling.

First, a porous structure has many pores its inside how each pore can be identified with the location, pore size, shape and spatial relations with its neighborhood. Large

memory spaces are needed for data storage. Wettergreen et al. (Wettergreen et al., 2005b) created a porous object by packing 1008 polyhedron blocks repetitively. The assembly of the entire 1008 building blocks was beyond the computer's ability and left it unfinished. Although computing power is now abundant, the large number of pores still presents a big challenge for computing efficiency consideration.

Second, although regular porous structures are easier to model and evaluate, irregular porous structures perform better in terms of representation reliability and design freedom. In some representations like unit cells (Chantarapanich et al., 2012; C.-M. Cheah et al., 2004; Gomez et al., 2007; Sun et al., 2005; Wettergreen et al., 2005b), porous structures are assumed to be homogeneous or regular to avoid this difficulty. This representation simplifies the structure heterogeneity and reduces the modeling difficulty, but also leads to simplified properties.

Third, the mechanical, physical, thermal and other properties of porous structures are concerned with not only materials but also structures. Take for example the Young's modulus, in a solid it is an inherent property and can be calculated by:

$$E = \frac{\sigma}{\varepsilon} \quad \text{Eq. 1.1}$$

where E is the Young's modulus; σ and ε are the stress and strain in the elastic portion of the stress-strain curve of the material.

Gibson and Ashby (Gibson et al., 1997) concluded that the effective Young's modulus of an open-cell porous structure is dependent on the Young's modulus of the solid material and the relative density of the structure,

$$\frac{E^*}{E_s} = C \left(\frac{\rho^*}{\rho_s} \right)^2 \quad \text{Eq. 1.2}$$

where E^* is the effective Young's modulus of the porous structure; E_s is the Young's modulus of the solid material; ρ^* is the density of the porous structure; ρ_s is the density of the solid material and C is a constant.

In this study, the method is proposed to generate irregular pores considering these three problems. However, research on porous structures is not only about porous geometry but it has a long history where some applications were recorded. Table 1.1 lists the typical applications and advantages of porous artifacts. The low density of porous structures makes them suitable to be used as materials in tissue engineering. The large deformation under certain stress is an excellent property for porous structures to be used as energy absorbers. The absorbers can transfer more kinetic energy into deformation energy compared to dense solid objects. The large surface areas also facilitate porous structures being widely adopted in applications where surface reactions and adsorptions are important.

Recently many researchers have been interested on porous structures and this is mainly because of many unique and excellent properties that porous structures possess. For instance, porous structures have lower density, lower thermal conductivity, lower stiffness, lower strength, larger compressive strain and larger surface areas than many solid components (Gibson et al., 1997; Scheffler et al., 2006). These represent proper properties for design purposes and overcome the weaknesses of most traditional solid objects.

Table 1.1. The typical applications and advantages of porous artifacts.

Applications	Utilized properties
Tissue scaffolds	Low stiffness, large surface area, good interconnectivity
Tissue implant materials	Low stiffness, low density
Energy absorbers	Low strength, large compressive strains
Lightweight design materials	Low density
Thermal insulators	Low thermal conductivity
Electrode in fuel cells	Large surface area
Filters	Large surface area, various pore size

Porous structures can be used in special applications which general solid materials are not able to be employed. The porous applications can be categorized into different fields such as biomaterials, energy absorber, lightweight structures, thermal insulators, electrode of fuel cells and filters. In the following sections they are introduced.

1.4.1 Biomaterials

Porous structures are usually used as scaffolds (Hollister, 2009; Leong et al., 2008; Meyer et al., 2009; Sun et al., 2004; Sun et al., 2002) and tissue implant materials (Enab et al., 2013; Guillén et al., 2011; Murr et al., 2011; Shen et al., 2011; Singh et al., 2010) in tissue engineering. Scaffolds mainly provide temporary support in human body and they will biodegrade as new tissues regenerate (Chen et al., 2011). When porous structures act as tissue implant materials, they will function as the replaced tissue, thus scaffolds and implant materials play different roles in human body.

Providing temporary mechanical support and enhancing mass transfer and cell attachment (Hollister, 2009; Hutmacher et al., 2004) are the main functions of a scaffold. Scaffolds should provide mechanical support before and during the new tissue

regeneration. Moreover the transportation of waste and nutrition is dependent on the highly porous scaffold.

In tissue implants, porous structures can improve the high stiffness problem caused by solid metallic implants and make the implants more harmonious with tissues surrounded (Shen et al., 2011). The Young's modulus of an implant is a critical design consideration and the porous material whose Young's modulus matches the bone most should be selected to avoid stress shielding (Jacobs et al., 1993).

1.4.2 Energy absorbers

Porous structures are considered for energy absorbers due to their low strength, large compressive strain and low relative density (Gibson et al., 1997). The porous energy absorber converts the kinetic energy into its deformation energy. Dynamic crushing test and continuous load test are usually verify the energy absorption capacity (Ajdari et al., 2011a; Ajdari et al., 2011b; Ali et al., 2008; Li et al., 2012). Pore distributions, pore shapes and pore irregularities all have influences on the energy absorption capacity.

In addition to kinetic energy absorption, porous materials also absorb sound and the sound is converted into heat and transmitted. The aircraft engine noise abatement problem (Raj, 2011) is an application where porous materials act as sound absorbers.

1.4.3 Lightweight structures

Porous materials have relative low density compared to solids with the same materials. The low weight per volume ratio makes porous materials highly suitable for aircraft and vehicle design where weight is strictly controlled (Banhart, 2005). The porous structures such as sandwich panels and honeycombs (Crupi et al., 2013; Huber et al., 2009) are used as supernormal cores in product design as they offer high stiffness with low weight. In vehicle design, metal foams attract much attention and are

extensively used due to their good thermal, sound and vibration absorption abilities (De Giorgi et al., 2010).

1.4.4 Thermal insulators

Polymeric, glass and ceramics foams are used widely in thermal insulation materials because of their low thermal conductivities (Ashby, 2006; Barrios et al., 2013; Bourret et al., 2013). Porosity, cell size and temperature all affect the thermal conductivity of porous materials in complicated ways (Gibson et al., 1997). When porous materials act as thermal insulators, the low solid volume fraction, small pore size and other factors all control heat flow in foams and prevent heat transforming (Gibson et al., 1997).

1.4.5 Electrode of fuel cells

Being the electrode of fuel cells is a new application of porous materials. In order to improve the performance characteristics of fuel cells, porous carbon is adopted as the electrode (Chang et al., 2007; Krishnamurthy et al., 2011). The high surface area per volume ratio of porous structures increases the attachment surface of the electrodes and improves the reaction efficiency. The porous carbon can be designed as both regular periodic porous structures and irregular porous structures (T.-W. Kim et al., 2006).

1.4.6 Filters

Porous structures also function as filters to separate particles in one phase from the other one by a physical operation. Sandstone is a natural filter for water cleaning and activated carbon is a good air purifier. The filtration process makes use of the complex porous structures. The various pore sizes, large surface areas and long flow path interpose the pass of oversized particles and enhance the attachment of unwanted components.

1.5 Objectives and basic ideas of this work

The main goal in this thesis is to present numerical models, which are able to characterize mechanical behavior of brittle biomaterials. HA as a porous ceramics and GFRP as a layered composite are investigated to cover different aspects of macro-mechanical properties of brittle materials.

Elastic-plastic material model for HA, which is obtained from numerical and analytical techniques, and the irregular porous geometry, which is generated by a mathematical code, are implemented to the simulation. Nanoindentation tests on HA are simulated for solid and porous geometry, afterward the effect of porosity can be evaluated.

Validation methods for predicting composite behavior under impact and fatigue load are essential if the engineer is to have the confidence to use models of damage development in design. The failure event in a composite structure is in fact determined by the progressive occurrence and interaction of some or all of the many micro-mechanisms of damage.

Computer-Aided Design (CAD) plays an important role in modeling, partly due to the advanced manufacturing technology (Abdelaal et al., 2013; Derby, 2012) that transforms the complex CAD models into valid products. The easy manipulation and friendly user interaction make CAD the superior choice in porous structures modeling.

The main objectives of this thesis are:

- To present an analytical method to identify the nonlinear elastoplastic mechanical properties of HA.
- To develop a representational model of porous structures without any existing object, which is both morphologically and functionally efficient.

- To find the relationship between the solid and porous structures and corresponding properties through finite element analysis.
- To describe the behavior of GFRP laminates under low-velocity with parameters including bending stiffness, impact force, impact energy, impact velocity and deflection during and after the impact.

1.6 Scope of the present investigation

This investigation was conducted to determine the mechanical behavior of composites (layered GFRP laminate) and ceramic (hydroxyapatite). Based on the equipment in AMMP Center, different mechanical tests including low-velocity impact, nanoindentation, fatigue loading and tensile static tests were chosen to discover the mechanical responses of these materials.

Several reasons caused to use analytical and numerical methods besides of experiments. In order to decrease cost and save time, the finite element models and semi-empirical method were employed to predict the elastic-plastic parameters of HA. Moreover the dynamic response of GFRP composites was investigated using finite element analysis. The conjunction of experimental and numerical method concluded to deduction of the cost in preparation of the sample and number of tests, also time of collection data was reduced significantly.

1.7 Layout of the thesis

The outline of thesis is as follows. The opening chapter introduces the importance of the study on hydroxyapatite and glass-fiber reinforced plastic composites, besides the problems that need to be resolved. Chapter 2 covers a background into various state of matter. It provides a brief review of mechanical properties of HA, porous structure and low-velocity impact on layered composite materials. Chapter 3 represents an overview of the experimental methods adopted in the study, the characterization numerical and analytical techniques, as well as finite element methods, geometry model of porous

structure used. Alternative semi-empirical method is also presented in this chapter. Chapter 4 primarily concerns finite element simulation and models for GFRP. Chapter 5 elaborates the direct and inverse finite element model for HA. Chapter 6 explains the method to create porous geometry and structure. A profound result illustration and a discussion of the obtained products are presented in Chapter 7. Finally, Chapter 8 concludes and provides recommendations for possible areas of new work in the future.

CHAPTER 2:LITERATURE REVIEW

2.1 Introduction

The current chapter contains a brief review of existing works on mechanical properties of HA, porous structure, and low-velocity impact damage on GFRP, plus fatigue behavior of impacted composites.

2.2 Mechanical properties of HA

A general study has been performed on the mechanical properties of HA, including elastic modulus, hardness and strength. Ab-initio technique was implemented to calculate the elastic constant and carry out a theoretical tensile experiment on stoichiometric hydroxyapatite crystal (Ching et al., 2009). The deformation behavior was studied using structural analysis under various levels of tensile strain. Several attempts have been made to find the connection between porosity, elastic properties and fracture strength of sintered HA (Kumar et al., 2005; Metsger et al., 1999). To the best of our knowledge, however, proper micromechanical analysis of the effective elastoplastic properties has never been done; the shape of the pores was either unnoticed or assumed to be ideally spherical (Kumar et al., 2005). A research was performed on the role of microstructure and porosity on the mechanical behavior of sintered hydroxyapatite (He et al., 2008). Also the effect of cell number, size and density on the mechanical behavior of polymer foam has been studied (Yetkin et al., 2013). Work was only done experimentally to observe the porous influence and it was concluded that porous microstructure produces HA with plastic deformation properties. The dependence of the mechanical properties of sintered hydroxyapatite on sintering temperature was discussed (Prokopiev et al., 2006). The problem was clarified by

concentrating on the elastic modulus, compression strength and micro structure of sintered hydroxyapatite on processing temperature. However, the previous work has been done on hardening parameters for alloy (Findik, 2012) but for HA the identification of elastic and plastic parameters remains unsolved. It is useful to consider sintering process of the powder base material to determine the influence over mechanical properties (Gökçe et al., 2011). Generally, research has focused on elastic properties; consequently, the plastic area and actual microstructure of sintered HA is still unknown.

Compared with mechanical properties tests, the nanoindentation technique is an appropriate means of characterizing nanomechanical properties. A number of analysis approaches based on experimental and analytical research have been directed at many materials to extract the mechanical properties from the nanoindentation load-displacement curve. During loading, the typical load-displacement response generally follows the relation described by Kick's law, that is, $P = Ch^2$ where P is the indentation load, h is the measured indentation depth and C is the curvature of load displacement curve during loading. Based on Kick's law, mechanical properties are obtained from measured force-displacement curves, such as elastic modulus, yield strength, strain hardening, residual stress and creep behavior (Ahn et al., 2001; Cheng et al., 1998; Cheng et al., 2002; Herrmann et al., 2006; Warren C Oliver et al., 2004). In this study, a semi-empirical method which means involving assumptions, approximations, or generalizations designed to simplify calculation or to yield a result in accord with observation. This method is implemented to extract the hardening parameters from the measured data set of load and displacement for Berkovich indentation for HA.

2.3 Background on porous structures

During the last decades, considerable approaches were put forward to model porous structure and these methods can be roughly classified into three categories, as shown in Figure 2.1.

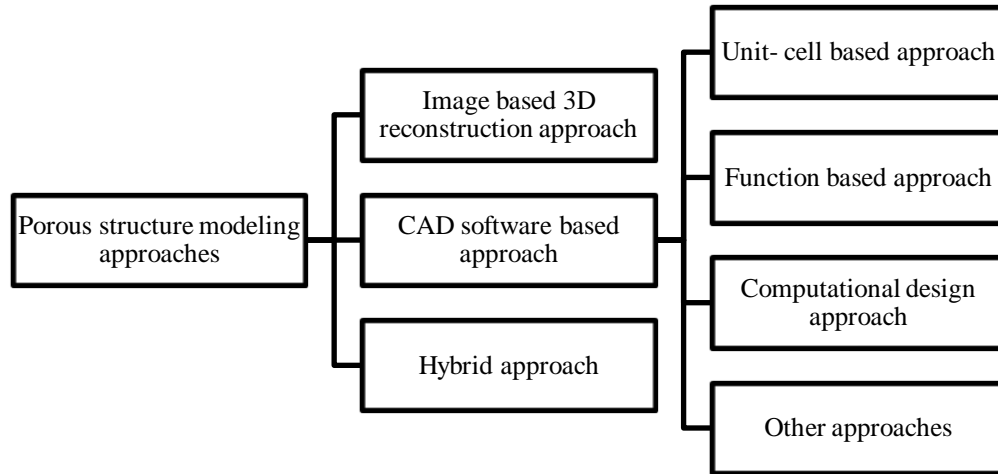


Figure 2.1. Classification of porous structure design approaches based on the previous literatures.

Image based 3D reconstruction approach is widely used in biomedical research (Vergés et al., 2008), (Starly et al., 2005). The foundation of this approach is image modalities including computed tomography (CT), magnetic resonance imaging (MRI), optical microscopy and micro CT (Sun et al., 2005). Applying these technologies, the existing porous object is scanned layer by layer and a 3D model is constructed in computer from the scanned 2D cross- sectional images after data processing. This method rebuilds the existing object at hand and mimics the porous structure in computer.

CAD software based approach does not need pre-existing objects and the modeling process is accomplished through computer software utilizing different theories and algorithms to represent the porous structure.

2.3.1 Unit cell based approach

In unit-cell based approach, feature primitive represented with specific geometry is first built and porous structures are created through repeated Boolean operations of the feature primitive. The feature primitive is called unit cell and various unit cells form a library. The key issue here is how the unit cells are built to represent the desired structure and match the corresponding properties. Gomez et al. (2007) described the unit cell informatics and characterization. Sun et al. (2005) designed a library of various unit cells by analogizing trabecular architectures found at different anatomical sites in the human skeleton. Some researchers (C. Cheah et al., 2003a, 2003b) created a unit-cell library with eleven polyhedrons which are selected from Platonic solids, Archimedean solids, prisms and antiprisms. Wettergreen et al. (2005) created a library containing two types of models, one is based on solid geometry with the inclusion of void spaces to create porosity and the other one is based on geometry of regular polyhedra. As Wettergreen et al. used two different methods to create porosity, Different geometry of unit-cells produced the stress discontinuities, therefore they solved the problem in the boundaries (using the concept of common interface).

2.3.2 Function based approach

In function based approach, the porous structure is described or controlled by functions. Yoo (2011) and Gabbrielli et al. (2008) proposed to represent porous structure using triply periodic minimal surfaces which are those with zero mean curvature and a crystalline structure. Cai et al. (2008) introduced to use a shape function which is computed when making a transformation between two different coordinate

systems. Irregular and deformed pore- making units are derived from regular basic units based on the shape function. Boolean difference is operated and irregular pores are removed from the solid. Pasko et al. (2011) used different periodic functions for modeling porous structures within the Function Representation. These functions serve to directly define the structure shape.

2.3.3 Computational design approach

In computational design approach, characteristics and properties related to the porous structure are formulated in a mathematical way so as to make a quantitative evaluation and prediction. Homogenization theory is commonly used in this approach especially in optimization design, which uses asymptotic expansion of relevant physical variables to generate multiscale equilibrium equations to compute the effective properties (Hollister, 2005). Adachi et al. (2006) built a model of scaffold degradation and new bone formation, and mechanical properties are formulated during the process. A three-dimensional computational simulation is conducted to evaluate the change of the mechanical properties and provides the desired function. Sanz-Herrera et al. (2009) used a mathematical approach to study factors such as stiffness, porosity and pore size, and predicted in vivo the rate of bone formation, scaffold degradation and the interaction between implanted scaffold and the surrounding bone.

2.3.4 Mechanical properties of porous structure

The most important mechanical properties are the yield strength and elastic modulus. Acharya et al. (2004) present a method to construct a simple and general site bond correlated 3D Hydraulic Pore Network model of hydraulic behavior of porous media for a wide range of permeability and porosity. Modeling porosity of biomaterials is critical for developing replacement bone tissues. Schroeder et al. (2005) uses this representation to develop an approach to modeling of porous, heterogeneous materials.

Zeleniakiene et al. (1969) investigated the stresses of 2D and 3D Representative Volume Element of porous polymer material. They compare the two models and evaluate the differences between them in the cases of various porosity modes. Komlev et al. (2006) investigated a highly porous hydroxyapatite scaffolds before the implantation and after they were seeded within vitro expanded bone marrow stromal cells (BMSC) and implanted for various numbers of weeks in mice. The methodologies revealed the applicable approaches to obtain mechanical properties of HA in the current study. Also the gap, which was required to be investigated. Helgason et al. (2008) compare the results from subject-specific finite element analysis of a human femur to experimental measurements, using two different methods for assigning material properties to the FE models. Teoh et al. (2008) survey the literature in the area of bone material properties and Needle/bone interaction in the context of needle placement. Vergés et al. (2008) described the methodology that they have designed to quantify the pores distribution in bone implants and the empirical results that they have obtained with CAD designed scaffolds, micro-CT and confocal microscopy data. They segmented the 3D images into three regions: exterior, bone and pore space. Next, they divide the pore space into pores and connection paths. Michailidis et al Michailidis et al) al. ,2010aMichailidis et al ; ,2010b(, introduced and facilitating the establishment of a FEM model corresponding to a solid geometry of open-cell foams for simulating the material behavior in micro-tension. Podshivalov et al. (2011) describes a new alternative for individualized mechanical analysis of bone trabecular structure. Guillén et al. (2011) studied compressive behavior of bovine cancellous bone and three open-cell metallic foams using mechanical testing, micro-focus computed tomography and finite element modeling. Ren et al. (2012) tested and evaluated mechanical properties changes of two hydroxyapatite ceramics induced by bone ingrowth were in a rabbit model. On the other words Both HA ceramics were implanted into the femoral condyles

of rabbits for the specified observation period (1, 5, 12, 24, and 48 weeks) in order to study on bone ingrowth.

2.4 Low-velocity impact on GFRP

Efforts to deal with the problem of damage propagation in laminated fiber reinforced plastic composites have been done by many investigators through the use of continuum damage mechanics. They tried to predict the influence of micro-scale defects and damage at a macro-scale using simplified assumptions for the damage and its effect on the mechanical properties (Ilyushin, 1973; Kachanov, 1986; Rabotnov, 1979). Many works have been made to introduce a micro-mechanical damage model applicable to a composite structure under loading and to evaluate certain damage characteristics within the model (Kiselev et al., 1990; Kondaurov, 1988).

Internal damage such as delamination and splitting of the surface of the samples, which is back of impacted-face, can reduce the residual strength of composite significantly. Delamination, fiber and matrix breakage are damages, which arise due to an impact energy event. This results in a reduction in stiffness and strength, also after low-velocity impact the damaged composites would be faced with different loading based on their application, in this condition the damage propagates. (Park et al., 2013). Hence the safe use of composites requires an understanding of impact damage intensity because of low-velocity impact. However, the dynamic behavior of composite laminates is very complex, because there are many concurrent phenomena during composite laminate failure under impact load. Therefore, it is very common to find research works about this issue at the literature, for example: Cairns et al. (1992); Farley et al. (1992); Haug et al. (1993); Belingardi et al. (1997); Collombet et al. (1997); Gottesman et al. (1997); Vicente et al. (2000); Kindervater et al. (2000); Kostopoulos et al. (2002); Tsamasphyros et al. (2013); Caprino et al. (1999); Naik et al. (2004); De Morais et al.

(2005); Mitrevski et al. (2005); Mikkor et al. (2006); Mamalis et al. (2006); Kim et al. (2007); Cho Zhao et al. (2007).

Recently, numerous researchers have been studying the impact effects on composite laminates. The investigations can be divided into three categories: (1) dynamic response of composite laminates, (2) contact mechanism in composite structures by impact load and (3) damage modes and failure in composites. Abrate (1991) presented a detailed contact mechanism and dynamic response of composite laminates under low-velocity impact. Other researchers have focused their studies on damage recognition, type and mode. Ross et al. (1973) analyzed the effects of impact exerted by conical head impactors and observed delamination in glass epoxy plates using a powerful light source. Chester et al. (1992) developed a delamination model of different fiber reinforced plates and showed that delamination always occurred in stretched form or almond shape. Evans et al. (1987) looked into how a toughened matrix could enhance the impact characteristics of epoxy composites, while Zhou et al. (2000) studied the damage resistance and tolerance of glass fiber-reinforced plates with a range of thicknesses. The damage of four different fiber-reinforced composite plates following standard drop weight impact at various impact energies was studied (Hosseinzadeh et al., 2006). All plates were modeled using ANSYS LS-DYNA under similar conditions to those from the real tests. They also calculated the threshold damage value for each composite. Tita et al. (2008) developed experimental and numerical approaches for failure analyses of thin composite laminates under low-velocity impact. Zhang et al. (2013) investigated Impact behaviors at low velocity of composite laminates reinforced with fabrics of different architectures.

Subsequent to earlier work on predicting the life of composite materials, Beheshty et al. (1999) came up with a new method. They demonstrated that a constant-life model is adequate for undamaged and damaged laminates. Mitrovic et al. (1999)

studied the effects of dynamical parameters and fatigue behavior of impacted composites, while the influence of thickness on the tension-compression fatigue behavior for carbon/epoxy was considered by Tai et al. (1999). The Weibull distribution function and median rank method were employed to predict the probability of failure, and a relationship was presented for the amount of stress and length of fatigue life. Symons et al. (2000) reflected on two amounts of damage, which had evident and barely evident damage impact. 5Hz frequency and $R=-1$ stress rate were applied for fatigue loading.

In recent decades, researchers including Yuanjian et al. (2007) have been exploring natural fibers as reinforcement for polymers by experimenting on the fatigue and impact behavior of these composites. A decrease in elastic modulus was detected during fatigue loading and its relationship was remarked from damage accumulation. Uda et al. (2009) found that the slope of the $S-N$ curve for undamaged samples was higher than for impacted laminates. The fatigue properties of various composite material types have reportedly been obtained since 1967 via many experimental studies. Based on results, empirical $S-N$ curves between stress and fatigue life have been derived - relationships which have been suggested for use in the design process (Harris et al., 1996). Both linear and nonlinear $S-N$ curves have been proposed with respect to experimental results (Joseph et al., 1994; Mao et al., 2002; Nicholas, 1995; Yang, 1978). A nonlinear curve between strain and fatigue life can also predict the fatigue life of composite materials (Halford et al., 1993; Reifsnider et al., 2000; Subramanian et al., 1995). A linear relationship between maximum stress S and the logarithm of N , or the number of load cycles to fatigue failure, is widely utilized to fit experimental data as given by Eq. 2.1:

$$S = m \log N + b \quad \text{Eq. 2.1}$$

where m and b are parameters related to the material's properties.

Another relationship is considered in Eq. 2.2:

$$k_1 S^{k_2} N = 1 \quad \text{Eq. 2.2}$$

where k_1 and k_2 are constant from experiments. m and b are depended on material properties and they are changed with different materials. m , b , k_1 and k_2 are obtained from fatigue test and $S - N$ curve.

With the predicted fatigue life under constant cyclic loading, fatigue damage can be evaluated after a given number of cycles through a fatigue damage accumulation model, which is discussed in chapter 4. The composite is assumed to fail when the accumulated damage exceeds a critical level.

2.5 Aim of the present work

The aim in this research is to develop a model to investigate on mechanical behavior of brittle biomaterials. Macro-mechanical properties of HA as a porous material and Mechanical response of GFRP as a layered material under dynamic loading are studied.

A relationship for damage evaluation with respect to impacted and non-impacted GFRP laminates. This work shows an experimental, analytical and numerical investigation of the low-velocity impact on thin composite laminates plates of epoxy resin reinforced (matrix) by woven E-glass fiber (reinforcement). The low-velocity impact besides fatigue behavior of glass fiber-reinforced composites with impact energies up to 19.86J for different thicknesses is presented.

What this study is trying to address is to propose a geometric representation to model such irregular porous structure, and to design such artifacts from a constructive perspective from scratch. Instead of designing a faithful copy from 3D reconstruction, the proposed method does not require any pre-existing models, yet it can generate generically similar structures with irregular pore shapes and distributions.

The effective mechanical properties of porous structure are dependent on the porosity parameters of the solid material. Finite element method is utilized to analyze stress distribution in porous media for HA to investigate the effect of porosity on mechanical behavior.

In the present study, the mechanical behavior of bovine hydroxyapatite is investigated using Berkovich nanoindentation to obtain the hardening parameters. An inverse analysis besides an analytical method process is presented to identify the nonlinear elastoplastic mechanical properties, followed by validation with existing experimental data. The aim of the work is to characterize the elastoplastic behavior of HA to be used in a multi-scale modeling framework to predict the mechanical response of artificial or natural hard tissue. The target is to obtain accurate mechanical behavior in comparison with the previous works for HA.

CHAPTER 3: METHODOLOGY

3.1 Materials

In this research two brittle biomaterials, which are porous and layered composite, are chosen to investigate. First, Hydroxyapatite is nowadays considered a useful biocompatible material. Second GFRP as a composite laminates have high stiffness, high strength and low density, which are used extensively in structural applications. In the next section, the preparation of HA and GFRP samples will be explained.

3.1.1 HA powder preparation

Initially, bovine samples were supplied from a local slaughterhouse. The macroscopic adhering impurities and material were removed from the cortical bone in order to clean away any ligaments and tissue from the sample. The acquired bones were boiled in distilled water, and they were then dried in the sun to eliminate organic matter and collagen. A defatting process was implemented so that soot would not form in the heating step. A hacksaw was used to cut the samples into small pieces of 10×10×5mm. The cut, rectangular bones were heated for 2 hours in air at 900°C at a heating rate of 5°C/min, the microstructure changes due to the removal of the water (around 9 wt.%) and organic contain such as collagen (around 20 wt.%), proteins, polysaccharides, and lipids that are also present in small quantities as shown in Figure 3.1. With slow furnace cooling the samples returned to room temperature. A mortar pestle and sieve were employed to obtain HA powder. Only HA powder with particle size less than 400 µm was used in this study due to have higher green strength because of mechanical interlocking during green body samples preparation or compaction process (German, 1984).

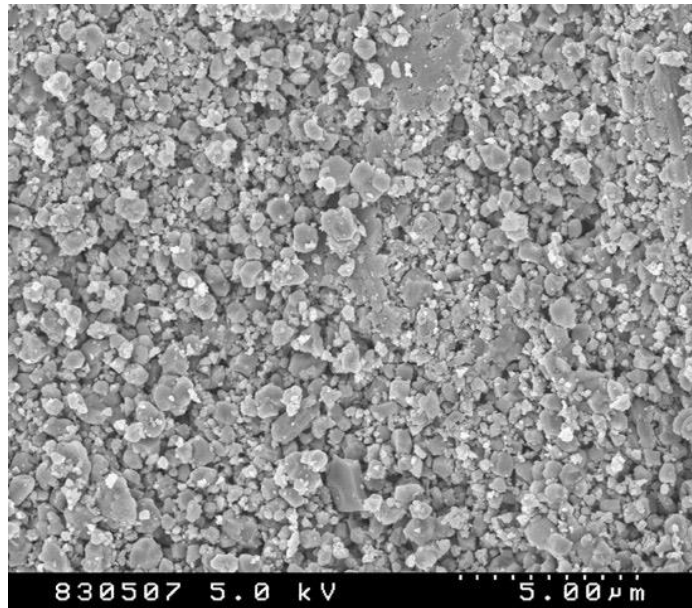


Figure 3.1. The microstructure of raw bovine bone after heating at 900 °C for 2 h shows numerous pores and few small pores.

3.1.2 HA powder characterization

X-ray diffraction with a monochromated CuK α radiation model XRD 6000 Shimadzu was used to analyze the hydroxyapatite phases. Scanning speed and step were adjusted to 7°/min and 0.02° respectively. The Fourier transform infrared (FTIR) spectrum of the powder was identified with a Nicolet Avatar 360 FTIR spectrometer. The powder and KBr were mixed before FTIR analysis, and then they were pressed into pellets. During these processes, a scanning electron microscope (SEM: Hitachi S4200B) was used to test the bone samples and HA powder morphology. The samples were mounted on steel stub pins and afterward coated with palladium (Pd) using a sputter coater (E1030 Ion Sputter, Hitachi) in order to make a conducting layer and avoid charging in the microscope. The screening method (sieve shaker machine, Retsch AS200) was chosen to analyze the distribution of bovine HA powder particles. Screens were stacked starting with 20 μ m, to 45 μ m, 150 μ m and 300 μ m for screening analysis (the smallest opening size was placed at the bottom). 300 gr of the powder was placed on top of the screen stack, which was vibrated for 60 min. Subsequent to vibration, the

powder in each size space was weighed and the interval percent was estimated for every size fraction. The particle size data points were mapped on a particle size distribution histogram.

The XRD pattern of the bovine HA powder is shown in Figure 3.2 within the 2θ range from 20° to 50° . The well resolved XRD peaks of BHA could be easily indexed on the basis of hexagonal crystal system of space group $P6_3/m$ (Jcpds File No. 9-432 (Hydroxyapatite), 1988) with respect to JCPDS file no. 9-432. The Bragg peaks at ~ 21 , 22, 25, 28, 31, 32, 34, 35, 39, 41, 43, 45, 46, 48 and 49° (2θ) observed for bovine HA corresponded to the characteristic peaks of stoichiometric HA (JCPDS 9-432). XRD analysis also indicated the absences of secondary phases, such as TCP or calcium oxide (CaO). Thus, it can be said that BHA powder production method resulted in high crystallinity and single phase HA and is also believed to be pure HA as indicated by the peak of the diffraction patterns (JCPDS 9-432).

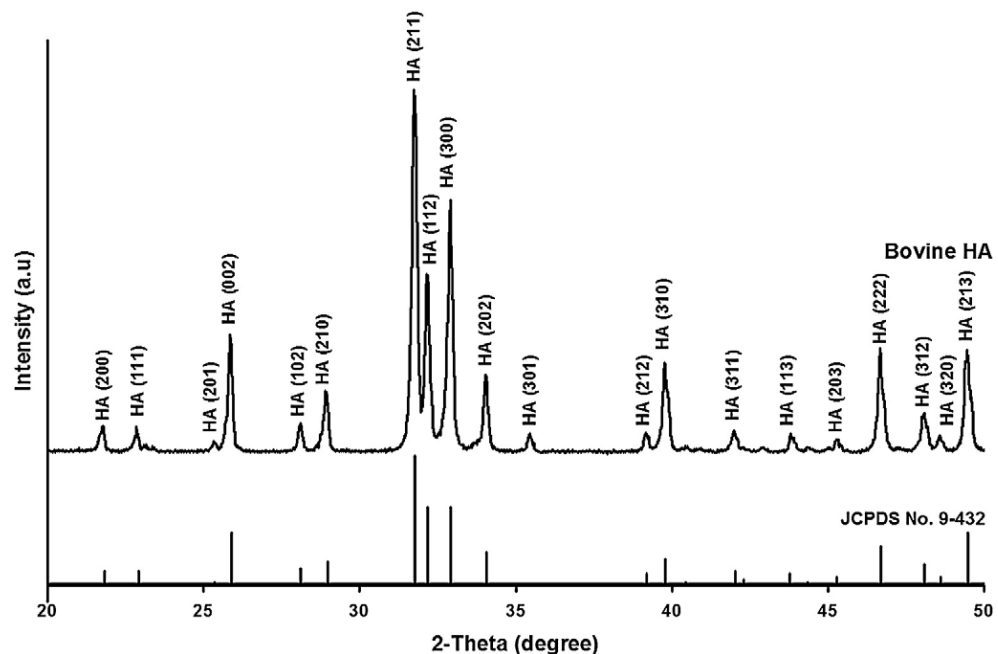


Figure 3.2. XRD pattern of bovine HA obtained from heated bovine bone at 900°C shows that this material is highly crystalline and correspond to the characteristic peak of HA (JCPDS No. 9-432).

The XRD pattern of the apatite has been indexed on the basis of hexagonal structure and the lattice parameters obtained by the standard least-squares refinement of the diffraction lines. Wang and Chaki reported that the dehydroxylation phenomenon could also be observed by simply comparing the XRD position of the sintered material with that of the standard JCPDS data for stoichiometric HA (P.E. Wang et al., 1993). Table 3.1 presents the position of XRD peaks of bovine HA powder which corresponds to the plane (211), (300) and (202). The three main peaks are very similar in position. It indicates that the heated bovine bone is of hydroxyl carbonate apatite, which is beneficial for biomedical purposes due to its similarity with the bone apatite.

Table 3.1. Peaks position of HA powder and HA JCPDS 9-432.

Bovine HA		Plane			JCPDS 9-432	
2-Theta	d	h	k	l	2-Theta	d
21.760	4.0810	2	0	0	21.819	4.0701
22.840	3.8904	1	1	1	22.902	3.8800
25.320	3.5147	2	0	1	25.354	3.5101
25.840	3.4451	0	0	2	25.879	3.4400
28.120	3.1708	1	0	2	28.126	3.1701
28.900	3.0869	2	1	0	28.966	3.0801
31.760	2.8152	2	1	1	31.733	2.8141
32.160	2.7811	1	1	2	32.196	2.7780
32.900	2.7202	3	0	0	32.902	2.7200
34.040	2.6317	2	0	2	34.048	2.6311
35.440	2.5308	3	0	1	35.48	2.5281
39.280	2.2918	2	1	2	39.204	2.2961
39.780	2.2642	3	1	0	39.818	2.2621
41.980	2.1504	3	1	1	42.029	2.1481
43.860	2.0625	1	1	3	43.804	2.0650
45.280	2.0011	2	0	3	45.305	2.0000
46.680	1.9443	2	2	2	46.711	1.9431
48.080	1.8909	3	1	2	48.103	1.8900
48.580	1.8726	3	2	0	48.623	1.8710
49.460	1.8413	2	1	3	49.468	1.8410

The XRD analysis of HA powder confirms to the FTIR result as shown in Figure 3.3. The IR spectrum of bovine HA shows only the characteristic absorption peaks of HA. A large number of bands in the spectra (3570.91, 3440.24, 2076.38, 1993.10, 1459.73, 1413.12, 1101.13, 633.68, and 568.91 cm^{-1}) match the bands in the HA reference

spectrum and are in agreement with literature data on HA (Jinawath et al., 2002; Joschek et al., 2000; Murugan et al., 2002).

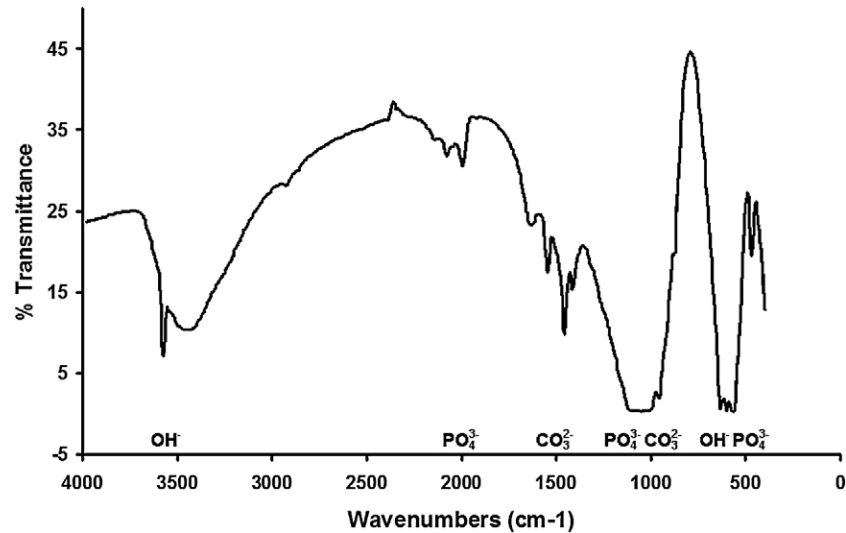


Figure 3.3. FTIR spectra of HA obtained from heated bovine bone at 900 °C shows characteristic of IR spectroscopy of HA.

The absorption peaks at 3570.91 and 633.68 cm^{-1} may be due to the presence of hydroxyl (OH^-) group of HA. The FTIR spectra also indicate the presence of phosphate (PO_4^{3-}) and carbonate (CO_3^{2-}) ions in the heated bovine bones. Results show that IR spectrum of the HA sample shows a major peak at $\sim 630 \text{ cm}^{-1}$ and $\sim 3570 \text{ cm}^{-1}$ due to the presence of the hydroxyl group. The intensity bands at about 1410 cm^{-1} and 1450 cm^{-1} in the spectrum of bovine HA powder are attributed to components of the ν_3 mode of a trace amount of CO_3^{2-} and $\nu_2 \text{ CO}_3^{2-}$ band at about 875 cm^{-1} .

The particle sizes distribution of HA powder after crushing using mortar and pestle is shown in Figure 3.4. The graph shows a broad range of particle sizes distribution. The average particle size was between 45 μm and 150 μm . There is also presence of irregular particles shape as shown in Figure 3.5. The irregular morphology of HA powder can give a higher green strength (the interparticle bonds that form due to

compaction) because of mechanical interlocking during green body samples preparation or compaction process (German, 2005).

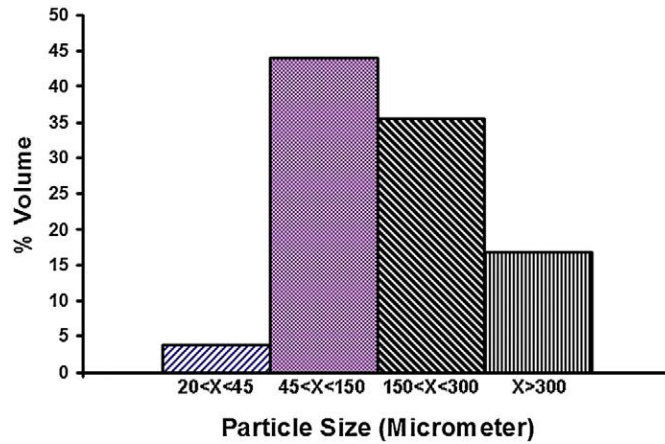


Figure 3.4. Bovine-driven HA particle size distribution shows that the average size of the powder used in this research was between 45 μm and 150 μm .

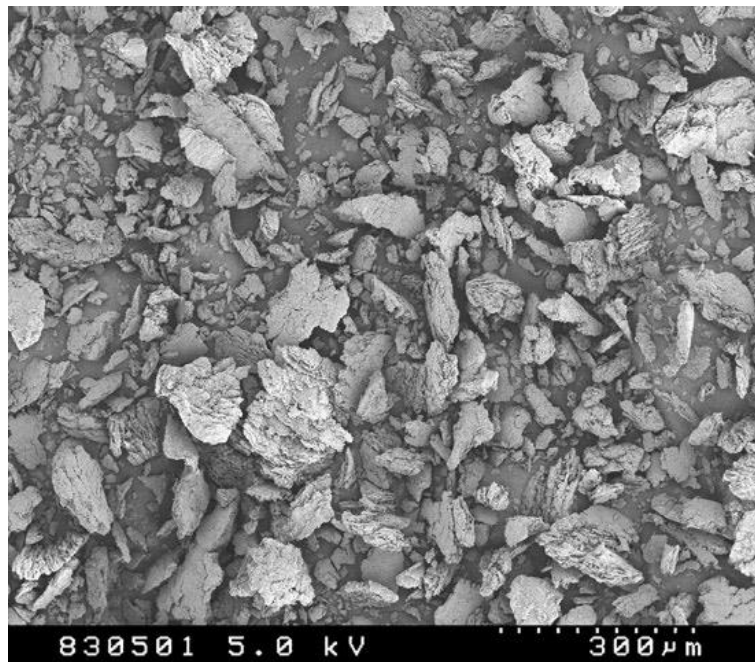


Figure 3.5. Scanning electron micrograph of bovine HA powder exhibiting the irregular particles shape.

3.1.3 Phase stability

Figure 3.6 shows the XRD plots of HA specimens sintered at 1000, 1100, 1300 and 1400 $^{\circ}\text{C}$. Those XRD results show that the intensity of major peaks of sintered HA at 1000, 1100, 1300 and 1400 $^{\circ}\text{C}$ decreases with increasing sintering temperature which

may indicate decomposition of HA. Ooi et al. and Toque et al. reported that the HA may decompose to α -TCP (alpha TCP), β -TCP (beta TCP), and T-TCP (tetra TCP) (Herliansyah et al., 2009; Ooi et al., 2007). The comparison of the three major peaks of BHA (i.e. the (h k l) of (2 11), (3 0 0) and (1 1 2)) sintered at 1000, 1100, 1300 and 1400 °C is depicted in Figure 3.7.

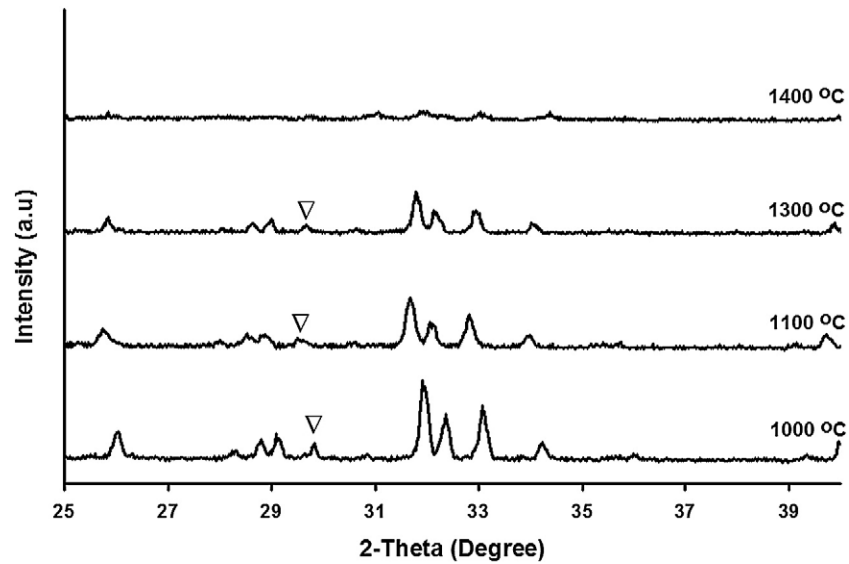


Figure 3.6. X-ray diffraction pattern of bovine HA sintered for 2 h at (a) 1000 °C; (b) 1100 °C; (c) 1300 °C; (d) 1400 °C (▽=TTCP).

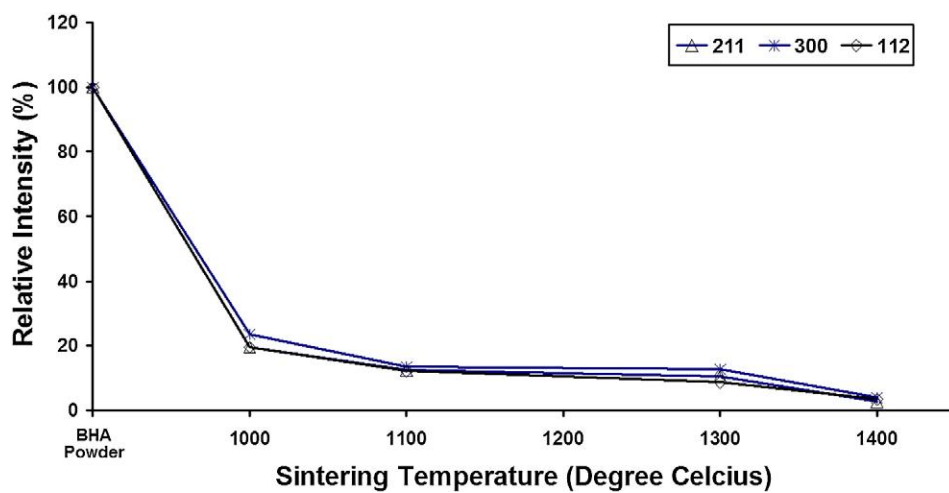


Figure 3.7. The intensity of the three main peaks of HA as a function of sintering temperature.

3.1.4 HA Sample preparation

Using 20 mm cylindrical dies, the HA powder was compacted uniaxially at 156 MPa to form green bodies, which were then sintered in air atmosphere with no pressure at different temperatures, 1000, 1100, 1200, 1300, and 1400°C, at a furnace ramp rate of 5°C/min and 2 hours dwelling time. The disk-shaped HA samples were 3 mm thick and 10 mm in diameter.

3.1.5 Preparation of GFRP samples

In this investigation, the composite samples are woven E-glass/epoxy. The area density of E-glass fibers is 400gr/m². The provided resin is epoxy and the specimens were fabricated via hand-layup method. The fibers are cross-ply and their direction is [0/90°] in each layer. The laminated samples are square plates of 12cm×12cm. The geometrical properties and number of layers in the experimental samples are summarized in Table 3.2, while Figure 3.8 illustrates the stacking sequences.

Table 3.2. Geometrical properties and number of layers.

Fabric Material	Area Density (gr/m ²)	Length (cm×cm)	Thicknesses (Number of Layers)		
E-glass	400	12×12	2 mm (3)	3mm (5)	4mm (6)

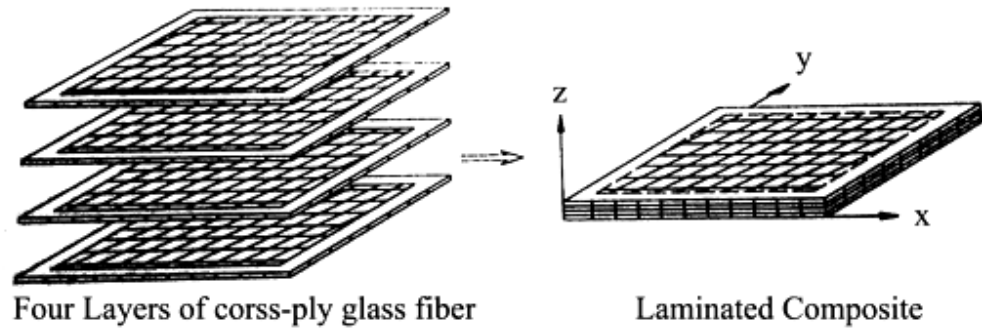


Figure 3.8. The stacking sequence for GFRP laminates.

3.2 Mechanical testing methods

In this research various experiments are considered to characterize mechanical behavior of the materials. In following the methods used in mechanical tests will be represented.

3.2.1 Nanoindentation test

Indentation experiments were performed with a nanoindentation machine (Triboscope system, Hysitron Inc., USA). ISO 14577 standard was followed for the nanoindentation test. A calibrated Berkovich indenter was used with included angle (α) 65.03° and radius of tip curvature of 150 nm, as shown in Figure 3.9. Diamond was used for the indenter with elastic modulus of 1140 GPa and Poisson's ratio of 0.07. The maximum indentation depths at which material properties become almost constant in the nanoindentation test were obtained with different maximum loads for different samples. For the HA samples at 1100 to 1400°C sintering temperatures, the maximum indentation load was equal to 4 mN to reach a maximum indentation depth of 150 nm. For the HA sample sintered at 1000°C, this depth was obtained by applying a load of 1.5 mN. At least five indentations were made at each load level on each sample. Poisson's ratio can be assumed a constant value of 0.2 in numerical analysis for ceramics (Warren Carl Oliver et al., 1992a). The indentation force was applied for 30,

10 and 30 seconds for loading, holding and unloading respectively, with a constant speed.

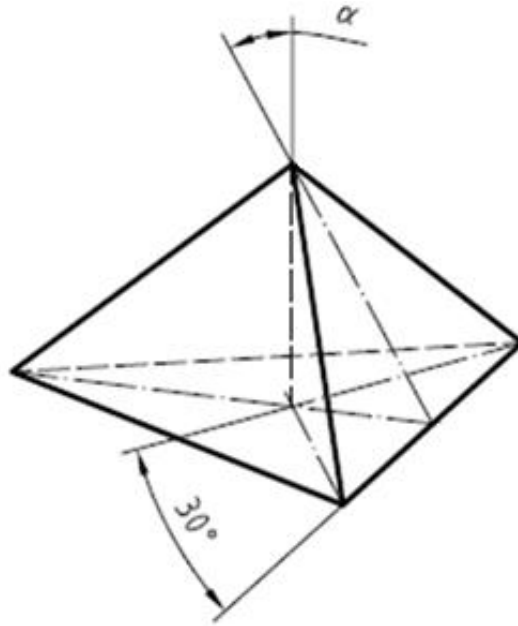


Figure 3.9. Geometry of Berkovich indenter with 65.3° angle according to ISO 14577.

3.2.2 Impact test configuration

Low-velocity impact tests were performed in a purpose-built, drop-weight impact rig by altering both drop height and impactor weight however in this investigation the height is changed only. Samples to be impacted were clamped between two steel square plates and were organized as illustrated in Figure 3.10.

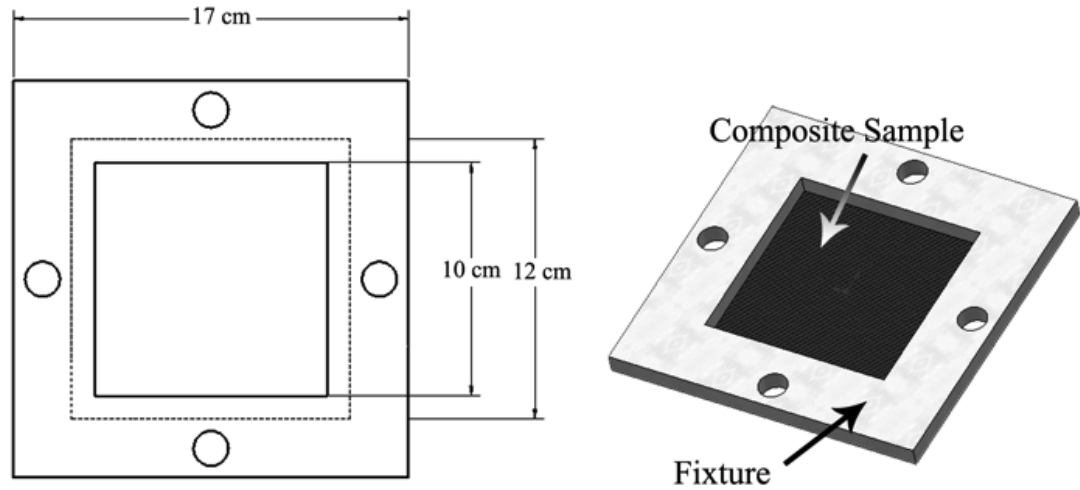


Figure 3.10. Fixtures and locations of samples under fixture.

Figure 3.11 shows a general schematic view of the drop-weight machine. According to ASTM D5628 (Weight et al., 2001), the impactor head is hemispherical and has a diameter of 12.7mm. The impactor is made of steel 4340, it is held and released using an electromagnet and gets captured after impact to prevent secondary strikes. The minimum height and weight of the impactor are 10cm and 7kg. Impact tests were performed at two initial impact energy levels, 9.8, 19.6 and 29.4 J. The initial impact energy levels were adjusted in order to study on three conditions for different thicknesses: rebounded-Impactor, maximum penetration and perforation; these amounts of energy were obtained using several tests.

The impact energy was calculated from impactor weight and drop height data. Visual inspection of the impacted specimens' damaged areas was facilitated by the semi-transparency of the composites. The damage topography was recorded with a digital camera.

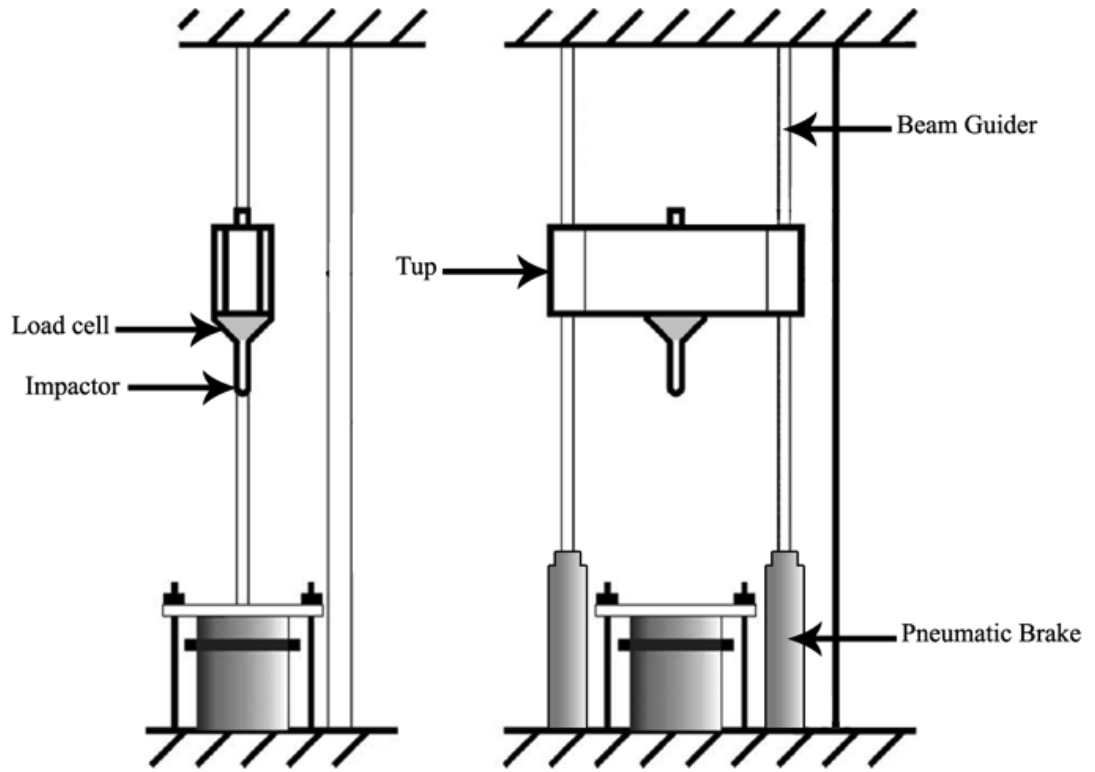


Figure 3.11. The schematic of the drop-weight machine.

3.2.3 Tensile Static test

The Monotonic mechanical properties of the specimens were determined using the tensile test. Speed of the test machine was adjusted on 5 mm/min. the elastic modulus of composite is slope of crossed line in the stress-strain curve in the strain range % 0.05 to % 0.025 according to ISO527 (Yuanjian et al., 2008). The samples fail when a transverse crack is observed. The maximum strength and the stress value at failure point are taken as brittle behavior of the laminates.

3.2.4 Fatigue loading

Fatigue testing was performed with a servo-hydraulic Instron 8502 model. The maximum fatigue loading capacity was 100KN and for static loading it was 250KN, while the maximum displacement was 150mm (± 75 mm). The specimens were placed between fixtures as shown in Figure 3.12.

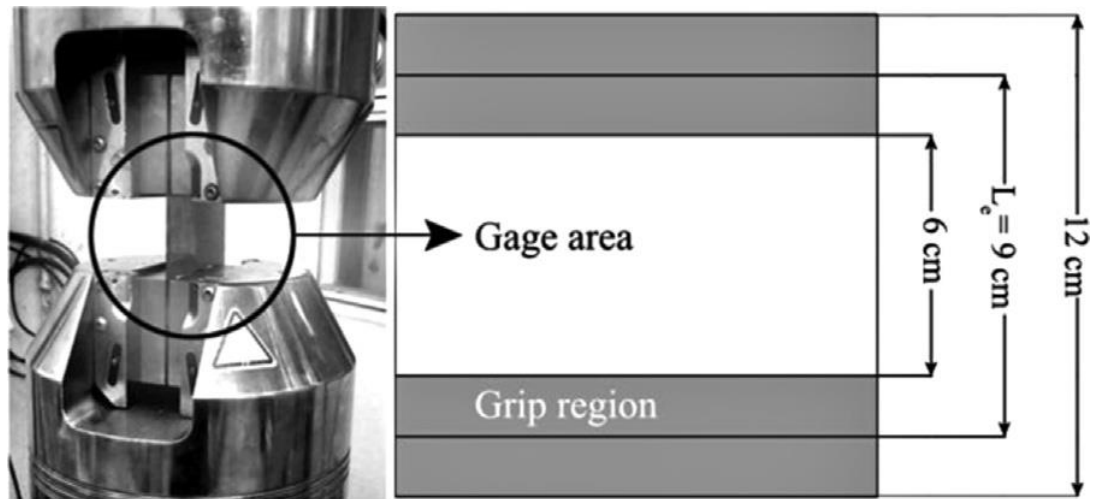


Figure 3.12. Composite plate location between the fixtures of the fatigue test machine.

Cyclic sinus loading was applied at a frequency of 3.5Hz. Joseph and colleagues (Joseph et al., 1994) studied the frequency effect on composites, and according to results for carbon/epoxy composites, a high frequency insignificantly affects fatigue life, but the effect is substantial for glass/epoxy. A 3.5Hz frequency was selected to decrease the influence of frequency and heat.

Fatigue strength was assessed in tensile mode and specimen life was recorded for undamaged and impacted laminates. The minimum force applied was zero, so R (minimum stress/maximum stress) stress ratio equaled zero and remained constant. The maximum stress value was assumed to be the fatigue strength. The loading amplitude was determined with the tensile strength of non-impacted samples and the amount of residual strength. The test continued until the laminates fractured completely.

3.3 Evaluation of mechanical properties for HA

Extensive analyses of indentation data obtained with a wedge-type indenter revealed that for incompressible materials, the overall relationship between the hardness and yield stress of an elastoplastic material can be expressed as (Briscoe et al., 1996):

$$R_y = \frac{H}{\sigma_y} = \frac{\xi}{\sqrt{3}} \left[1 + \ln \left(\frac{4\sigma_y}{3\pi E} \tan \alpha \right) \right] \quad \text{Eq. 3.1}$$

where E is Young's modulus of the material, ξ is a parameter which depends on the ratio of the yield stress and Young's modulus of the intended material, and α is the inclination of the face of the indenter. For hard metallic alloys and ceramics, ξ may be selected as $5\sqrt{2}/9$ and 1, respectively.

The Young's modulus was obtained directly from nanoindentation test machine. However In depth-sensing indentation techniques used in nanoindentation, the elastic modulus of the specimen can be determined from the slope of the unloading of the load-displacement response. The modulus measured in this way is formally called the indentation modulus of the specimen material. Ideally, the indentation modulus has precisely the same meaning as the term elastic modulus or "Young's modulus" but this is not the case for some materials. The value of indentation modulus may be affected greatly by material behavior (e.g. piling-up) that is not accounted for in the analysis of load-displacement data. For this reason, care has to be taken when comparing the modulus for materials generated by different testing techniques and on different types of specimens (Warren Carl Oliver et al., 1992b). The following equation shows that the indentation modulus as a function of dP/dh and the area of contact (Fischer-Cripps, 2011):

$$E = 0.5 \sqrt{\frac{\pi}{A}} \frac{dP}{dh} \quad \text{Eq. 3.2}$$

where E is Young's Modulus, P is indentation force and h is indentation depth.

Material hardness is defined as the ratio between the applied force and the projected contact area. The actual projected contact area A_m can be computed from the hardness value H and the maximum load of indentation P_m using Eq. 3.3.

$$H = P_{ave} = \frac{P_m}{A_m} \quad \text{Eq. 3.3}$$

Reduced elastic modulus \bar{E} can be obtained based on A_m and the slope of the unloading curve at maximum force and maximum depth $\left(S_m = \frac{dP}{dh}\bigg|_{h=h_m}\right)$ (Giannakopoulos et al., 1994):

$$\bar{E} = \frac{S_m}{c^* \sqrt{A_m}} \quad \text{Eq. 3.4}$$

where c^* is a computationally driven parameter that depends on the geometry of the indenter and its value for different indentation tests can be used to find the reduced elastic modulus for the indented material. For a Berkovich indenter, the c^* value is 1.2370.

For most materials, the curvature C may be expressed as a function of the characteristic stress $\sigma_{0.29}\bar{E}$ and σ_y (Bucaille et al., 2003; Dao et al., 2001; Larsson et al., 1996) as formulated in Eq. 3.5:

$$C = \frac{P}{h^2} = A\sigma_{0.29} \left\{1 + \frac{\sigma_y}{\sigma_{0.29}}\right\} \left\{B + \ln\left(\frac{\bar{E}}{\sigma_y}\right)\right\} \quad \text{Eq. 3.5}$$

where A and B are constant and depend on the indenter geometry. The values of A and B are 6.02 and -0.875 respectively for a Berkovich indenter. $\sigma_{0.29}$ is the stress which corresponds to the characteristic strain $\varepsilon_r = 0.29$ for the indented material under uniaxial compression. The characteristic strain is an important parameter in such analysis and should be carefully selected. Pervious FEM analyses for sharp indenters such as Berkovich and Vickers indenters suggests that $\varepsilon_r = 0.29$ (Bucaille et al., 2003).

Simply, yield strain is calculated from $\varepsilon_y = \sigma_y / E$; consequently, the work

hardening exponent can be computed from Eq. 3.6 using $\sigma_{0.29}$, σ_y and ε_y :

$$n = \frac{\ln(\sigma_{0.29}) - \ln(\sigma_y)}{\ln(\varepsilon_{0.29}) - \ln(\varepsilon_y)} \quad \text{Eq. 3.6}$$

The strength coefficient of the material is obtained using Eq. 3.7.

$$\sigma_y = K \varepsilon_y^n \quad \text{Eq. 3.7}$$

In chapter 7 the amount of hardening parameter will be summarized from the analytical method.

CHAPTER 4:FINITE ELEMENT SIMULATION AND MODELS FOR GFRP

4.1 FE simulation for low-velocity impact

This section provides details regarding the finite element simulation model used to analyze the impact phenomenon. The response of glass fiber epoxy composite laminates under low-velocity impact was modeled with MSC.MARC[®] MENTAT[®]. Three-dimensional solid elements with eight nodes were used for the discretization of the square specimen laminates. The nodes at the specimen's periphery were fixed in all directions. ORTHOTROPIC material was selected for modeling the material properties of composites.

The impactor of the hemispherical nose with 12.7 mm diameter is discretized with an 8-node solid element similar to that used for the composite laminate. The impactor is constrained to movement within 5 degrees of freedom (x and y translation and 3 rotation), and is allowed to move only in the z direction. The impactor is treated as a rigid elastic body with effective density of 7860 kg/m^3 , Young's modulus of 200 GPa and a 0.3 Poisson's ratio. An automatic contact condition is assigned between the composite target and impactor to accommodate impact initiation and progress. It starts with a point on the surface contact since the impactor touches the composite plate and progresses as a surface-to-surface contact. A contact criterion based on 0.01 mm of normal distance between the contact surfaces is adopted for the simulation.

The time step is one of the most crucial parameters, which normally causes divergence in non-linear finite element analysis. Choosing an adequate time step is another fundamental stage in the simulation process. Modal analysis indicates that $2 \times 10^{-8} \text{ s}$ is the minimum time required to prevent divergence of the solution process. The FE-model of the impactor and composite laminate is shown in Figure 4.1.

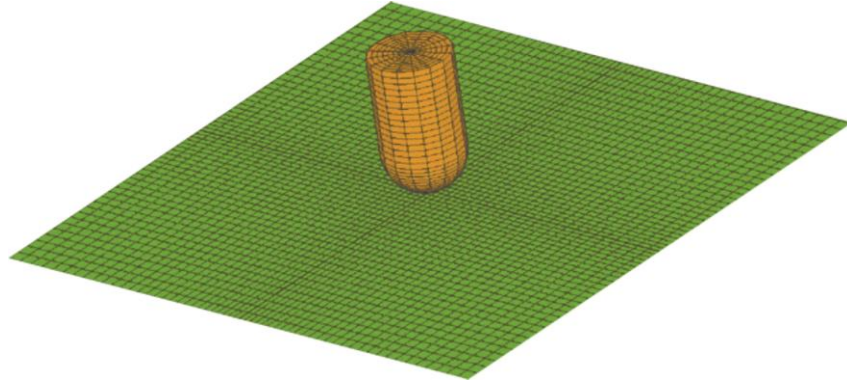


Figure 4.1. Finite element model with 12647 solid elements.

4.2 Calculating the energy absorbed or dissipated for impacted laminate

If an objective with mass m impacts a composite plate with a velocity v_0 , the impact energy of the impactor E_i can be expressed by (Baucom et al., 2005):

$$E_i = \frac{mv_0^2}{2} \quad \text{Eq. 4.1}$$

Besides, the kinematic energy $KE(t)$ transferred from object to the target (composite laminate plate) can be expressed by:

$$KE(t) = \frac{mv_0^2}{2} - \frac{m(v_i(t))^2}{2} \quad \text{Eq. 4.2}$$

where the velocity of the impactor $v_i(t)$ can be obtained by:

$$v_i(t) = v_0 - \frac{1}{m} \int_0^t F_{exp} dt \quad \text{Eq. 4.3}$$

The experimental impact force F_{exp} is measured during the impact event. Thus, it is possible to evaluate the impact energy, which reaches the composite plate, as well as the absorbed energy and the elastic energy (Figure 4.2).

The absorbed energy could be understood as *released energy*, because the failure mechanisms activated during the impact event release energy. However, the literature considers these release energies as a fraction of impact energy, which is absorbed by the structure and is not transformed on elastic vibrations (elastic energy).

Figure 4.2 shows that the absorbed energy from measurements can be calculated using

$$KE(t) = E_e + E_a \quad \text{Eq. 4.4}$$

where KE_i is the kinematic energy; E_e is the elastic energy and E_a is the absorbed energy.

In other words, the energy transfers from the object to the target (composite laminate plate) is absorbed by the failure mechanisms activated. Thus, each failure mechanism, i.e., intra ply failures and/or delamination absorb a fraction of impact energy. Therefore, the amount and the type of failure mechanisms activated will affect the absorbed energy values. However, the amount and the type of failure mechanisms activated depend on some factors:

- Mass and velocity of the impactor (impact energy level);
- Geometry of the impactor;
- Geometry of the structure;
- Type of fiber and/or matrix used for manufacturing of the composite structures;
- Stacking sequence of the plies.

For this work, the influence of the impact energy level and thickness of laminates was investigated.

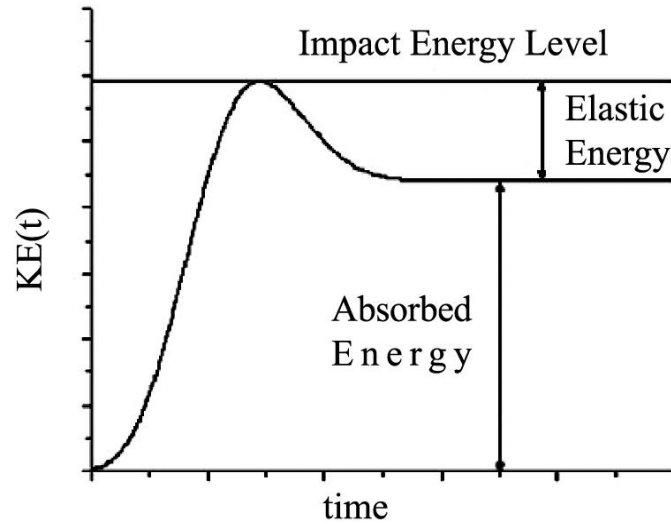


Figure 4.2. Estimating absorbed energy from a typical impact response of a composite laminate (David-West et al., 2008).

4.3 Fatigue failure model for composite materials

Composite materials subjected to fatigue loading accumulate damage that leads to fracture or functional failure of structures. For materials with homogeneous and isotropic properties, damage initially accumulates at a low growth rate and a single crack propagates in the direction perpendicular to the cyclic loading axis. On the other hand, in composite materials, especially structures with multiple plies and laminates, fracture behavior is characterized by multiple damage modes, such as matrix cracking, fiber fractures, ply cracking, delamination, void growth and multidirectional cracking. These modes appear rather early in the fatigue life of composites.

The mechanisms of crack initiation and growth in composite materials are fairly complex. Even for unidirectional, reinforced composites in simple loading cases such as tension along the direction of fibers, cracks may begin in various locations and directions. Not only can cracks start in the matrix, perpendicular to the direction of loading, but they can also initiate in the interface along the fibers' directions between the fibers and matrix due to debonding. Abundant experimental fatigue tests have been

carried out to examine crack growth in composites during the propagation of only one dominant crack in the same plane and direction as the initial crack. The Paris law helps describe this fatigue crack propagation behavior, but it is limited to unidirectional aligned fiber-reinforced composites. For more general laminates, a similar mode of crack propagation cannot be obtained even under simple loading. Thus, traditional fracture mechanics are ineffectual for the fatigue analysis of composite materials.

The concept of damage accumulation may serve as a more suitable approach to predicting the fatigue life of composite material structures. Nevertheless, it is not possible to measure fatigue damage directly. Therefore, the residual strength of composite materials is often employed to quantitatively evaluate fatigue damage due to cyclic loading.

4.3.1 The Broutman and Sahu Model

Broutman and Sahu (Broutman et al., 1972) proposed a simple, linear degradation model for residual strength, which is described by the following deterministic equation:

$$X_r = X - (X - \sigma_{max})\left(\frac{n}{N}\right) \quad \text{Eq. 4.5}$$

where X is the material's initial static strength, X_r is the residual strength after n loading cycles at maximum stress level σ_{max} , and N is the number of cycles to failure for this stress level, as derived from the S - N curve.

4.3.2 The Halverson Model

A linear damage summation model was first used to evaluate the fatigue behavior of composite materials by Nicholas and Russ (Chou et al., 1977). Halverson (Halverson et al., 1997) applied a power function in terms of cycle ratio to evaluate the remaining material strength and calculate the fatigue life.

$$F_r = 1 - (1 - F_a) \left(\frac{n}{N} \right)^j \quad \text{Eq. 4.6}$$

where F_r is the normalized remaining strength (normalized by the undamaged static strength), F_a is the normalized applied load (also normalized by the undamaged static strength), j is a material constant, n is the number of cycles of applied load, and N is the fatigue life of a constant load. According to the definition of damage in Eq. 4.6, the mathematical function for damage accumulation will also be a power function of cycle ratio. Therefore, the D damage parameter can be defined according to Eq. 4.7.

$$D = (1 - F_a) \left(\frac{n}{N} \right)^j \quad \text{Eq. 4.7}$$

In the current study, a fatigue failure model is modified using the two above mentioned models and a damage index is defined to describe the amount of damage to GFRP laminates.

CHAPTER 5:FINITE ELEMENT MODEL FOR HA

In this section, finite element methods will be elaborated for nanoindentation test on HA samples using the solid geometry and low-velocity impact on GFRP. The details for the porous geometry will be described in the next chapter.

5.1 Direct model for nanoindentation

The direct finite element model was made using MSC.Marc[®] software. Figure 5.1 illustrates the 2D and 3D mesh designs of the entire solid model with a magnified view of the mesh design under a Berkovich indenter. In the 3D simulation, the HA sample was modeled into a cylindrical shape rather than cubic in order to obtain proper mesh design in three radial directions. In the nanoindentation simulation, the indented surface is a free surface; the shape does not significantly affect stress distribution if the surface is considered large enough. The indenter and HA were considered rigid and elastoplastic materials, respectively. The mechanical properties of hydroxyapatite were calculated based on the analytical method and experimental data, which are presented in chapter 7. These HA properties were used in the simulation to obtain nearly the same force-penetration depth as the experimental nanoindentation test results.

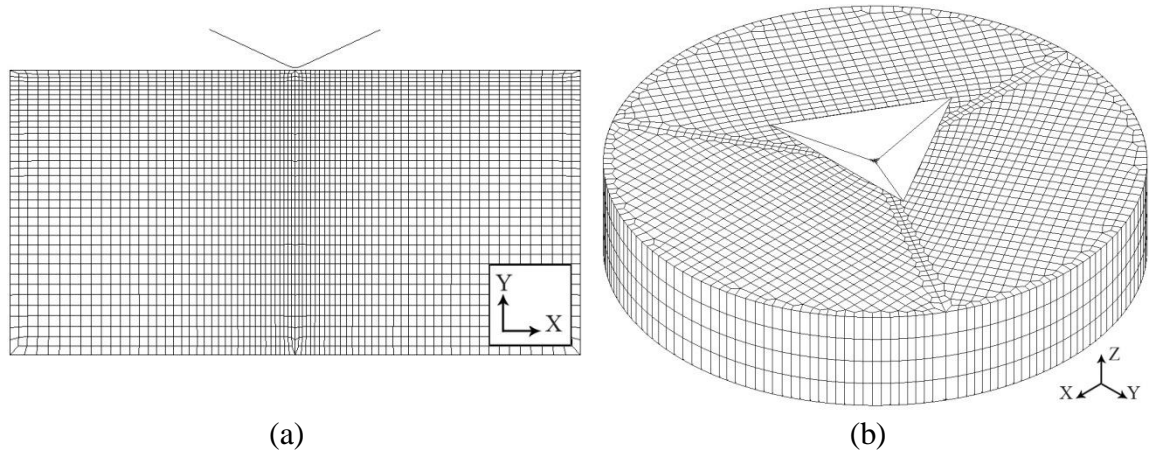


Figure 5.1. Finite element mesh for the Berkovich indentation test and solid structure: (a) 2D model, (b) 3D model.

In this study, the numerical analysis steps include only loading and unloading but not holding since the strain rate is not reflected in the material properties. Two methods were chosen to obtain a displacement-load curve from the FE model, which are force control and displacement control. Force control was adjusted according to the indentation force applied in the experiments; the maximum depth of indentation was implemented in the displacement control method. In the 3D model, only displacement control was used.

As the nanoindentation test was assumed to be quasi-static, the strain rate sensitivity was not considered. The adopted meshes are 4-node plain stress quads and 8-node 3D solid elements for 2D and 3D respectively. The contact between the indenter and the sample surface was modeled as rigid to deformable. Throughout the analysis, the nodes of the back face of the sample were constrained against displacement in the x- and y-directions for 2D and plus z-direction for 3D. The total deformation was calculated by the axial component of nodal displacement in the load direction for the node touching the indenter tip.

The output results of the finite element model are very sensitive to element size; therefore, it is necessary to check the effect of element size on result accuracy. Five different discretization models and non-uniform elements were used for the nanoindentation simulation of the displacement control models. The number of elements was increased by subdividing the elements into 2, 3, 4 and 5 divisions. The numbers of elements used were 2880 and 3840 for the 2D and 3D models respectively. Figure 5.2 shows a comparison between the obtained force-displacement curves for HA sintered at 1200°C. It is clear the four different discretization models are satisfactory and the accuracy cannot be improved beyond 5 times of subdivision. Therefore, the model with the lowest number of elements was adopted for the current investigation in order to reduce the number of calculations.

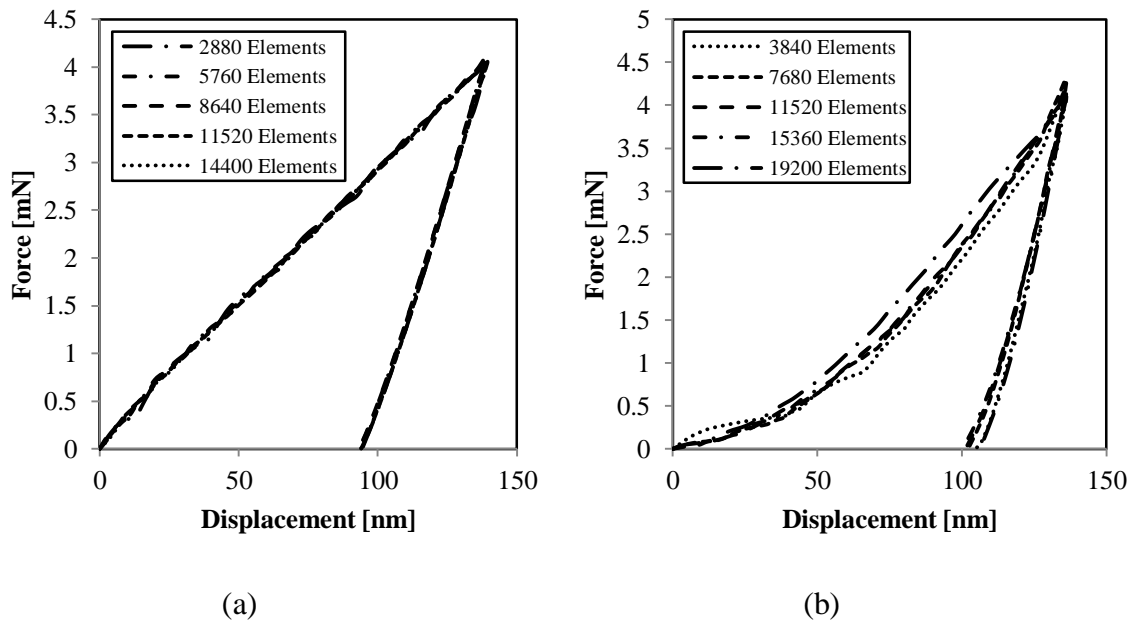


Figure 5.2. Effect of mesh size on the force-displacement curves obtained by incremental displacement solution method for: (a) 2D model, and (b) 3D model.

5.2 Inverse FE model for nanoindentation (for given material properties)

The main idea behind the present inverse FE model is to compare the force displacement data of the finite element simulation of the indentation test against the

experiment until a good match is achieved. The outlined procedure of the inverse technique for identifying the material parameters is represented graphically in Figure 5.3. The considered technique requires the experimental force displacement data from the nanoindentation experiment and elastic parameters of the HA specimen. For given material parameters n and k of the power hardening law, the model will predict the plastic modulus and force displacement curve. The predicted forces are compared with the experimental results until a good match is achieved. It is assumed the material is homogenous, isotropic and obeys the von Mises yield criterion.

Figure 5.4 explains the iterative procedure of the suggested inverse FE model for determining the hardening parameters (n and k) from experimental indentation data. The suggested inverse FE model is based on the displacement control technique. After each solution step, deviations of the predicted force displacement from the experiments are calculated. If the difference between the numerical and experimental loads at maximum load is less than or equal to 4% and the overall error is less than 10% then the material parameters are considered optimum. It is a noteworthy flow model represented by Eq. 3.7, and it was adopted through the finite element simulation. This procedure is followed for all test samples.

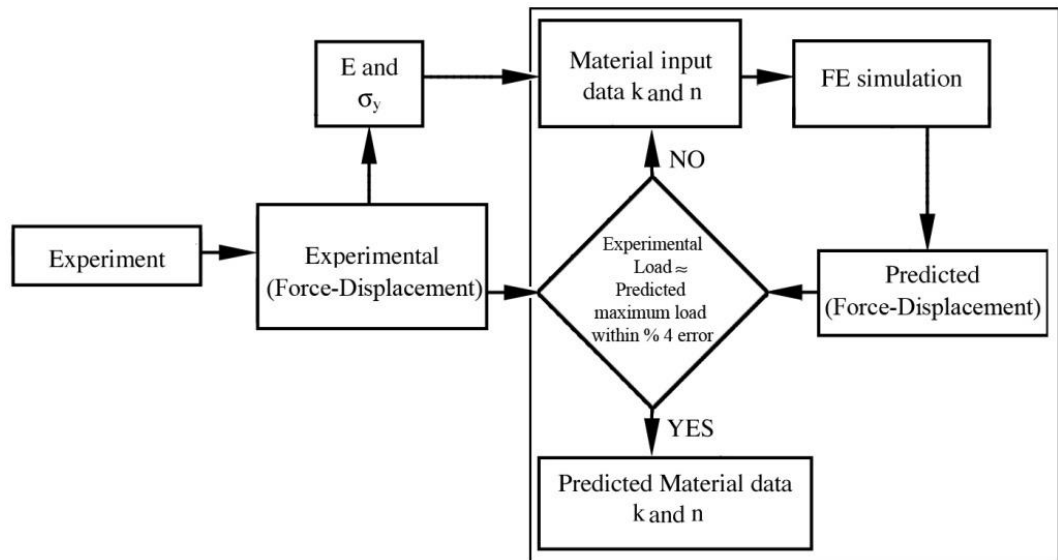


Figure 5.3. Outline of the inverse FE technique to determine the plastic properties of HA from nanoindentation experimental data.

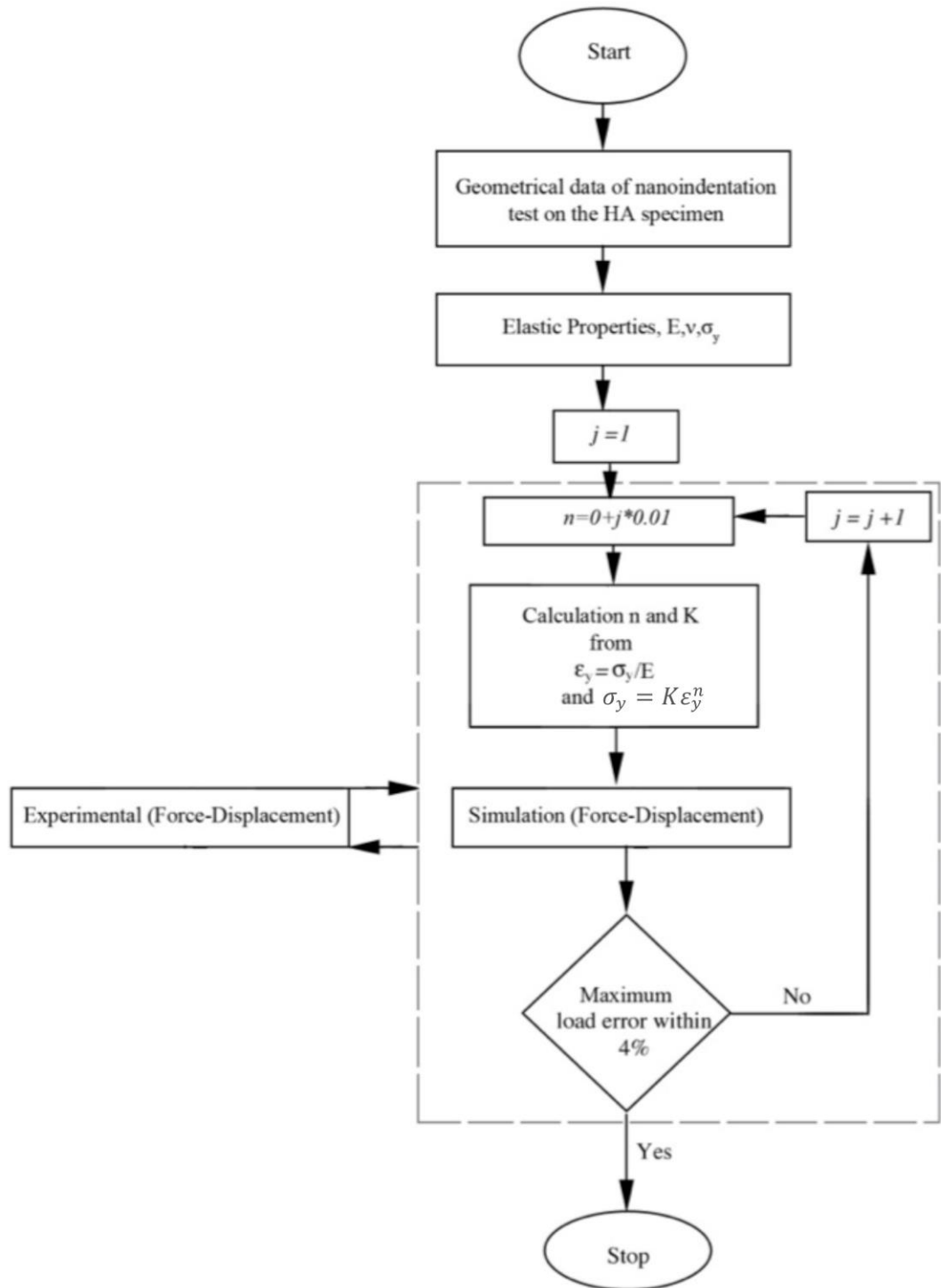


Figure 5.4. Procedure to determine the hardening parameters through a force displacement curve using nanoindentation data and inverse finite element technique.

CHAPTER 6:POROUS STRUCTURE MODELING BASED ON CENTROIDAL VORONOI TESSELATION

6.1 Introduction

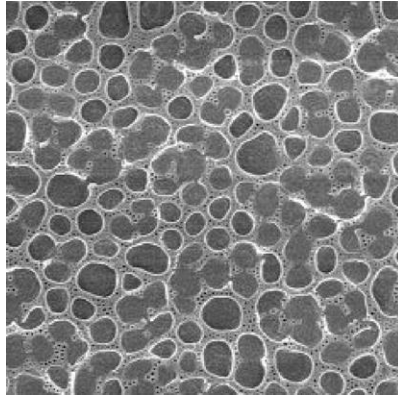
In good modeling of HA, the control ability of porosity and pore size is achieved. However there are limitations.

In 3D porous structure modeling, the accurate control of porosity is not easily achieved because of the numerous variables involved. Porous structure modeling method is short of analytical representation.

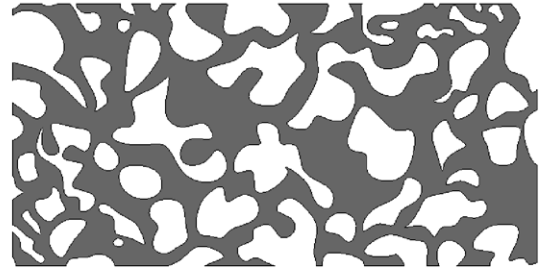
Adopting quadtree/octree enumeration to perform the modeling domain subdivision seems insufficient. These are questions that need to be addressed. Is this the best subdivision methodology to represent porous structures? Does the porous structure modeled with this approach match the model in nature?

6.2 A simple concept to generate irregular porous structure modeling

The objective of this chapter is to design irregular porous structures such as those shown in Figure 6.1 although it is straightforward to explicitly model the pore boundaries with B-Spline, however, manual designs of such cavities via direct specification of control polygons/polyhedrons are extremely tedious and unwieldy. Moreover, the modeled pore shapes and pore distributions would be highly dependent on or considerably constrained by designer's creativity and experience. In this work, we propose a nature-inspired representation, which imitates the formation process of a porous structure.



(a)



(b)

Figure 6.1. Examples of irregular porous structures. (a) and (b) are adapted from (Sirivithayapakorn et al., 2003; Wong et al., 2007) respectively.

6.3 Centroidal Voronoi tessellation

Nature creates structures based on the minimum energy principle, which means the formative processes in natural structures are characteristically governed by the least-energy responses. The structure that satisfies the minimum energy function is the most stable structure (Table 6.1).

Table 6.1. The characteristics and advantages of hexagons in porous structure design

Characteristics of hexagonal tessellation	Matched requirements
The least-energy internal arrangement	Provide high strength
The most economical method for partitioning a surface with maximum usable area	Provide highly porous structures with large surface areas
The ‘minimum-length’ connection of random points	Minimizes energy loss during transmission

According to the minimum energy principle, hexagonal geometry can be expected to provide high strength, highly porous structures with large surface areas and minimize energy loss during transmission (Pearce, 1990). Through observing objects in nature (structures or cells in plant, animal, viruses, metals and crystals), most of the structures exist in the form of hexagons. It has been proved that hexagonal tessellation is the most

economical method for partitioning a surface. Here the term ‘economical’ means hexagonal cells fulfill the minimum structure to maximum usable area criterion.

Hexagonal tessellation is also the ‘minimum-length’ connection of random points (Figure 6.2). Connecting an arbitrary number of random points in the plane in such a way to minimize the total distance between the points leads to a series of three line segments meeting at 120 degree angles (In geometry, a hexagon is a polygon with six edges and six vertices. The total of the internal angles of any hexagon is 720°).

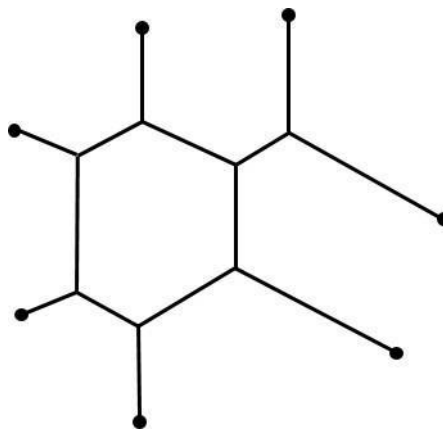


Figure 6.2. A ‘minimum-length’ connection of random points in a plan

6.3.1 Random aggregation model

In their seminal work, Schaefer and Keefer (Schaefer et al., 1986) for the first time, proposed a model that explained the formation mechanism of random porous materials. They contended that the porosity is due to random “jungle gym” or branched-polymer-like structures. From experimental data derived from small-angle X-ray scattering (SAXS), they proposed a random colloid-aggregation model, which states that during polymerization, “the silica particles first grow to a mean radius and then aggregate in a ramified manner and ultimately gel”.

Inspired by Schaefer and Keefer’s random colloid-aggregation model, in this thesis, we propose a geometric representation that follows the physical/chemical process of

polymerization. Voronoi tessellation is first generated to partition the space into a collection of compartments. Selective compartments are then merged together to imitate the random colloid aggregations. Through this Voronoi cell merging, irregular convex and concave polygons are obtained and the vertices of which are modeled as control points of closed B-Spline curves. The fitted B-Spline curves are then employed to represent the boundaries of the irregular- shaped pores.

The analogy between the terms/processes in Schaefer–Keefer model and the corresponding CAD counterparts are briefly listed in Table 6.2, and each mimetic modeling process is detailed in what follows.

Table 6.2. An analogy of physical/chemical polymerization and the nature inspired counter- part.

Physical/Chemical process	Nature inspired counterpart
Polymerization	Porous structure formation/modeling
Jungle gym	Voronoi tessellation
Ramifying process	Attribute based branching/classification
Colloid aggregation	Voronoi cell/polygon merging

6.3.2 A hybrid Voronoi tessellation and B-Spline based representation for pore shape and pore distribution modeling

To implement the “Jungle gym” structure, Voronoi tessellation is first generated to partition the space into a collection of compartments. For a point set $P = \{p_1, p_2, \dots, p_n\}, n \geq 2$ in the m-dimensional space R^m , the region $V(p_i)$ associated with a Voronoi generator point p_i which follows Eq. 6.1 is defined as the Voronoi cell of p_i (Okabe et al., 2009):

$$V(p_i) = \{x | \|x - p_i\| \leq \|x - p_j\|, \text{ for } i \in I_n, j \in I_n, j \neq i\} \quad \text{Eq. 6.1}$$

where $\|x_1 - x_2\|$ is the Euclidean-distance between point x_1 and x_2 , $I_n = \{1, 2, \dots, n\}$. Intuitively, the Voronoi cell or Voronoi region $V(p_i)$ consists of a point set, the elements of which are closer to p_i than any other points in P . The m -dimensional space R^m is partitioned into exactly n regions $v = \{V(p_1), V(p_2), \dots, V(p_n)\}$, as demonstrated in Figure 6.3(a), and this partition is called the Voronoi diagram of $P = \{p_1, p_2, \dots, p_n\}$ and P is called the generator points of this Voronoi diagram.

In R^2 the boundaries of Voronoi cells contain line segments, which are the perpendicular bisector of the line that joins two associated generator points. The boundary is called Voronoi edge, and all the Voronoi edges of the same Voronoi cell form a Voronoi Polygon. The point where three or more Voronoi edges meet is called Voronoi point or Voronoi Vertex.

Given a set of distinct points $P = \{p_1, p_2, \dots, p_n\}$, $n \geq 2$, the Voronoi diagrams can be constructed using Fortune's plane-sweep algorithm (Fortune, 1987). Let $V(p_i)$ be a Voronoi cell associated with the generator p_i and the vertices of the Voronoi polygon $V(p_i)$ be $\{v_0, v_1, \dots, v_m\}$, if we regard these Voronoi vertices as the control points of a closed B-Spline curve $C(u)$ of degree k , then

$$C(u) = \sum_{i=0}^m N_{i,k}(u) v_i \quad \text{Eq. 6.2}$$

where $N_{i,k}(u)$ is B-Spline basis function of degree k , which can be recursively defined by Eq. 6.3. To create a periodic B-Spline curve, the first and last k control points must be properly wrapped in the form such that $v_0 = v_{m-k+1}$, $v_1 = v_{m-k+2}, \dots, v_{k-2} = v_{m-1}$ and $v_{k-1} = v_m$.

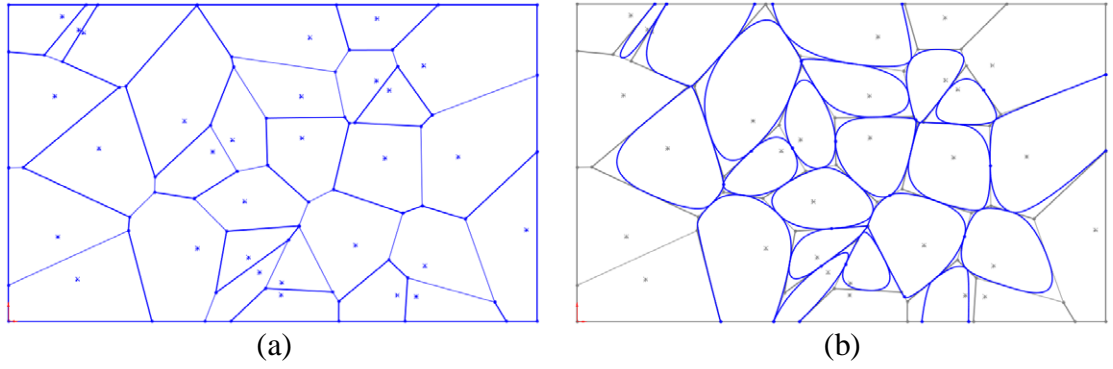


Figure 6.3. Voronoi diagram and B-Spline curves fitted from Voronoi polygon vertices.

$$N_{i,0}(u) = \begin{cases} 1 & (u_i \leq u \leq u_{i+1}) \\ 0 & (\text{otherwise}) \end{cases}$$

Eq. 6.3

$$N_{i,k}(u) = \frac{u - u_i}{u_{i+k} - u_i} N_{i,k-1}(u) + \frac{u_{i+k+1} - u}{u_{i+k+1} - u_{i+1}} N_{i+1,k-1}(u)$$

Figure 6.3(b) shows some cubic periodic B-Spline curves generated from the Voronoi cells shown in Figure 6.3(a). In this study, we propose to use such a closed B-Spline curve to represent the pore boundaries.

As can be seen from this figure, that hybrid Voronoi-B-Spline based representation is very suitable to represent irregular pore shapes. Since there are unlimited numbers of Voronoi tessellations for R^m and its subspaces, it is guaranteed that the shapes of the associated Voronoi polygons are not restricted to regular patterns. The use of periodic B-Spline curves to represent the pore boundaries can also effectively characterize the real world pore geometries which are seldom polygon or polyhedra-like, as those are shown in Figure 6.1.

This is a simple representation, however, also it has some limitations. For instance, the interstices between adjacent pores are too small and many pores nearly touch each other. Moreover, it is known that the Voronoi cells generated from distinct points are

always non-empty convex set (Okabe et al., 2009), therefore it is impossible to model such porous structures as shown in Figure 6.1(b), for which concave features such as crease edges or corners are commonplace.

To control the interstices in-between the modeled pores, a straightforward approach is to increase the order k of the B-Spline curves, since the higher the order k is, the farther the fitted curve deviates from the control polygon, as illustrated in Figure 6.4. Although a high order can be used in B-Spline curve fitting, however it is less practical to infinitely increase the order k .

6.4 Control of pore size

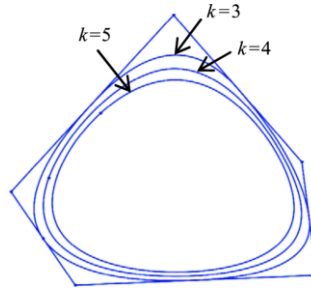


Figure 6.4. Different orders of B-Spline curves and the control polygon.

An alternative effective method is to scale the control polygon instead, and use the scaled polygon vertices to fit the B-Spline curves. In doing so, the centroid of the polygon is first computed from Eq. 6.4, which is used as the scaling center. The scaled polygon vertex can be then derived from Eq. 6.5:

$$x_c = \frac{1}{m} \sum_{i=1}^m x_i, \quad y_c = \frac{1}{m} \sum_{i=1}^m y_i \quad \text{Eq. 6.4}$$

$$\hat{x}_i = x_c + t(x_i - x_c), \quad \hat{y}_i = y_c + t(y_i - y_c) \quad \text{Eq. 6.5}$$

where (x_c, y_c) is the polygon centroid, (x_i, y_i) is the i -th control vertex of the polygon, (\hat{x}_i, \hat{y}_i) is the scaled control vertex, t is the scaling factor and m is the total number of vertices of the control polygon. Figure 6.5 shows the increments of pore interstices using scaled control polygons.

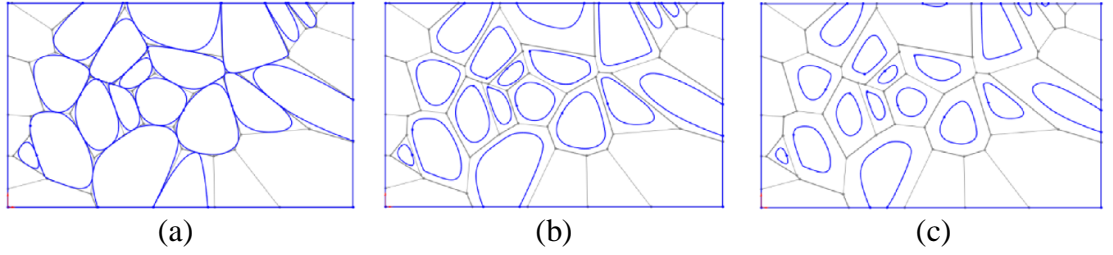


Figure 6.5. Modeling increased pore interstices using scaled control polygons. (a) Scale factor $t = 1.0$; (b) Scale factor $t = 0.8$; (c) Scale factor $t = 0.6$.

To enable modeling pores with concave shapes, the most straightforward way is to introduce concave polygons as the control points of B-Spline curves. Inspired by the random colloid-aggregation model discussed in previous section, we proposed to selectively merge some Voronoi polygons together so as to allow concave polygons to be modeled.

To accomplish this, an integer attribute λ is associated to each Voronoi polygon as shown in Figure 6.6(a) and (b), here different colors are used to represent the attributes associated with different Voronoi cells. The attribute λ is a random integer ranging from $[\lambda_{min}, \lambda_{max}]$ indicating the category it belongs to.

Two cells A and B are merged/aggregated together on the following conditions. (i) A and B belong to the same category, i.e. they have the same attribute value; and (ii) A and B are adjacent, i.e. they share some Voronoi edges in common.

Figure 6.6(b) highlights three Voronoi cells which satisfy these conditions (for brevity, we call them the child polygons of the merged polygon), and we will use the three cells inside the bounded circle.

Let the Voronoi vertices of the three Voronoi cells in Figure 6.6(c) be $\{a, b, c, d\}$, $\{b, c, e, f, g, h, i, j\}$ and $\{c, d, j, k, l\}$, and the Voronoi edges of these polygons are:

$$\begin{aligned} ve_1 &= \{a \leftrightarrow b, b \leftrightarrow c, c \leftrightarrow d, d \leftrightarrow a\} \\ ve_2 &= \{b \leftrightarrow e, e \leftrightarrow f, f \leftrightarrow g, g \leftrightarrow h, h \leftrightarrow i, i \leftrightarrow j, j \leftrightarrow c, c \leftrightarrow b\} \\ ve_3 &= \{c \leftrightarrow j, j \leftrightarrow k, k \leftrightarrow l, l \leftrightarrow d, d \leftrightarrow c\} \end{aligned} \quad \text{Eq. 6.6}$$

where the symbol $x \leftrightarrow y$ denotes vertex x is connected with vertex y , and x and y are the bounding vertices of an edge. To get the edges of the merged polygon, all the shared edges of the child polygons are excluded while the remainder non-shared ones, which constitute the edges of the merged polygon, are appended to the merged edge list.

By definition $x \leftrightarrow y$ is equivalent to $y \leftrightarrow x$, the edge pairs $(b \leftrightarrow c \in ve_1, c \leftrightarrow b \in ve_2)$, $(j \leftrightarrow c \in ve_2, c \leftrightarrow j \in ve_3)$ and $(c \leftrightarrow d \in ve_1, d \leftrightarrow c \in ve_3)$ in Eq. 6.6 are shared Voronoi edges and therefore excluded, and the edges of the merged polygon are therefore:

$$e = \{a \leftrightarrow b, d \leftrightarrow a, b \leftrightarrow e, e \leftrightarrow f, f \leftrightarrow g, g \leftrightarrow h, h \leftrightarrow i, i \leftrightarrow j, j \leftrightarrow k, k \leftrightarrow l, l \leftrightarrow d\}. \quad \text{Eq. 6.7}$$

Note that the edge of the merged polygon is generally stored in random orders in memory and there is no guarantee that the adjacent edges in the list are incident to each other.

6.5 Boundary and edge control algorithm

For visualization purposes, this does not matter; however to fit closed B-Spline curves, the sequence of the edge vertices does make a difference. To rearrange the edges

such that adjacent edges in the list are also geometrically consecutive, an ordered vertex list is created. All the vertices are then saved into the ordered list according to the edge connectivity relations.

The two vertices of the first edge, i.e. a and b are first appended in the ordered list, and the next edge, which is incident to the last vertex b , is then identified. In this example, the next edge is $b \leftrightarrow e$, so the vertex e is appended to the ordered list, and the edge $b \leftrightarrow e$ is excluded since both its bounding vertices are already included in the ordered vertex list. Such a process repeats until all the edges are interrogated, and the ordered vertex list now becomes $\{a, b, e, f, g, h, i, j, k, l, d, a\}$. As the first and the last vertex are the same, so the last one is removed, and the final control vertices of the B-Spline curve are $\{a, b, e, f, g, h, i, j, k, l, d\}$, as shown in Figure 6.6(d). Figure 6.6(e) shows the fitted B-Spline curves whose control points are generated from such ordered vertex list, and some concave shaped pores derived from the merged control polygons are clearly seen.

The pore interstices shown in Figure 6.6(e) are also very small. A simple approach to increase pore interstices is to apply the formulae of Eqs. (Eq. 6.4) and (Eq. 6.5). For concave polygons however, such a scaling operation is problematic and this can be clearly seen in Figure 6.7(a), where the scaled point set inside a concave polygon is no longer a subset of the original point set. Figure 6.7(c) shows a problematic case resulted from using the above simple approach. As highlighted in the circle-bounded region, the pores are no longer separated with small interstices, instead overlapped regions appear.

There are several approaches to solving this problem, for instance using the straight skeleton (Aichholzer et al., 1996). The straight skeleton is created by continuous shrinking of all edges of a polygon at a constant speed, and the skeleton is the set of traces of the moving vertices. The medial axis of a polygon is similar to the straight skeleton but the traces may include parabolic curves. Instead of scaling all the vertices

using the polygon centroid as the scaling center, the discussed problem can be resolved by moving the polygon vertices along the straight skeleton or the medial axis. However, both algorithms are relatively complex and the problem can be tackled with an alternative approach.

To accomplish this, we propose a relatively simpler and more straightforward method as compared with the straight skeleton or medial axis transform algorithms. The idea is very simple: for vertices which are not shared by adjacent Voronoi polygons, for instance $\{a, e, f, g, h, i, k, l\}$ in Figure 6.6(c), the scaled/shrunk vertices are calculated from Eqs. (Eq. 6.4) and (Eq. 6.5). As shown in Fig. 8(b), the shrunk vertices are now $\{a_1, e_1, f_1, g_1, h_1, i_1, k_1, l_1\}$. For vertices which are shared by two Voronoi polygons, for instance $\{b, d, j\}$ in Figure 6.6(c), the vertices are first separately scaled with respect to each child polygon's centroid using Eqs. (Eq. 6.4) and (Eq. 6.5), and the scaled vertices are now $\{b_1, d_1, j_1\}$ and $\{b_2, d_2, j_2\}$ in Figure 6.7(b). The coordinates of these scaled vertices $\{b_1, b_2\}$, $\{d_1, d_2\}$, $\{j_1, j_2\}$ are then averaged and output as the new coordinates of the shrunk vertices, i.e. $\{b_{12}, d_{12}, j_{12}\}$ as shown in Figure 6.7(b). The final vertices of the shrunk polygon are therefore $\{a_1, b_{12}, e_1, f_1, g_1, h_1, i_1, j_{12}, k_1, l_1, d_{12}\}$.

Without loss of generality, all the vertices of the shrunk polygon whose vertices are $\{v'_0, v'_1, \dots, v'_m\}$ can be formulated as:

$$\hat{v}_i(t) = \sum_{i=0}^m w_i v_i \quad \text{Eq. 6.8}$$

where $\{v_0, v_1, \dots, v_m\}$ is the vertices of the original polygon, w_i is a weight related to the shrinking or scaling factor t . A rigorous proof that the shrunk control polygon will always be contained in the original polygon is straightforward. Figure 6.7(d)

demonstrated the result of using the proposed approach to increase the pore interstices, and the effectiveness is clearly shown in contrast with the result shown in Figure 6.7(c).

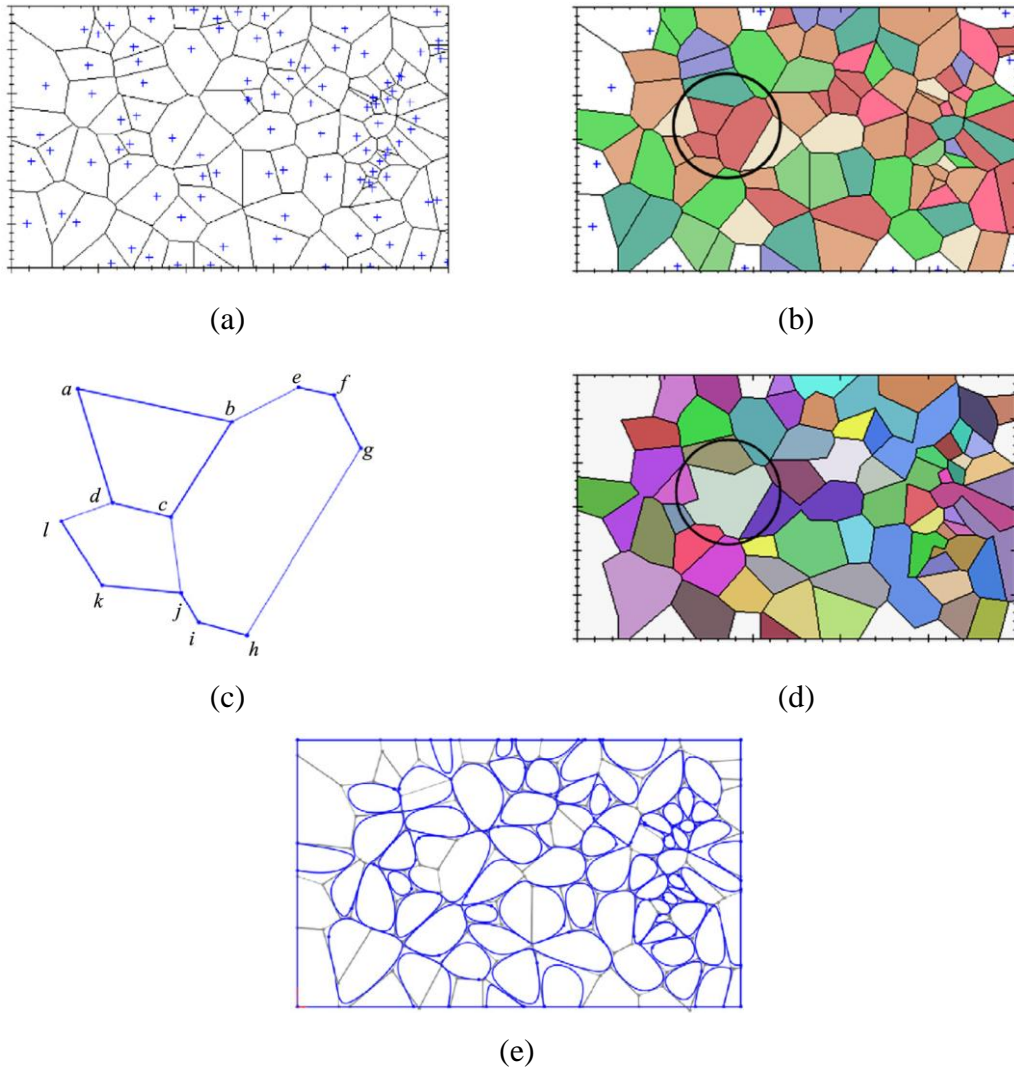
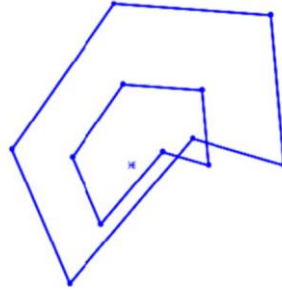
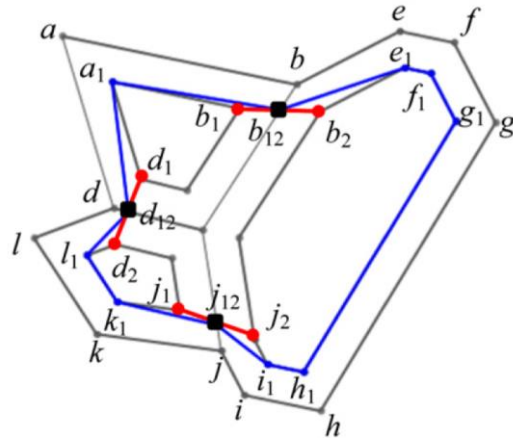


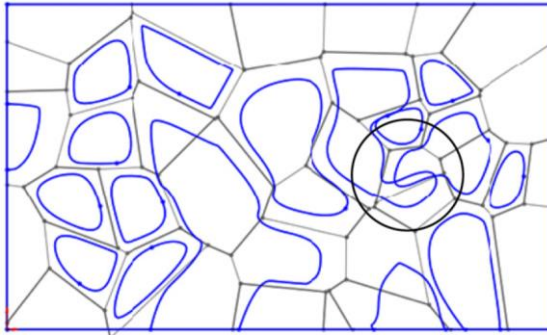
Figure 6.6. Cell attributes association and concave pore modeling. (a) A Voronoi diagram with no attributes associated. (b) Each cell is randomly associated with an integer attribute, represented with a fill color. (c) A zoomed view of three Voronoi polygons to be merged. (d) Adjacent same-attributed Voronoi polygons are merged to form a bigger polygon. (e) The fitted B-Spline curves and their control polygons. Note that the cell attribute of the merged cell shown in (d) may not be exactly the same as the attributes of the child cells in (b), and attributes are used only for classification purposes.



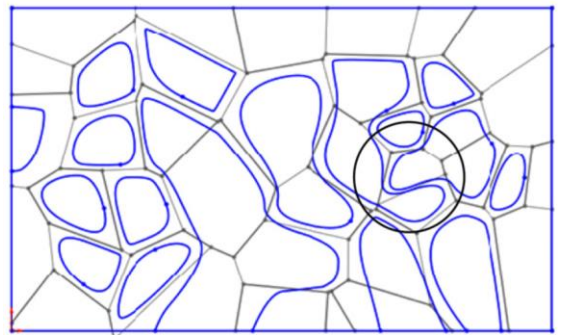
(a)



(b)



(c)



(d)

Figure 6.7. Scaling of convex polygons and closed B-Spline fitting. (a) The down-scaled point set is not a subset of the original point set. (b) The proposed polygon shrinking scheme. (c) A problematic case of using naive scaling operation. (d) The desired increment of pore interstices.

6.5.1 Geometric model of 2D irregular porous structures

In the previous sections, a hybrid Voronoi tessellation and B-Spline based representation is proposed to model irregular-shaped pores. Based on this representation, an irregular porous structure can be defined as follows.

Denote G_{ext} as the external geometry of an object, and a discrete point set $P = \{p_1, p_2, \dots, p_n\}$, $p_i \in G_{ext}$ includes n points which are inside G_{ext} . Let the Voronoi tessellation of P be $v(P) = \{V(p_1), V(p_2), \dots, V(p_n)\}$. For each Voronoi polygon $\delta V(p_i)$ represented by a list of vertices $\{v_0, v_1, \dots, v_m\}$, the shrunk polygon whose vertices are calculated by Eq. 6.8 is denoted as $\delta V(p_i, t)$, where $0 < t \leq 1$ is the shrinking or scaling factor. The closed B-Spline curve fitted from $\delta V(p_i)$ can be obtained from Eq. 6.2 and denoted as $C(p_i, t)$. We define the point set S_i bounded by $C(p_i, t)$ as a pore, and the Boolean union of S_i is then modeled as the pore space S . A porous structure Ω is then constructed with the Boolean subtraction of S from G_{ext} :

$$S = \bigcup_i S_i \quad \text{Eq. 6.9}$$

$$\Omega = G_{ext} \setminus S \quad \text{Eq. 6.10}$$

where the \bigcup and \setminus refer to the Boolean set union and subtraction operators.

Figure 6.8 illustrates an irregular porous object modeled with the proposed representation. The external geometry G_{ext} of the porous object is a 2D rectangle with 0.5 mm in length and 0.3 mm in width. One hundred points are randomly generated inside G_{ext} , and ten attributes $\lambda = 1, 2, \dots, 10$ are randomly associated to the one hundred Voronoi cells.

The aggregated polygons are shown in Figure 6.8(a), and all the polygons are then shrunk with a factor of $t = 0.75$ to guarantee sufficient pore interstices. Closed B-Spline curves with order $k = 5$ are fitted from the shrunk polygons. The shape and distribution of the pore are depicted in Figure 6.8(b). The results of applying a Boolean subtraction of the pores from the external geometry are shown in Figure 6.8(c), rendered in filled color.

Comparing the irregular porous models shown in Figure 6.1(b) and Figure 6.8(d), it can be clearly seen that they are generically similar in both pore shape and distributions. The difference is that the model in Figure 6.1(b) is reconstructed from SEM images (Sirivithayapakorn et al., 2003), whereas the one shown in Figure 6.8 is modeled from a constructive approach using CAD tools.

The benefit of this constructive design is obvious. Such models are constructed based on stochastic geometry and theoretically there are numerous different configurations in terms of the pore shapes and distributions. Among these infinite choices/configurations, although it is possible to manually design one of them using conventional CAD modeling approaches, however the workload required is hardly comparable with the proposed approach. The manual approach is not only labor-intensive, but also tedious and unwieldy; and moreover the versatility and quality of the design are also closely constrained by the designer's creativity and experience.

The modeling efficiency of the proposed approach is also an important advantage. If the irregular porous structures are to be designed via optimization methods, for instance, the sensitivity based iterative approaches or population based approaches (e.g. Genetic algorithm), variant geometric models must be efficiently constructed in accordance with parameter updates, otherwise the overall throughputs and productivity of the optimization will be severely undermined.

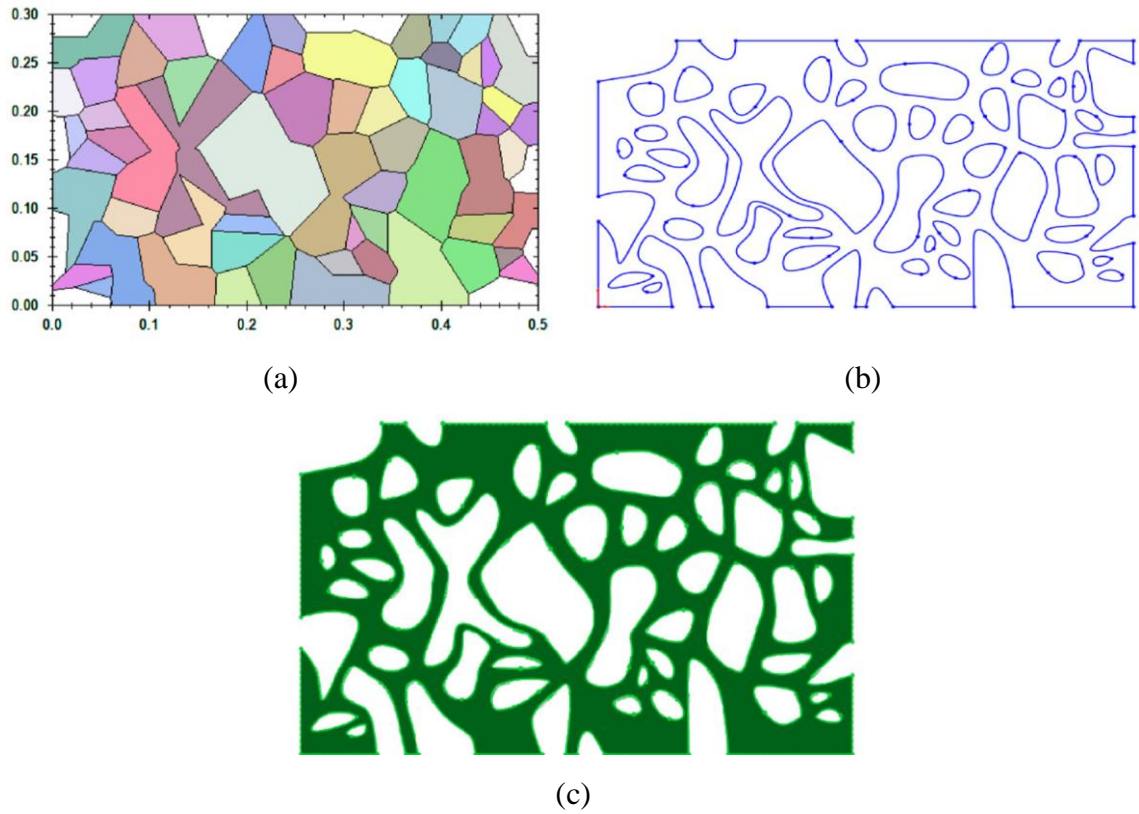


Figure 6.8. An irregular porous structure model. (a) The control polygons used for B-Spline curve fitting. (b) The pore geometries represented by B-Spline curves. (c) Boolean subtraction of the pores from the external geometry and the resultant 2D representation of the irregular porous structure.

6.6 3D geometrical model for irregular porous structures

A 3D solid structure is considered as a layered material, which in each layer includes some pores. This concept is similar to Magnetic resonance imaging (MRI) processes as media is captured in several layers. The sole difference is that the layers are generated by computer.

Using the proposed representation and design method, it was further modeled a simple 3D porous structure as shown in Figure 6.9. As shown in Figure 6.9(a) to (d) there is a 3D feature extruded from a 2D porous structure, and the detailed modeling scheme can be found in previous sections. Each of the models was assumed as a layer

that they were merged in Figure 6.9(e). This technique provides a 3D structure which is close to reality besides the geometry can be meshed easier than the others with complex geometry.

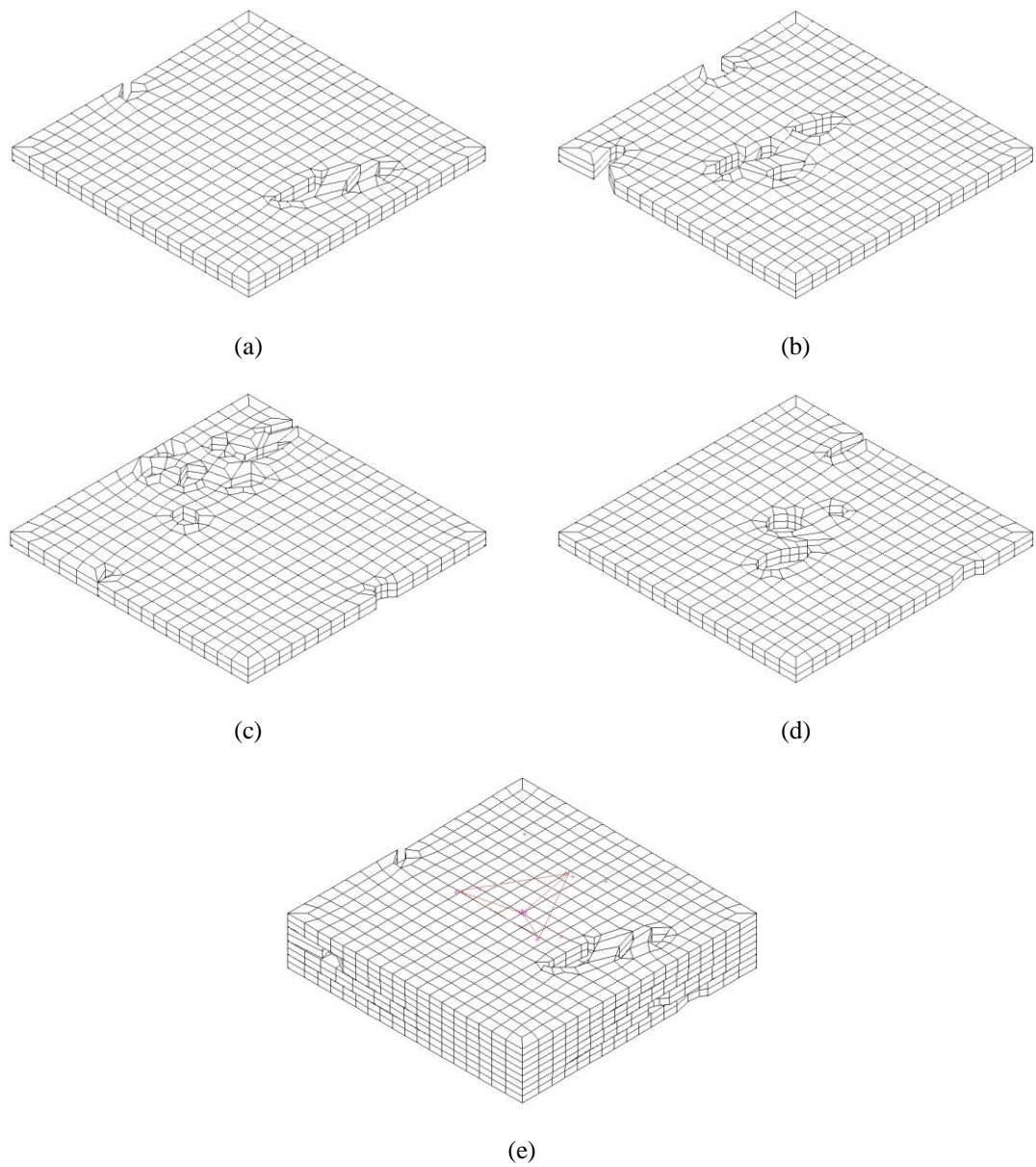


Figure 6.9. Different extruded 2D porous layers (a, b, c and d) and merging layers (e) to generate 3D structure implemented to finite element analysis for Berkovich nanoindentation problem on HA model.

CHAPTER 7: RESULTS AND DISCUSSION

7.1 Introduction

The present chapter contains analysis and discussion on the conducted experiments besides of numerical and analytical results. Ten experiments and specimens are investigated using available characterization and analysis techniques.

7.2 Hardening parameters for HA

In order to validate the suggested analytical method for direct and inverse FE models, comparisons between measured and predicted load displacement curves for nanoindentation testing have been done at different n and K values. Table 7.1 summarizes the work hardening parameters at different sintering temperatures of hydroxyapatite as obtained from the analytical method, whereas those predicted by the inverse technique for 2D and 3D models are given in Table 7.2.

Table 7.1 and Table 7.2 indicate that the hardening parameters estimated by the inverse technique for 2D and 3D models agree well with those calculated with the analytical method. The effects of sintering temperature on force displacement curve mesh deformation, stress strain curves and hardening parameters were investigated. A deduction in hardness is due to both the presence of secondary phases and larger grain sizes are detrimental hardness of HA (De Groot, 1980; P.E. Wang et al., 1993).

Table 7.1. Work hardening parameters of hydroxyapatite at different sintering temperatures as calculated from the semi-empirical model.

No.	Sintering temperature (°C)	E (GPa)	H (GPa)	σ_y (GPa)	A_m (nm ²)	S_m (μN)	\bar{E} (GPa)	C (nm)	$\sigma_{0.29}$ (GPa)	ε_y	n	K (GPa)
1	HA-1000	47.4	1.51	0.69	1.21E ₆	64.353	47.3	0.0026	19.296	0.014	0.46	4.92
2	HA-1100	77.6	2.97	1.46	1.97E ₆	100.59	57.9	0.0651	23.726	0.018	0.39	6.99
3	HA-1200	150.3	6.46	3.35	6.32E ₅	119.16	38.3	0.0897	15.606	0.022	0.21	7.80
4	HA-1300	131.4	6.61	3.68	6.08E ₅	104.01	34.1	0.1327	13.870	0.028	0.23	8.37
5	HA-1400	87.2	4.29	2.36	9.23E ₅	85.79	22.8	0.0936	9.154	0.027	0.30	6.97

Table 7.2: Hardening parameters determined by the inverse technique for 2D and 3D models

Sintering temperature (°C)		1000	1100	1200	1300	1400
n	2D-model	0.43	0.39	0.23	0.19	0.31
	3D-model	0.40	0.35	0.23	0.19	0.31
K (GPa)	2D-model	4.32	6.99	8.06	7.26	7.23
	3D-model	3.80	5.96	8.06	7.26	7.23

7.2.1 Force displacement curves

Force displacement curves are depicted in Figure 7.1a-d as obtained from experimental data and finite element analysis. These curves were calculated with the analytical method for the indentation tests and FE results at different sintering temperatures. The force displacement curves can be divided into loading, holding and unloading. The holding part is observed at maximum force according to experimental results (Figure 7.1a), whereas it was not modeled in the finite element simulations. In the experiments, due to the pores in the under layers, the steps can be seen in the force displacement curves through the loading part.

Maximum force, maximum depth and residual plastic deformation are the three main parameters that characterize the force displacement curves. In the finite element model maximum force and depth were applied to the indenter for force control and

displacement control respectively. As seen in Figure 7.1, for different sintering temperatures the predicted values of these three parameters are in good agreement with the experimental results with maximum error 4%.

Generally, for the harder samples, the FE analysis and experimental curves show a more similar trend. The sintered HA-1200°C sample has the highest elastic modulus of 150.3 GPa and hardness of 6.46 GPa. The HA samples was studied as a bulk material however crystalline HA has higher elastic modulus because basically HA is anisotropic materials which shows different mechanical properties in different directions (Ching et al., 2009). Figure 7.1 indicates adequate estimation of elastoplastic properties and consequently, an accurate FE model. However, the estimated force displacement curve for the HA-1000°C sample does not match well with the experimental data; as in the current simulation, the strain rate parameter was not considered but the effect of this factor in harder (brittle) materials can be neglected. In this study the elastic limit is based on off-set method which is the horizontal distance between the modulus line and any line running parallel to it and the amount is 0.2%.

Table 7.1, Table 7.2 and Figure 7.1 indicate when the work hardening exponent n increases and work hardening rate parameter K decreases, the material exhibits more plastic behavior. The HA-1000°C sample has the lowest hardness value of 1.51 GPa, while if the temperature increases to 1200°C, the hardness value is at a maximum. By raising the sintering temperature the HA sample displays a more inelastic trend and the hardness value reaches 4.29 GPa at 1400°C sintering temperature. In comparing the 2D and 3D models, the trends of the 3D force displacement curves are in better agreement with the experimental results. It is preferable, however, for the 2D simulation to be used rather than the 3D method since the 2D models save time for solving the problem.

The displacement and force control methods overestimate the load and displacement values in comparison with the experimental results. Since during the indentation is

the piling-up or sinking-in of the surrounding material. If the metal is work hardened it has a tendency to pile up and form a "crater". If the metal is annealed it will sink in around the indentation. Both of these effects add to the error of the hardness measurement. The divergence between the anticipated and experimental results could be due to the pile-up phenomenon. Oliver and Pharr's proposed method is best applied when no pile-up occurs but some sink-in takes place when the sample is indented. In the case of pile-up, contact depth is always greater than the total depth of indentation, thus the projected area is always underestimated (Warren Carl Oliver et al., 1992a). This underestimated area may lead to overestimating both hardness and reduced elastic modulus values; however it has significant effects on hardness value.

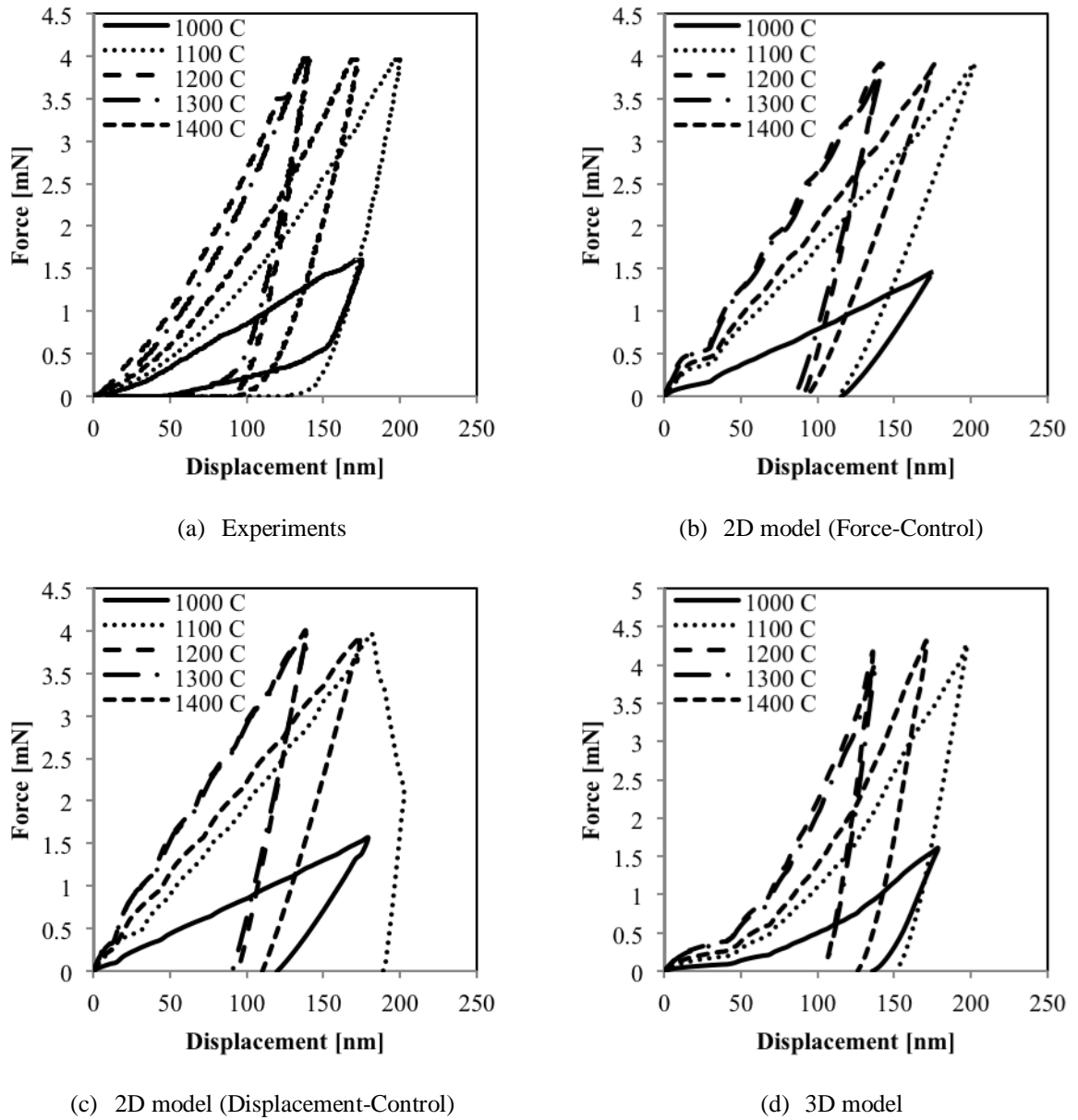


Figure 7.1. Force displacement curves obtained from the nanoindentation test of HA and finite element analysis; material parameters are based on Table 7.2 for different sintering temperatures, 1000, 1100, 1200, 1300 and 1400°C in 2D and 3D.

7.2.2 Mesh deformation

Figure 7.2 shows the AFM 3D image and FE deformed mesh of the 3D nanoindentation test. The indented surfaces are almost the same for both AFM and simulation results. This ensures the quality of the FE model and response of the material model used in the simulation. It is worth noting that the porosity of HA is not considered in the analysis and inverse FE model with solidarity assumption was used to

calculate elastic-plastic properties of HA. However, the indented surface is nearly the same for both numerical and experimental images. The solidarity assumption is approximately valid since the inverse FE model is based on matching the experimental and numerical force displacement curves. This means the effect of prosperity is inherently included in the analysis.

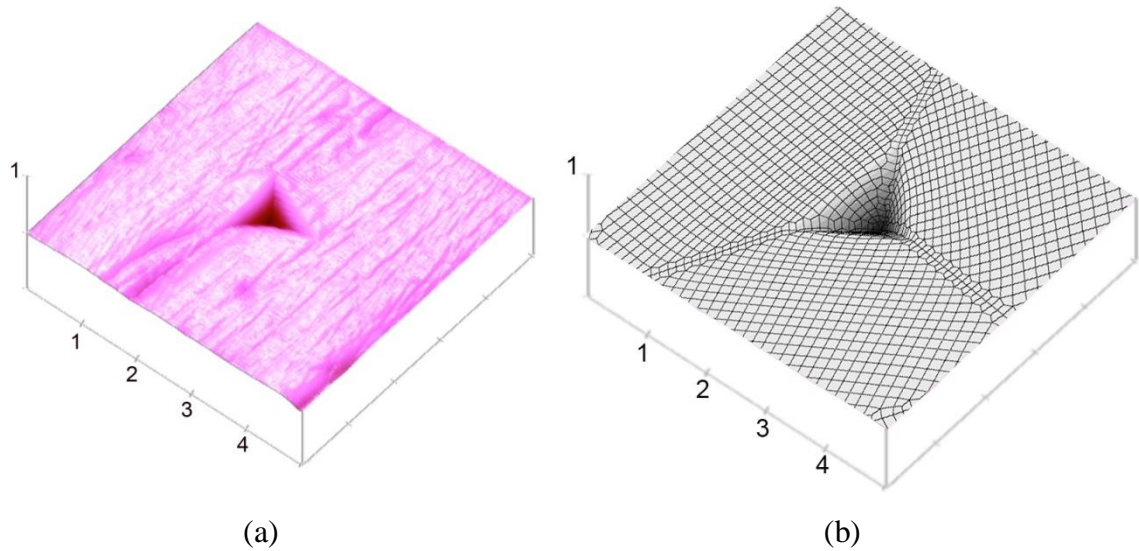


Figure 7.2. (a) AFM image of indented sample, (b) FE deformed mesh for 3D model.

7.2.3 Effect of sintering temperature on $\sigma - \epsilon$ curves

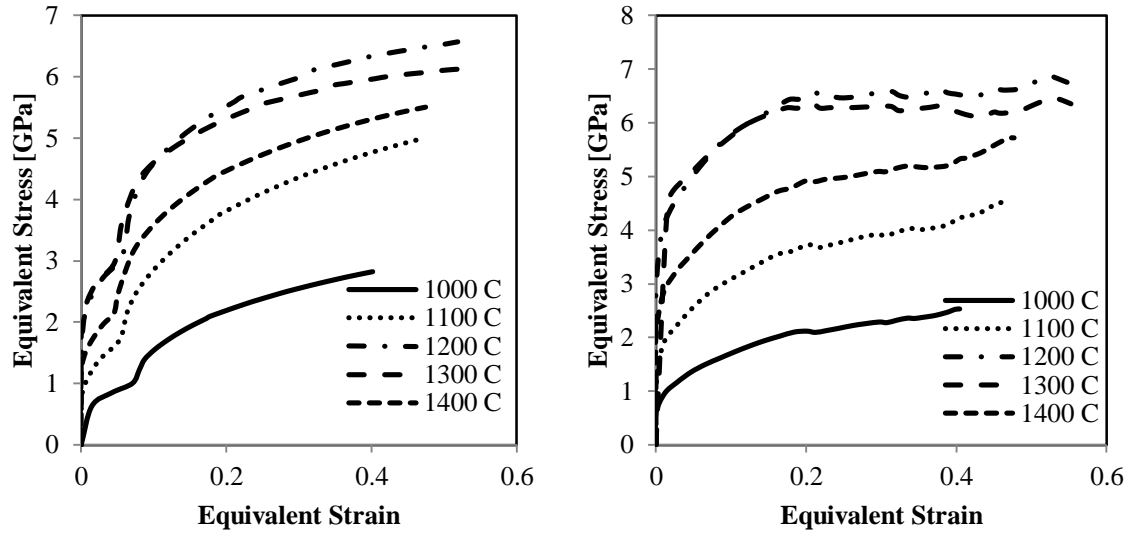
The equivalent stress and strain curves obtained from the numerical analysis for the 2D and 3D models are plotted in Figure 7.3. The power law ($\sigma = K\epsilon^n$) is used to fit the experimental data and validate to what extent the models' mechanical behavior follows that material's model. In the FE simulations, the material models were assumed isotropic; consequently, the anisotropy properties could not influence the stress-strain curves. The stress and strain distributions in all directions were expressed in terms of the equivalent value. Figure 7.3 shows the differences between the stress-strain curves for 2D and 3D and the predicted power law. The differences are significant for harder HA-1200 and 1300°C samples, especially when using the 3D model. It is worth mentioning that an increasing sintering temperature curve enlarges stress-strain. This

maybe attributed to the large grain size of HA samples sintered at highest and lowest temperature. Grain size can be obtained from Petch hall equation as a stress function:

$$\sigma_y = \sigma_0 + K/\sqrt{d} \quad \text{Eq. 7.1}$$

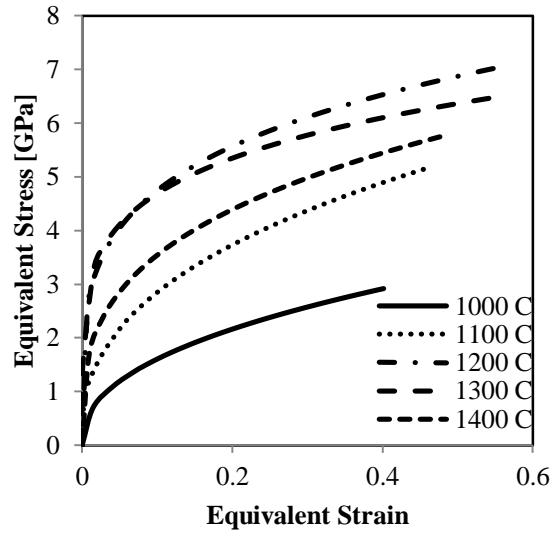
where d is the average grain diameter σ_y is yield stress, K is empirical constant.

The increase of hardness and with decreasing grain size has been observed in many oxide and nonoxide ceramics. In particular, this phenomenon is observed when grain sizes are in the range of 1–50 μm (J. Wang et al., 2010).



(a) 2D model

(b) 3D model



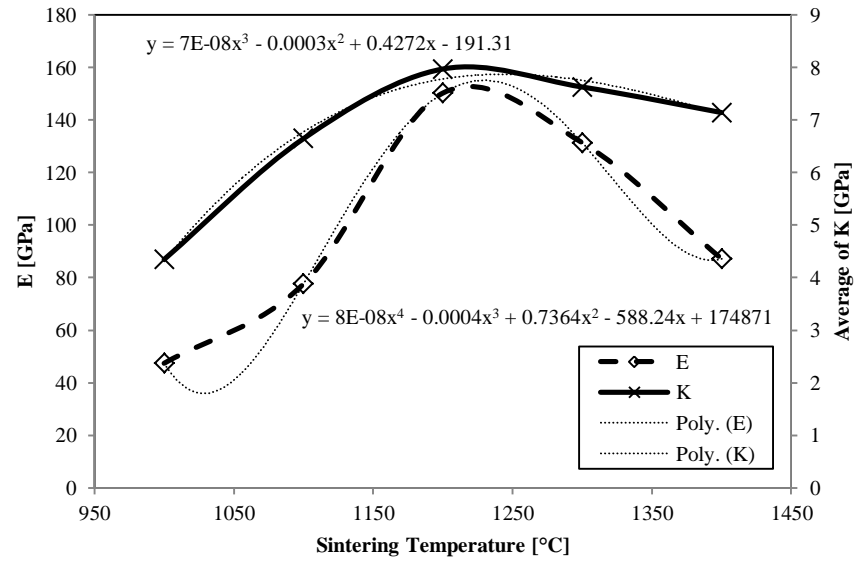
(c) Formula

Figure 7.3. Equivalent stress-strain responses of the different sintered hydroxyapatite extracted from 2D and 3D numerical analyses in comparison with the formula ($\sigma = K\varepsilon^n$).

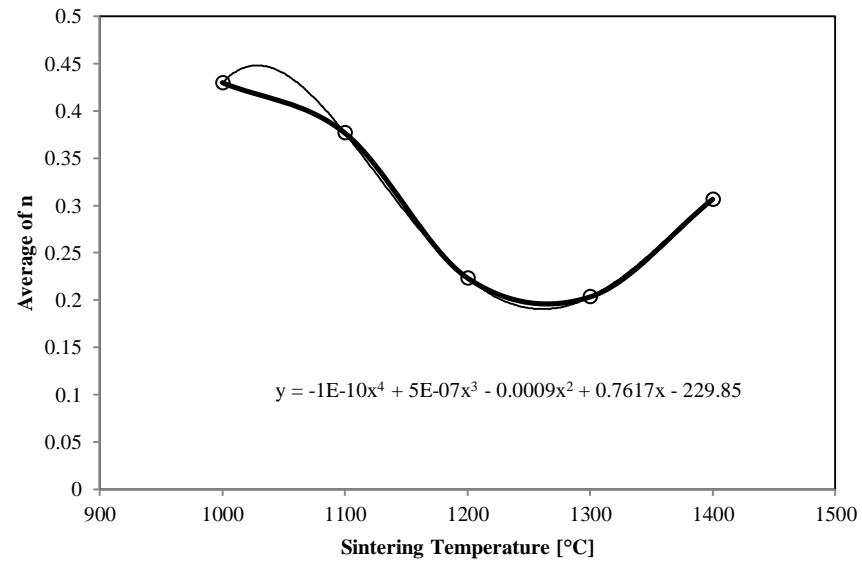
7.2.4 Effect of sintering temperature on hardening parameters

The influence of sintering temperature on the hardening parameters n and K as well as elastic modulus E , is shown in Figure 7.4. The n and K values are average values obtained from the inverse technique and analytical method (Table 7.1 and Table 7.2) whereas the elastic modulus E is obtained directly from the nanoindentation tests. In

order to predict the behavior of mechanical properties with sintering temperature, the trend of elastoplastic parameters was fitted and the related equations are given in Figure 7.4. It is observed that there is a critical sintering temperature range between 1200 and 1300°C, in which the E and K values are maximum and the n value is minimum. This explains why the HA-1200 and 1300°C samples are harder, and show more brittle behavior and less plastic deformation.



(a)



(b)

Figure 7.4. (a) Elastic modulus E and average values of K , (b) average n value versus sintering temperature for the hydroxyapatite samples.

7.3 Effect of porous geometry on indentation of HA

Following chapter 5, the technique is applied to create 2D and 3D porous media in order to use the geometry in FE simulation. In this section the effect of porosity will be analyzed under indentation loading and will be compared to solid (non-porous) structures.

7.3.1 Topologies and porosities for 2D

As demonstrated in chapter 5, the proposed geometric representation has a flexible degree of control on the pore shapes and distributions. Among others, users can accomplish this by (1) Adjusting the count and spatial distribution of generator points; (2) Adjusting the count and value distribution of random attributes associated with Voronoi cells; (3) Tailoring the orders of the B-Spline curve and (4) Tailoring the scaling factors.

Figure 7.5 shows two porous structures with different topologies, which are generated with the same set of generator points, but with different attributes associated. In Figure 7.5(a) 150 Voronoi cells, and the probability that adjacent cells have the same attribute value will be much higher than the case where is shown in Figure 7.5(b). Therefore after polygon merging, many concave-shaped pores appeared in the porous structure shown in Figure 7.5(a), while most of the pores in Figure 7.5(b) are convex shaped.

Figure 7.6 illustrates two examples with similar shapes but different porosities. Both porous structures are generated using 50 generator points, but different scaling factors are used. The porosities of the structures shown in (a) and (b) are with 40% and 90% scaling factors respectively.

As an evidence for porosity of HA, Figure 7.7 illustrates some microstructure of porous HA samples sintered between 1000, 1100, 1200 and 1300 °C. Interconnected grains of $\sim 1\ \mu\text{m}$ in size and a significant amount of fine porosity can be clearly observed at 1000 °C.

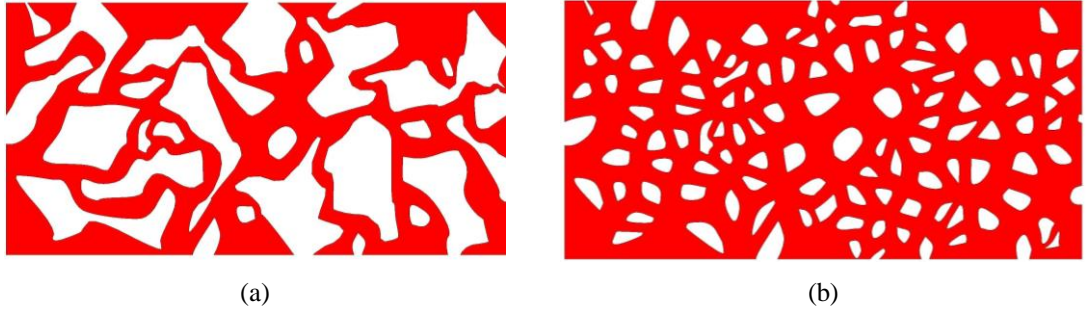


Figure 7.5. Porous structures with different topologies. (a) An irregular porous structure with many concave-shaped pores, the model is constructed with 150 generator points are randomly associated with the Voronoi cells. (b) An irregular porous structure with many convex shaped pores, the model is constructed with same 150 generator points are randomly associated with the Voronoi cells.

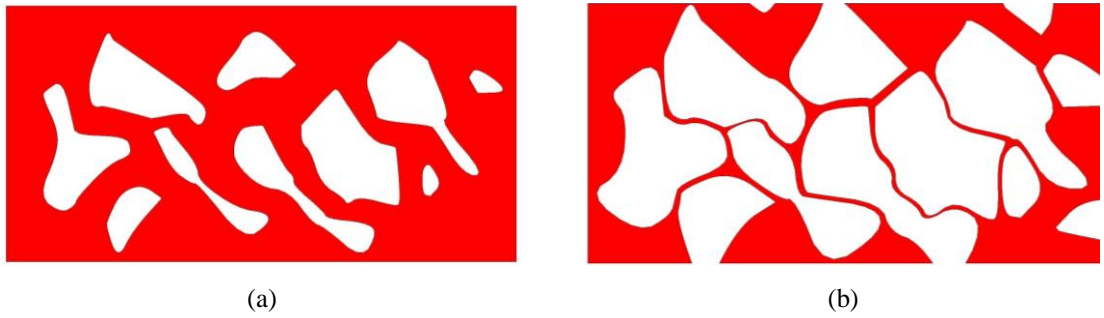


Figure 7.6. Porous structures with different porosities. (a) A porous structure modeled with the scaling factor $t = 0.4$. (b) A porous structure modeled with the scaling factor $t = 0.9$.

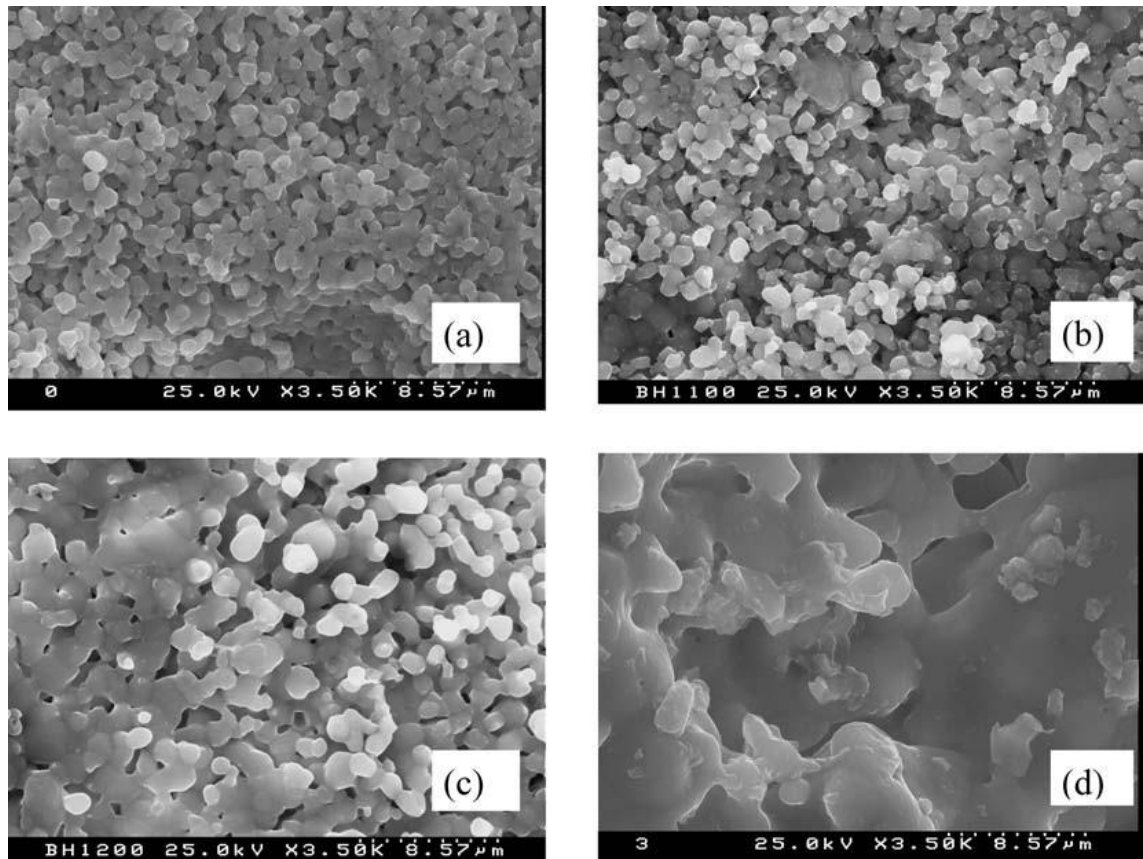


Figure 7.7. Microstructure of fracture surfaces of porous HA samples sintered at (a) 1000 °C, (b) 1100 °C (c) 1200°C and 1300 °C (d) (Goller et al., 2006).

7.3.2 2D finite element analysis of nanoindentation on a porous HA sample

A simple and effective geometric representation for irregular porous structure modeling is proposed. Study the hardness using nanoindentation on the hydroxyapatite samples. FE analysis has been done by MSC. Marc® software. The material properties are considered based on previous sections, which presented the alternative method to extract elasto-plastic parameters for HA material sintered on 1200°C (Naderi et al., 2015). Generally according to prior study all the conditions used in FE simulation are same as FE direct model (displacement control) except geometry for HA material that is implemented as a porous media (Naderi et al., 2015). The indenter is vertically applied on top surface and does not penetrate into a pore.

In order to study on effect of pores number through HA samples, four models have been generated using presented code in MATLAB, and then they were exported to MSC. MARC® to mesh and analyze the finite element models. Mesh generation in the models depends on distribution and shape of pores intensively, therefore refining mesh is necessary to avoid from further error. As shown in Figure 7.8 the number of pores increases for Figure 7.8 (a) to (b) and the dimension of all models are same ($5 \times 2.5 \mu m^2$). The numbers of generator points are 10, 20, 30 and 40; the scaling factor (0.5) and the criteria of polygon merging ($1 \mu m$) are constant for all.

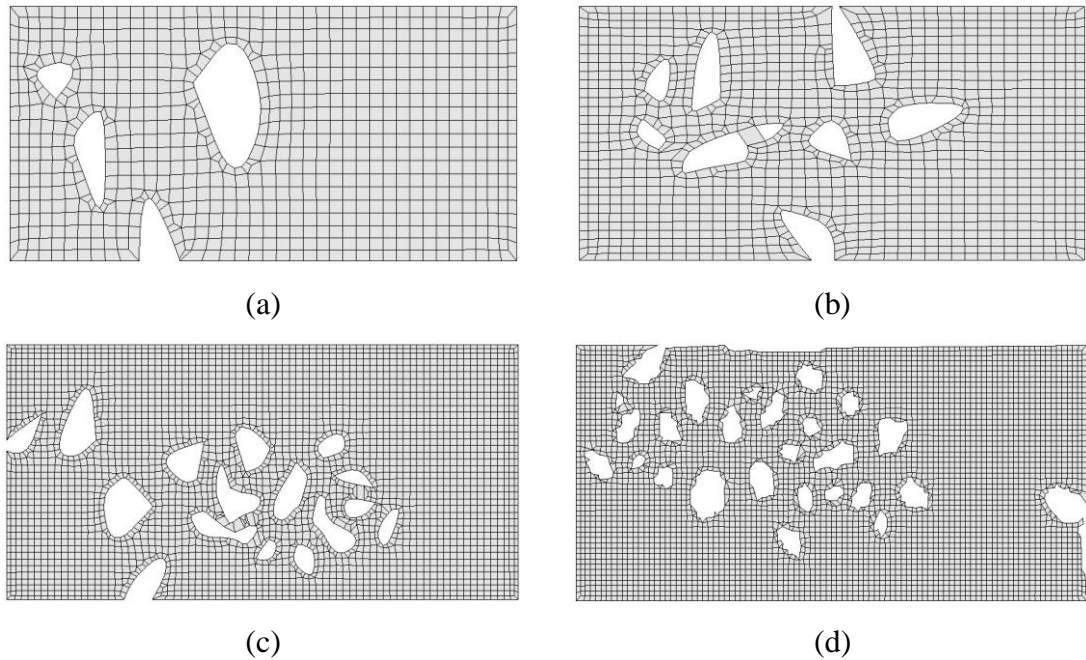


Figure 7.8. FE model of a designed irregular porous structures for different point generators (a) $n=10$, (b) $n=20$, (c) $n=30$ and (d) $n=40$.

Figure 7.9 illustrates Von Mises stress distribution after indentation on surface of HA models to indicate how the porosity can effect on deformation. In comparison to non-porous media (Figure 7.9(d)), stress concentration increases by increasing number of pores as it changes from 1.94 GPa in non-porous geometry model to amount of 3.816 GPa in the model with maximum number pores. The locations and in what way the pores distributes through the media cause to observe various responses to indentation loading. In Figure 7.9(c) the pores are located out of critical indentation zone therefore

maximum stress is 2.58 GPa, which is even lower than the model with minimum number of pores with maximum stress of 2.61 GPa (Figure 7.9(a)). It reveals that consideration of number and distribution of pores at the same time can be complicated since increasing number of pores concludes to higher stress concentration around indented point on the surface and the pores depended on its shape and location.

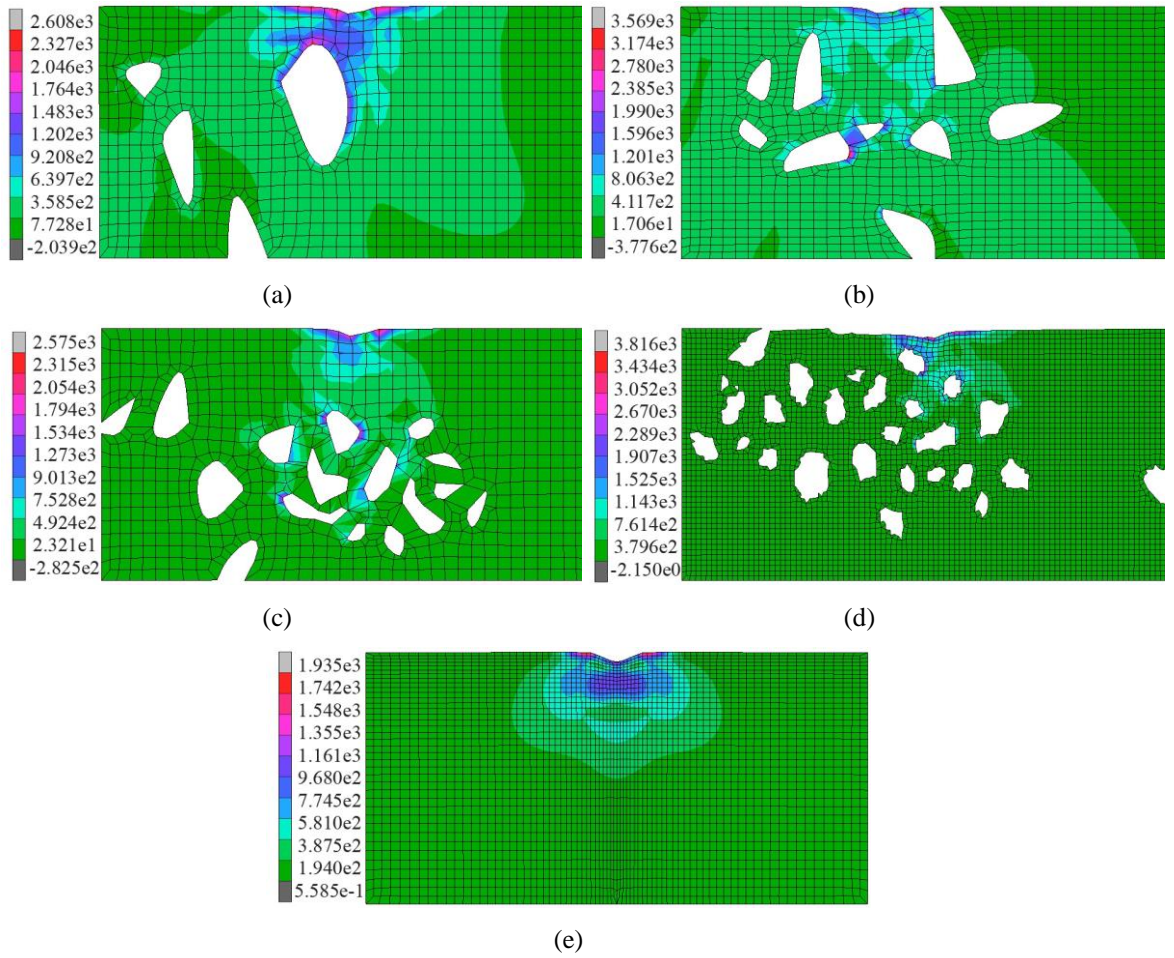


Figure 7.9. Equivalent Von Mises stress distribution [MPa] for indented HA sintered at 1200°C 2D models for different point generators, (a) $n=10$, (b) $n=20$, (c) $n=30$, (d) $n=40$ and (e) $n=0$ (non-porous).

Figure 7.10 shows force-displacement curves obtained from FE analysis for non-porous and porous geometry model subjected to nanoindentation test. The maximum force and indentation depth increase when the point generators and consequently number of pores increase, this matter can be related to distribution of pores; when the number of pores increases through the media, the geometry of material shows more homogenous behavior. Hence trends of the curves are getting close to the curve of solid structure by increasing of porosity. Figure 7.10 demonstrates the effect of porosity Comparative using only “numerical results”. In FE-model, HA was assumed as a “solid” and also a “porous” material, since the goal was generally to study how different

porosity effect on force-displacement curve in one material. Therefore HA at 1200 °C was considered both solid and porous.

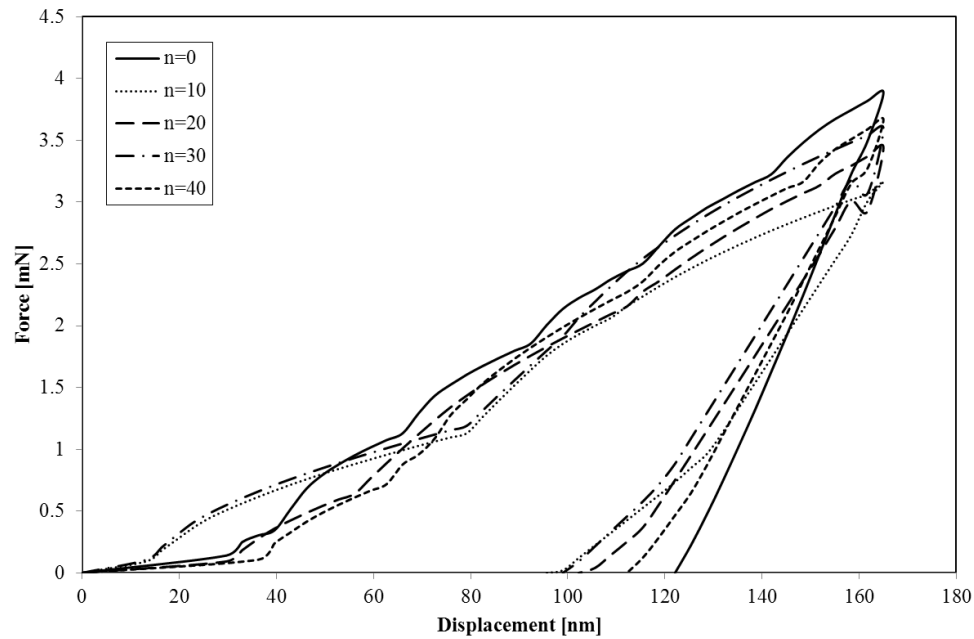


Figure 7.10. Effect of porosity on predicted force-displacement curves obtained from 2D finite element analysis of indentation (HA material properties at 1200 °C and n, number of point generator).

7.3.3 Results of a 3D HA porous solids

As we discussed in previous chapter, the idea for design of a 3D porous structure has been taken from MRI process. In MRI, the signals are received by a computer that analyzes and converts them into 2D images as a layer of the body structure or organ being examined and then the layers will be combined. However in this study, 2D porous layer are produced by MATLAB code artificially, which the code is able to control porosity in each layer. The layers are merged in FEA software, consequently the pores and percentage of porosity are able to be controlled by user.

3D finite element analysis for nanoindentation test has been done based on the method used in previous chapter for HA sintered at 1200°C. Equivalent Von Mises stress distributions are illustrated in Figure 7.11 at maximum load (right) and end of indentation. Maximum equivalent Von Mises stress is about 4 GPa and 7 GPa at the

middle and after indentation respectively. However this amount is almost equal for these two structures but the stress distribution is completely different. The response of the models to the indentation loading is unlike. These two moments were selected to capture the top surface of the models because the first is at maximum loading and depth to indicate the behavior of the samples in maximum posed stress; The second is at the end of indentation subjected to demonstrate the difference of the indented surfaces.

At the moment of maximum indentation and for the porous geometry (Figure 7.11(a)), stress distributes through bigger volume in comparison to the solid structure at the same moment(Figure 7.11(b)). As it was discussed before, the pores play a significant role in stress distribution. They cause stress to be allocated around of pores, consequently the stress concentration is not only around of the indentation zone.

After indentation and unloading, for the solid structure, which had more stress concentration through the indentation zone, the stress distribution area is bigger than the porous geometry (Figure 7.11). Also it can be explained using stress-strain curve for the indentation point at the center of surface (Figure 7.12).

According to Figure 7.12, the amount of stress for the porous model is lower than the solid one. So the porous geometry shows more brittle behavior in comparison with the solid structure. Although it can be expected that the trend of stress-strain curve for a sample with porosity is functional. Since it depends on how the pores are located in the model. The behavior of HA seems to be rigid-plastic material around the indented zone. In general HA is a ceramic and brittle material, but as microscopic point of view, the indentation tests have been done in “nano-scale” in this study. The plastic deformation can be considerable in comparison with elastic displacement and indentation depth in this scale (Figure 7.12), in this case material model can be considered as elastic-plastic.

It was mainly proposed to present a method, which is able to generate an irregular porous geometry in current study. In order to study on application of this method plus effect of porosity, the porous geometry was implemented to the direct FE-model.

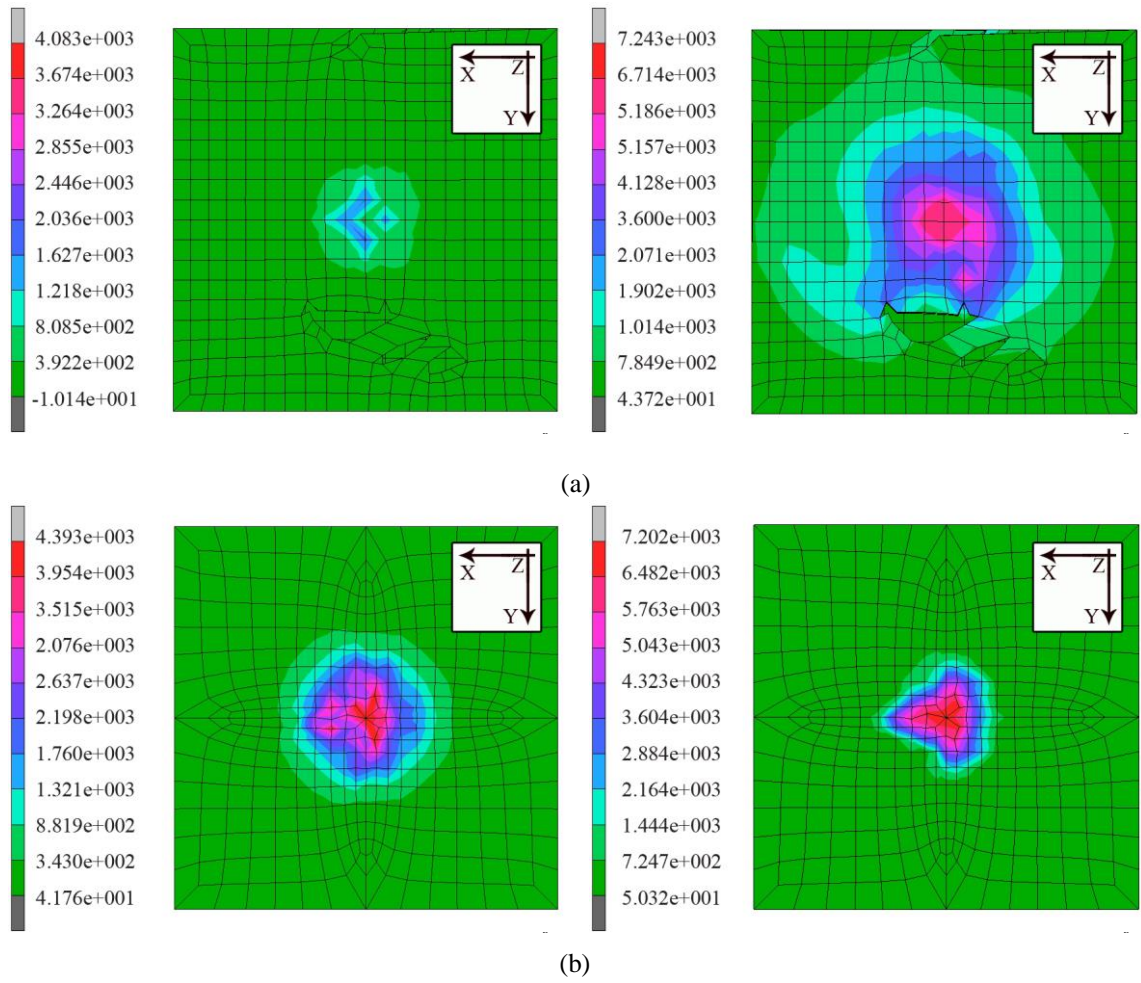
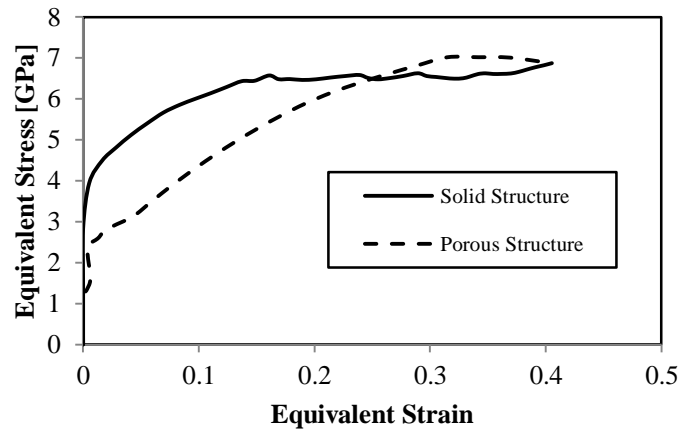


Figure 7.11. Equivalent Von Mises stress distribution [MPa] on the top surface and at the end of indentation (left), and maximum load/depth (right) for HA sintered at 1200°C 3D models for (a) porous and (b) solid geometries.



(a)

Figure 7.12. Expected stress-strain curve of the central point in indentation zone obtained from FE-model for solid and porous HA model.

7.4 Impact induced damage and failure modes in GFRP samples

7.4.1 Force-deflection diagram

Figure 7.13 illustrates the F-d diagram for GFRP laminates with thicknesses of 2 and 3mm. Two damage modes clearly exist. A drastic fall in contact force in the F-d diagram pertains to the first damage mode involved in this situation. The F-d diagram has a closed structure due to low initial impact energy (9.8J). Here, the impactor rebounds since in the downward part of the graph the force value and deflection decrease concurrently in the unloading phase. This damage mode includes matrix cracks and bending of fibers that are visible on non-impacted surfaces. Fiber fractures are attributed to bending deflection and fiber separation from the matrix that lead to diminished specimen bending stiffness. This is reflected in the plateau area of the F-d graph (a nearly constant force value with changes close to a particular amount).

Figure 7.13a indicates an open curve form of the Force-deflection diagram for impact energy of 19.6J. Increasing the energy level results in rising maximum force at

the impact moment. Nevertheless, for 2mm thickness where perforation occurred, the force peak is less than the impacted plate by 9.8J of energy. The reason is that perforation causes a drastic decline in bending stiffness. In the unloading phase, force alters sharply and causes unstable behavior of the perforated laminate. In Figure 7.13b the graph does not have a completely open form for 3mm plate thickness and 19.6J of impact energy. In this state, the laminated plate is at the threshold moment when the plate is about to be perforated. In the first instant of the unloading phase, deflection grows and then it decreases. For a clearer view of the impact process, photographs of the damaged laminates with 2 and 3mm thicknesses were taken (Figure 7.14 and Figure 7.15, respectively). The impacted surface (front) and the non-impacted (back) show damage propagation for 9.8 and 19.6J of energy. Composite behavior changes when thickness is increased up to 4mm, and consequently, impact response alters.

The F-d diagram for 4mm thickness is presented in Figure 7.16. In the unloading phase, force value variation is insignificant in the thin plates (2 and 3mm) since the contact force is imposed onto all lower and upper layers. Also, all layers are affected by the same force magnitude so the contact force will increase proportional to the deflection (Figure 7.16). After the laminate absorbs sufficient energy, the damage mechanism will be activated and cause a decrease in bending stiffness and contact force. For thick plates (4mm), the layers are in contact with the impactor head from the upper to the lower layer respectively, causing a tremendous drop in force value. Unlike the thinner plates, there is a plateau region around the peak force. When the initial impact energy increases to 29.4J, the impactor rebounds without perforating the surface of the plate. The photographs of the damaged laminate in Figure 7.17 confirm this.

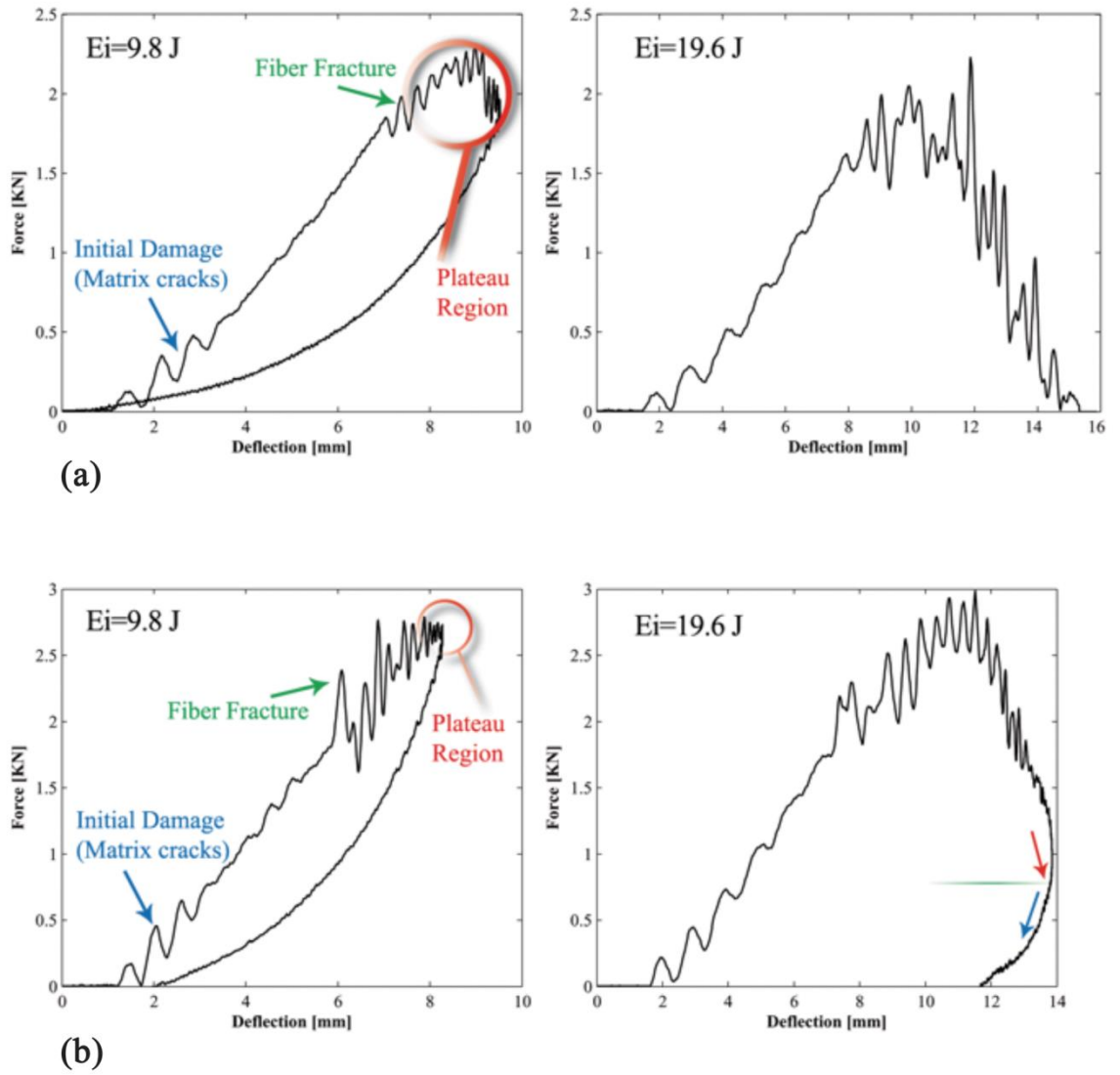
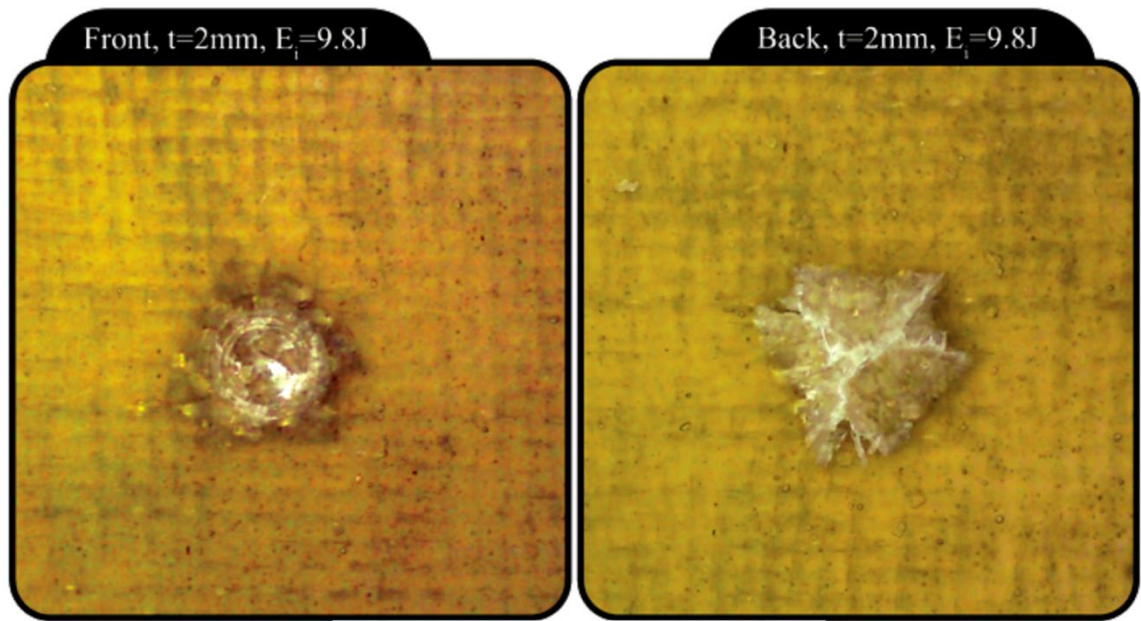
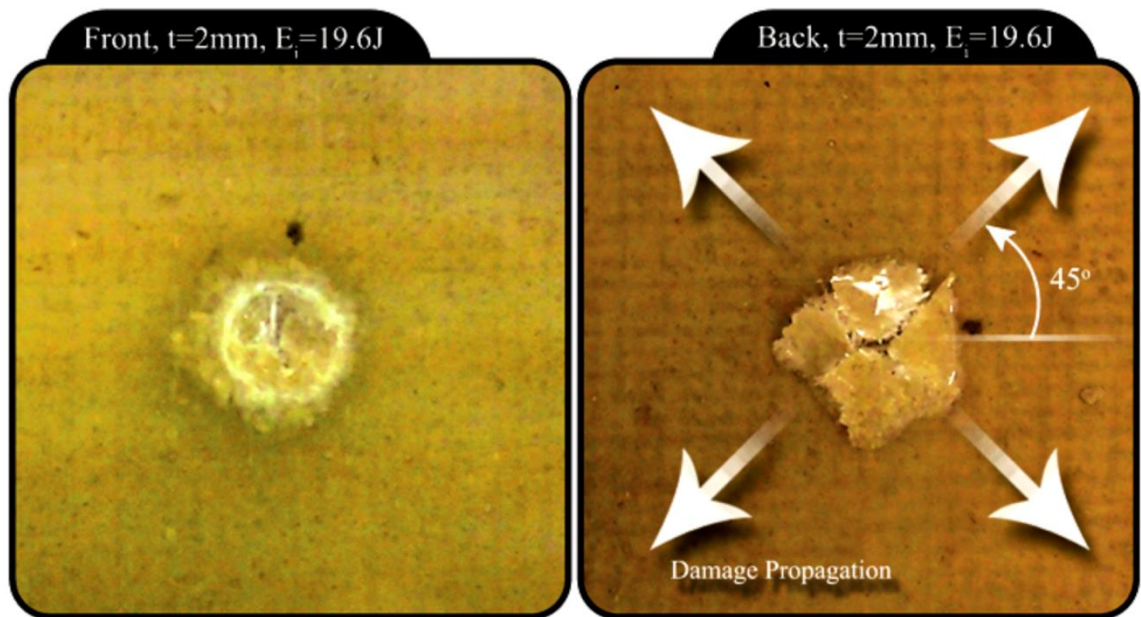


Figure 7.13. F-d diagrams for impact energies of 9.8 and 19.6 J on samples with thicknesses of: (a) 2mm, and (b) 3 mm.

The direction of woven e-glass/epoxy propagation depends on the path of the fibers in each layer. For $[0/90^\circ]$ fibers, the laminate is reinforced in 0 and 90-degree directions, thus the plate is weaker in the 45-degree direction; consequently, the damage propagates in these directions as illustrated in Figure 7.14, Figure 7.15 and Figure 7.17. The matrix in cross-fibre laminate composite is reinforced in 0 and 90 degree and it is an orthotropic material. The elastic modulus and the strength are more along fibre directions . Hemispherical impactor induce the tensile stress in back-face (non-impacted face), so the matrix are stronger in fibre directions. Damage in matrix can be propagated in 45 degree (Serge Abrate, 1991; Belingardi et al., 2008).



(a)



(b)

Figure 7.14. Photographs of front and back surfaces of the impacted samples with 2mm thickness after impact with different impact energy and damage propagation values in the 45° direction in woven fiber laminate. (a) Initial energy=9.8 J, and (b) Initial energy=19.6 J.

Bending stiffness K_b is defined as the slope of the line that fits the loading section of the F-d curve. In this sense, K_b is a material constant that does not depend on impact energy. Figure 7.18 portrays the loading segments of the F-d curves for different impact

velocities and plate thicknesses of 2, 3 and 4mm. It is clear that the bending stiffness K_b increases as the thickness and number of layers increase. In turn, the response of low-velocity impact is affected too. Table 7.3 lists the bending stiffness versus number of layers, which is almost constant at 0.1ton/ms^2 .

Table 7.3. Bending stiffness for different thickness (in parentheses an amount of k_b per number of layers).

Thickness [mm]	2	3	4
K_b [ton/(ms) ²]	0.29 (0.097)	0.38 (0.076)	0.57 (0.095)

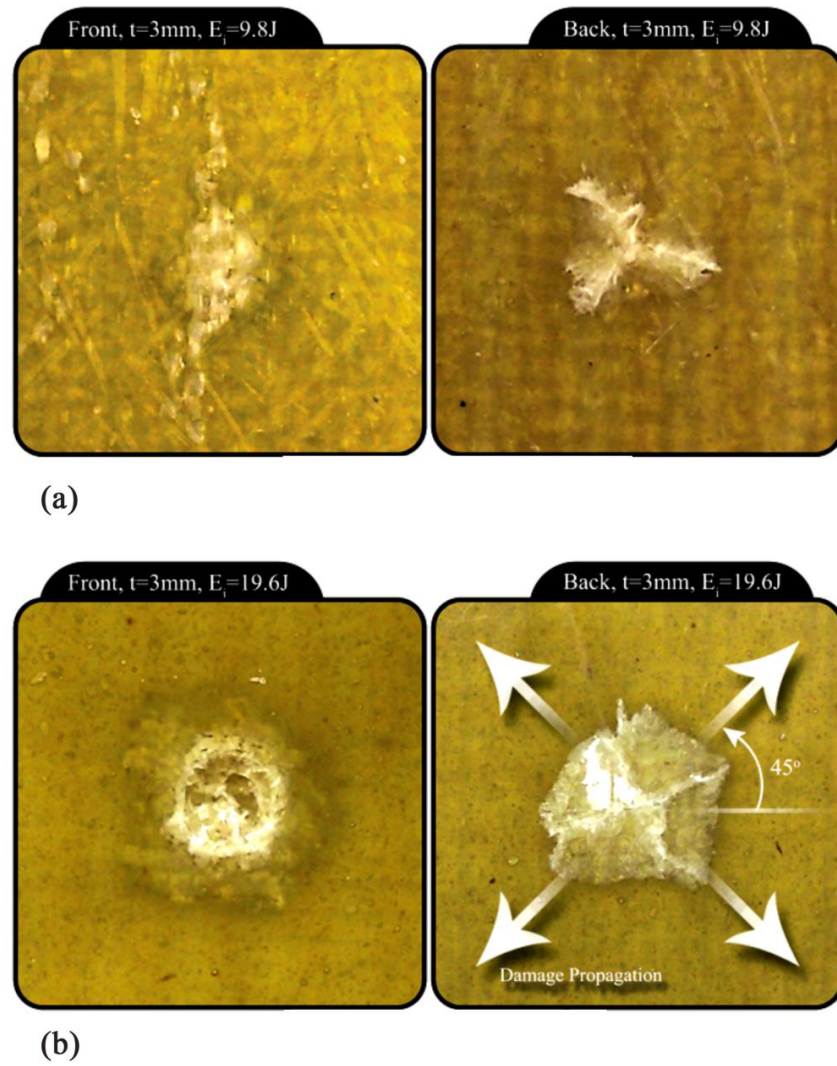


Figure 7.15. Photographs of the front and back surfaces of impacted samples with 3mm thickness after impact with different impact energy and damage propagation values in the 45° direction in woven fiber laminate. (a) Initial energy=9.8 J, and (b) Initial energy=19.6 J.

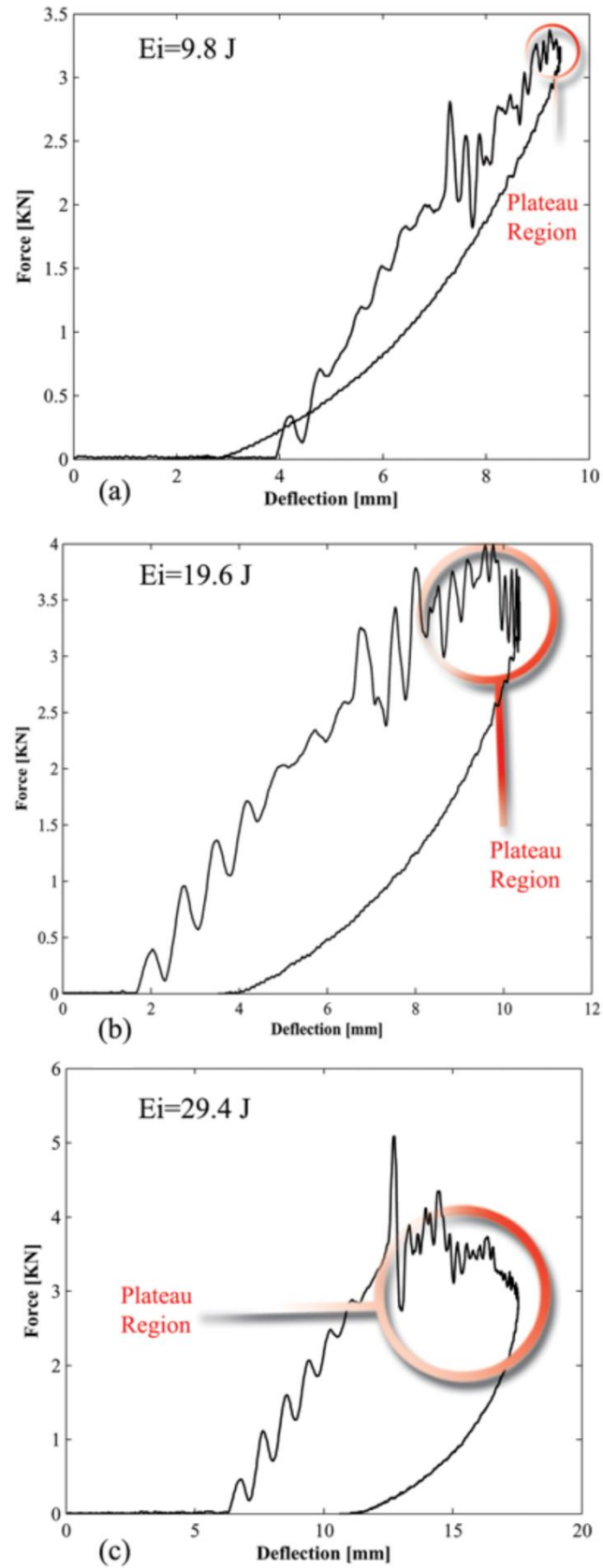


Figure 7.16. F-d graph for sample with 4 mm thickness and impact energy: (a) 9.8 J, (b) 19.6 J, and (c) 29.4 J.

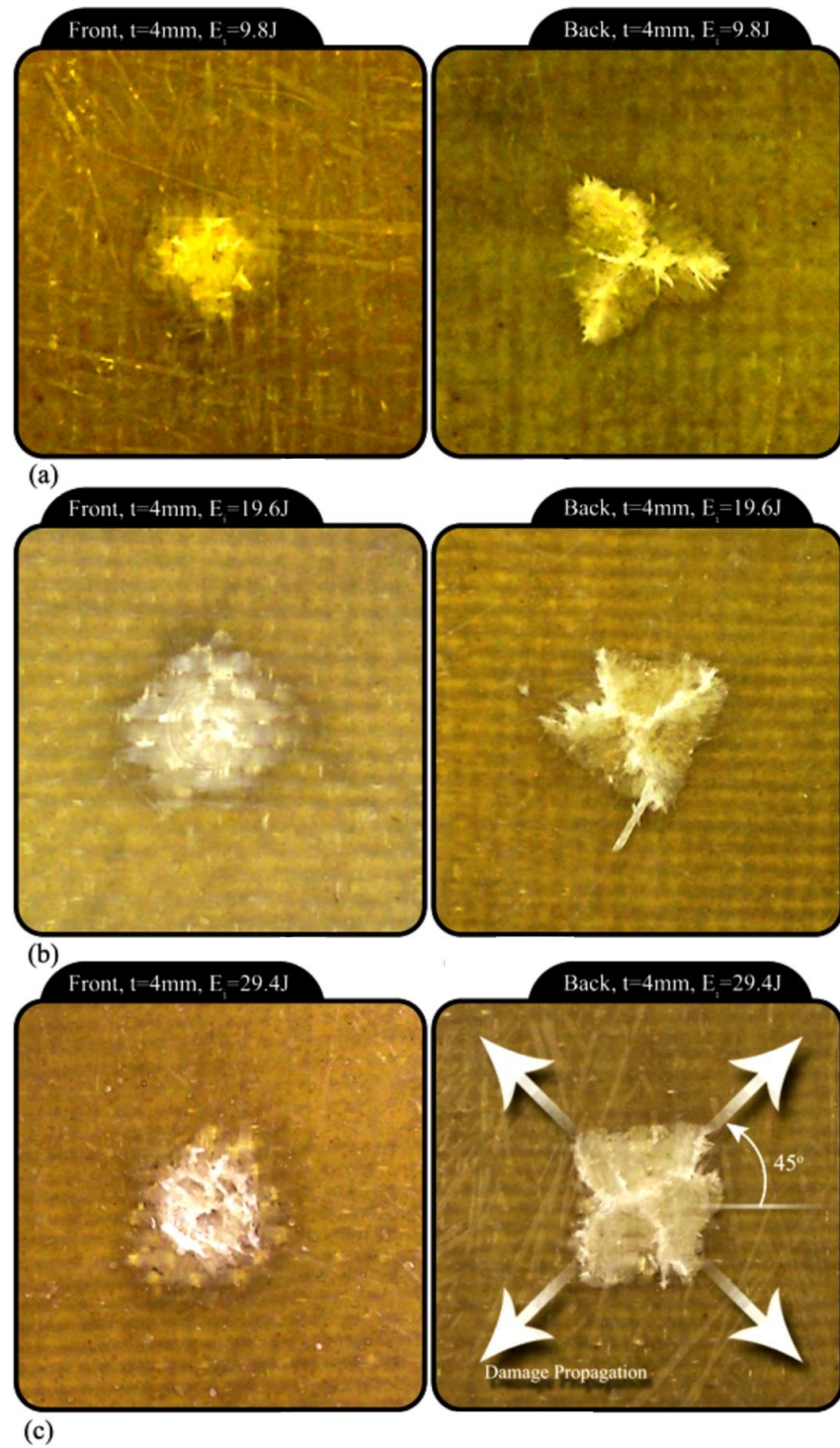


Figure 7.17. Photographs of front and back surface of the impacted samples with 4 mm thickness after impact with different impact energy and damage propagation values in the 45° direction in woven fiber laminate. (a) Initial energy=9.8J, (b) Initial energy=19.6J and (c) 29.4 J.

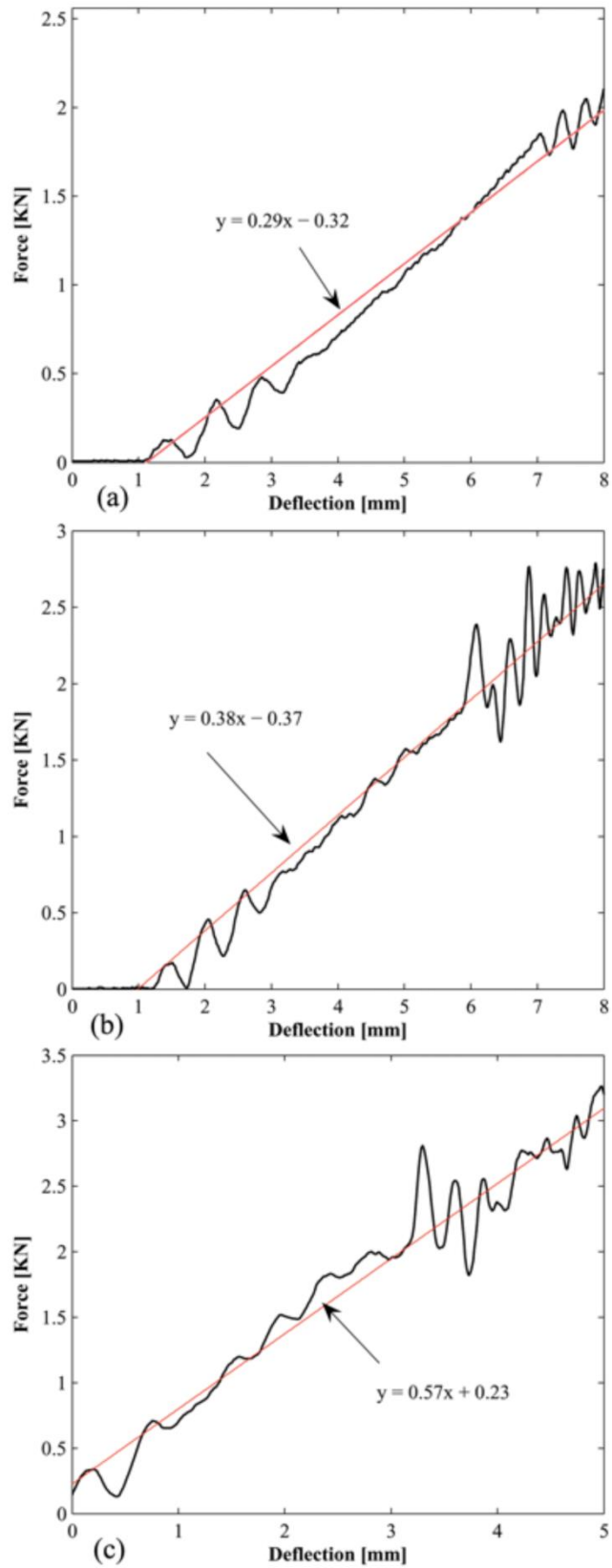


Figure 7.18. F-d diagram in loading phase with impact energy of 9.8J for: (a) 2mm, (b) 3mm, and (c) 4mm thickness.

7.4.2 Force-time diagram

The contact force can be defined by the reaction force between the plate and the impactor. In the experiments, this force was recorded by the load cell while the other parameters including velocity and deflection were calculated using the history of force. Figure 7.19 illustrates the force-time curve for three thicknesses and the range of impact energies. For instance, when the impact energy is low (9.8J), the obtained curve is parabolic and variations in force value with time are insignificant. MSC.MARC® runs were conducted with three impact energies and thicknesses. The force-time plots were compared with the experimental results. Figure 7.20 shows the force-time diagrams, which resulted from the finite element simulation analysis. The behavior of E-glass/epoxy laminates can be interpreted through this diagram. As Figure 7.20 indicates, the FE simulation model overestimates the maximum load carrying capacity when the damage is significant and the impact time is below the experimental values. The failure criteria employed in the proposed FE-model is not accurate for the laminates because perforation is deemed the dominant damage mode. The FE results signify that the modeled material is slightly stiffer than the actual one.

The maximum force increases slightly as initial impact energy increases. The same as for the F-d curves, a drastic fall in contact force is observed after 8ms due to bending fracture of fibers in the lower surface (non-impacted). The maximum force value also increases with augmenting thickness. Figure 7.21 shows the maximum amount of force with respect to bending stiffness for impact energies of 9.8J and 19.8J. It indicates a linear relationship for Glass/Epoxy laminate with respect to impact. The impacted plate of 2mm thickness is perforated, so the force value decreases by increasing the energy level. As seen in Figure 7.19 and Figure 7.20, the maximum load increases with increasing impact energy. This indicates that the maximum impact load of the laminates has not yet reached a saturation level where considerable damage or perforation would

occur. The contact time shortens as thickness increases and the obtained curve is parabolic; however, the time for peak force is almost constant at roughly 8ms.

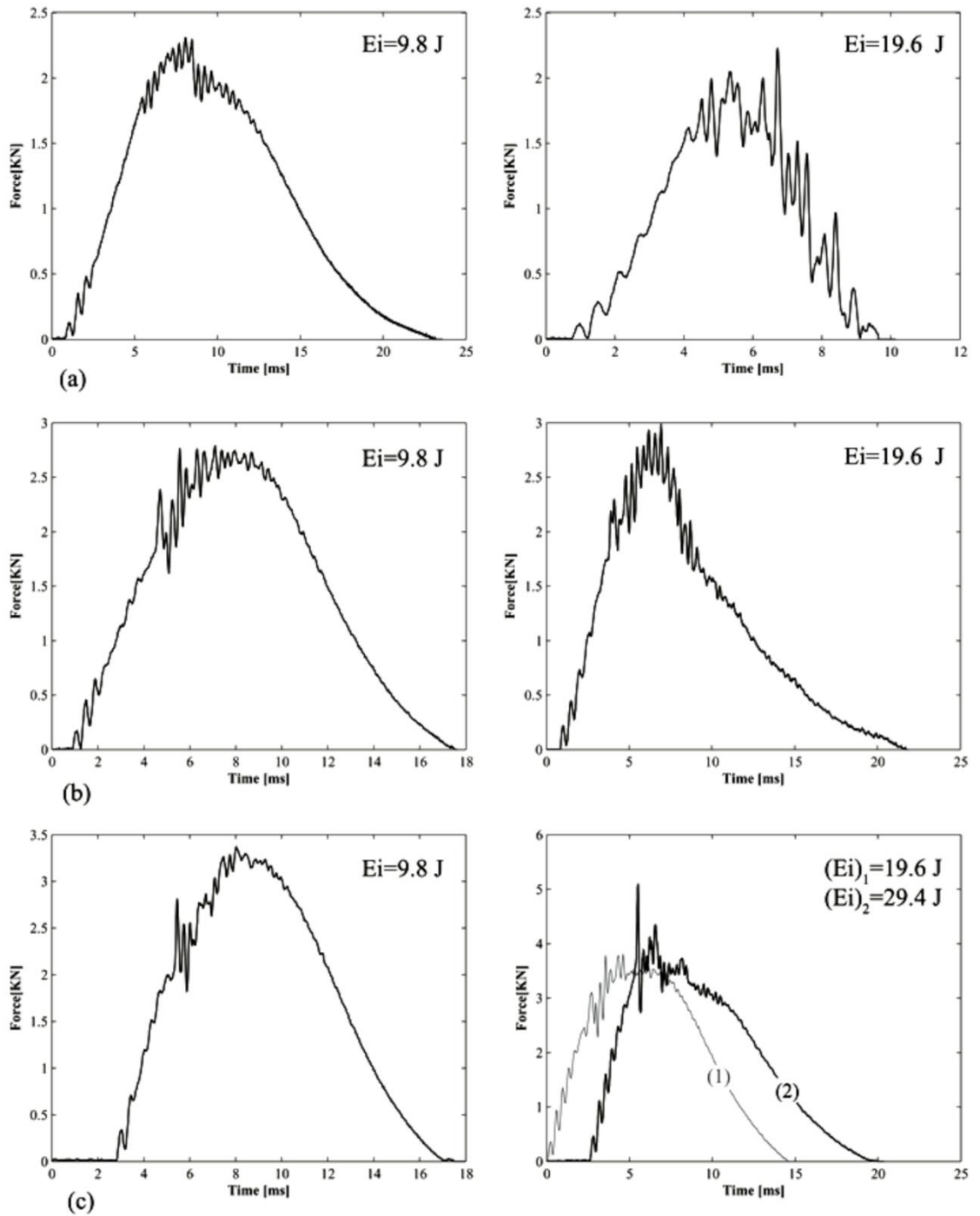


Figure 7.19. Experimental force-time curve for different impact energies and thicknesses: (a) 2 mm, (b) 3 mm, and (c) 4 mm.

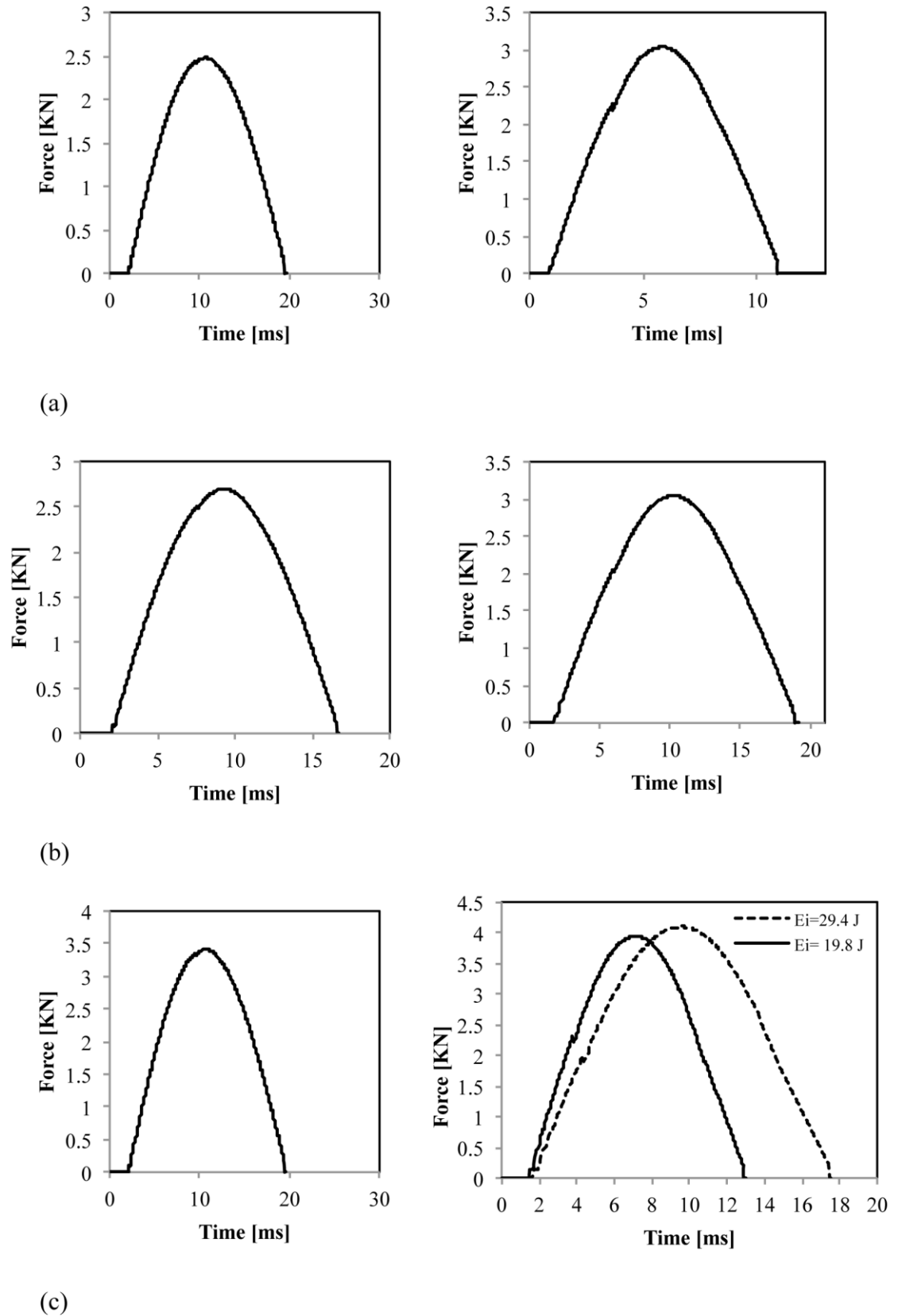


Figure 7.20. FE-simulation results for force-time curve under different impact energies and thicknesses: (a) 2 mm, (b) 3 mm, and (c) 4 mm.

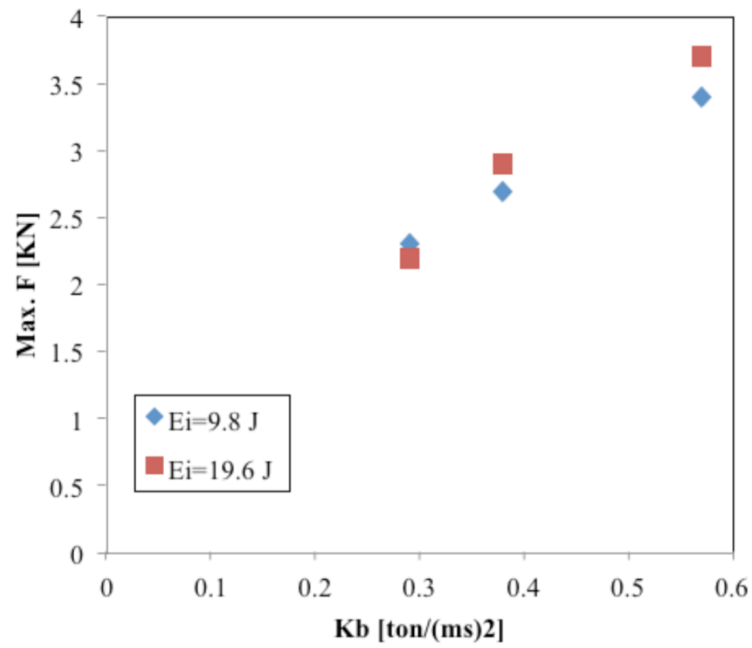


Figure 7.21. Maximum contact force–banding stiffness for Glass/Epoxy laminate for impact energies of 9.8 J and 19.6 J.

7.4.3 Deflection-time diagram

Figure 7.22 illustrates the deflection-time (d-t) diagram for 2, 3 and 4mm sample thicknesses. The maximum deflection is observed approximately at the instant of greatest contact force with a small delay. After the impactor reaches the peak deflection point, it continues to shift to the left side of the time axis. Contrary to the F-t diagram, the location of the peak value is constant for different thicknesses, but for the d-t curve, the maximum deflections times are 10.8, 9.7 and 9ms respectively for 2, 3 and 4mm thicknesses (impact energy is 9.8J). In Figure 7.22a, the d-t curve demonstrates that the impactor does not rebound to the initial place for the perforated plate and finally, the curve ascends for the perforated laminate in the d-t diagram.

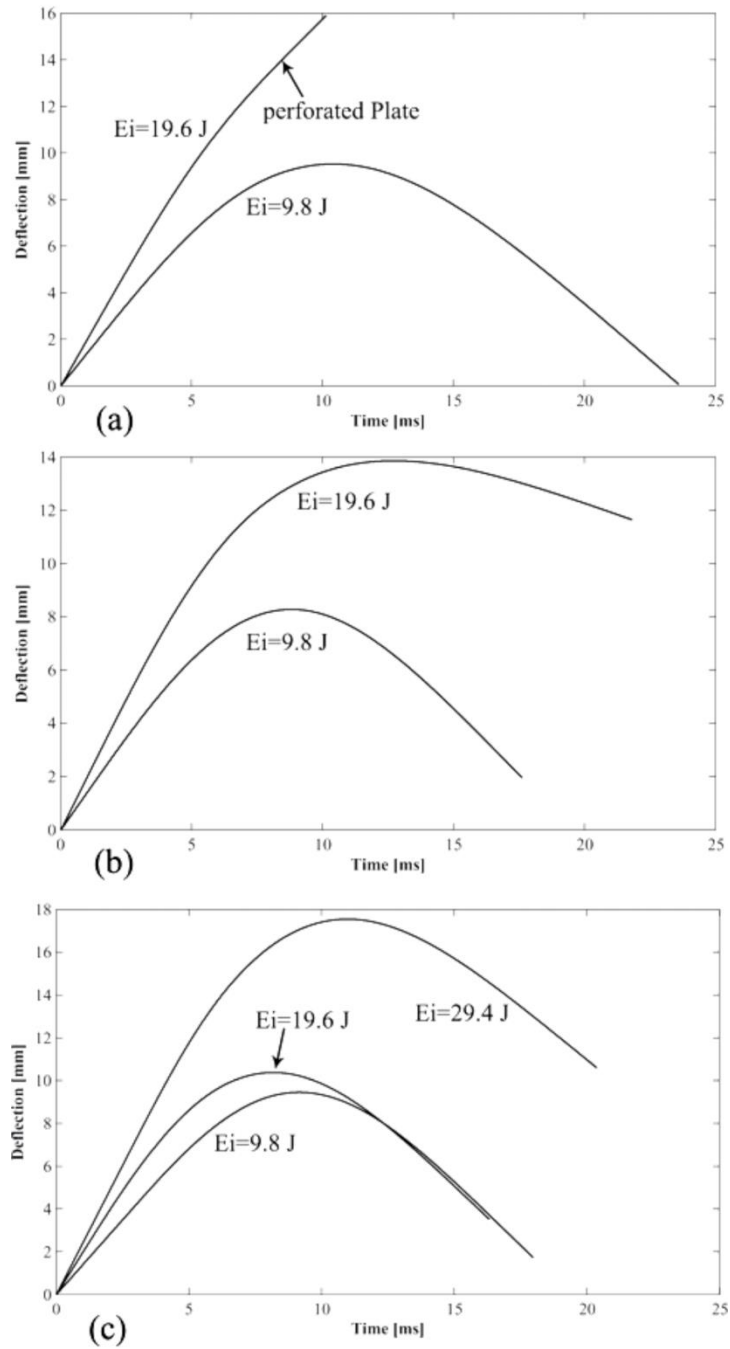


Figure 7.22. Variation of deflection versus time under different impact energies for the samples with different thickness: (a) 2 mm, (b) 3 mm, and (c) 4 mm.

7.4.4 Velocity-time diagrams

Figure 7.23a-c show velocity versus time at various impact energy levels as well as 2, 3, and 4mm thicknesses. Each graph's maximum velocity is at the beginning of the impact event.

When there is no perforation and the laminate has maximum deflection, the velocity value reaches zero for the rebounded impactor, after which the impactor moves in the reverse direction and velocity grows. For the perforated sample, the velocity does not change sign because the impactor does not rebound but instead keeps going through the laminates. For the impacted laminate with 3 mm thickness at 19.6J of energy, the velocity is near zero at the threshold of perforation.

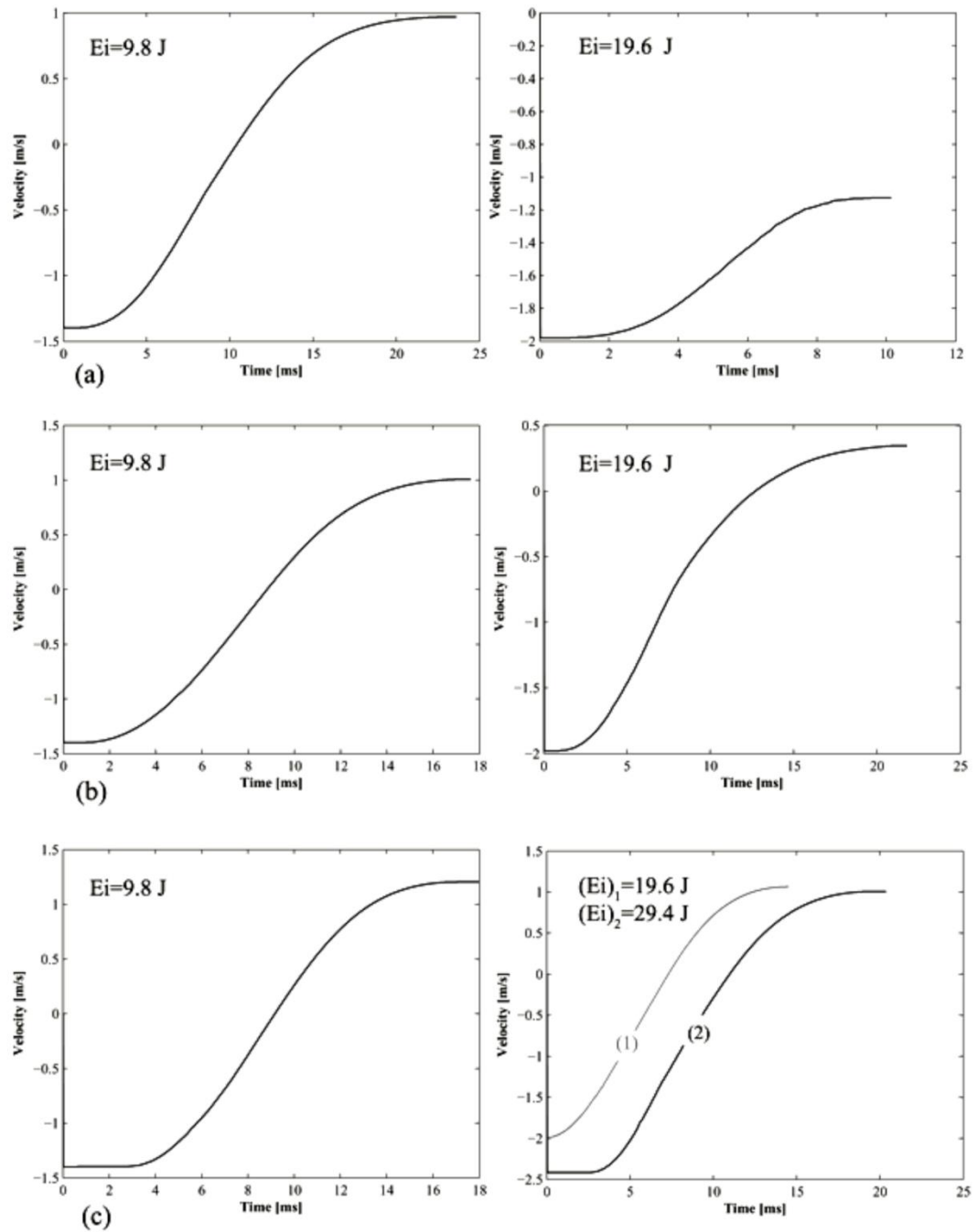


Figure 7.23. Variation of velocity versus time under different impact energies for the samples with different thicknesses: (a) 2 mm, (b) 3 mm, and (c) 4 mm.

7.4.5 Velocity-deflection diagram

Impactor velocity versus deflection is illustrated for different impact energies in Figure 7.24a-c. As with the v - t curve, the maximum velocity value is detected just before the incident. The velocity-deflection diagram (v - d) is parabolic when the impactor returns, and velocity is at a maximum when deflection is zero. If the sign of velocity changes, the impactor will reverse in direction and then will return to its original point. Figure 7.24a denotes the v - d graph for a perforated plate by initial impact energy of 19.6J. The curve is uni-directional as the velocity value decreases and deflection rises.

The impactor is stopped by a pneumatic automatic brake installed on the machine in order to avoid multiple impacts. Consequently, data is recorded until the impactor returns to its original place. Thus, one portion of the v - d curve is estimated and is shown by the dotted line. Return velocity can be evaluated with this approximation.

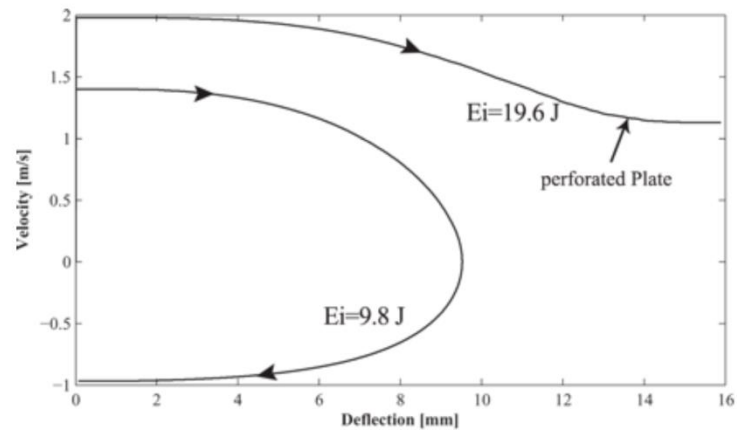
The slope of the v - d curve indicates disparities of strain rate ($d\dot{\epsilon}$) which has a higher value in the loading phase as opposed to the unloading phase when the impactor returns from the surface. Initial velocity (v_i) and return velocity (v_r) are given in Figure 7.25. The ratio of return velocity to initial velocity ($\frac{v_r}{v_i}$) decreases while the amount of impact energy increases; otherwise the drop in the diagram is associated to the damaged composite plates.

The amount of $\frac{v_r}{v_i}$ ranges between 0 and 1, meaning that:

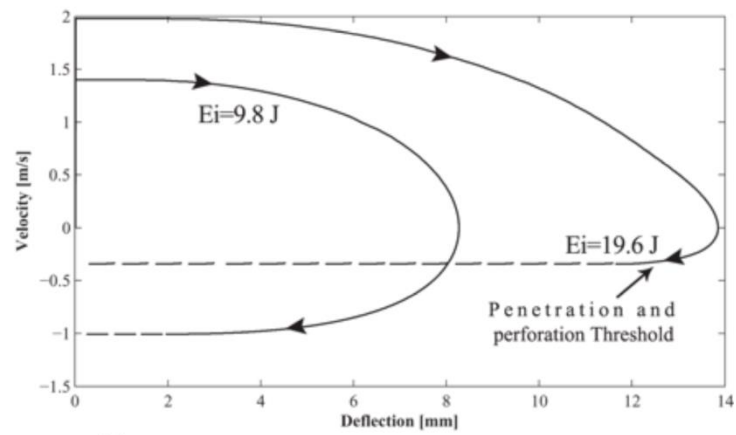
$$0 \leq \frac{v_r}{v_i} \leq 1 \quad \text{Eq. 7.2}$$

When $\frac{v_r}{v_i}$ equals 1, the impact is completely elastic. If $\frac{v_r}{v_i}$ equals 0 or is almost zero, the laminate is at the threshold moment of perforation (Figure 7.24b).

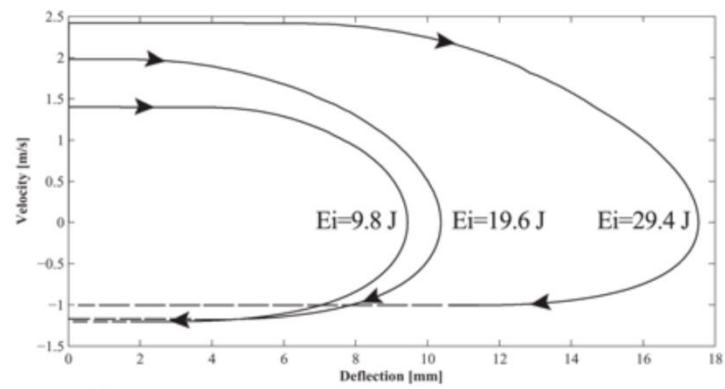
For comparison, the return velocities calculated from Figure 7.24a-c are shown in Figure 7.25. It is clear that for a given constant energy level the return velocity v_r of the impactor and velocity ratio $\frac{v_r}{v_i}$ increase as the composite laminate becomes thicker. Since the value of $\frac{v_r}{v_i}$ describes the laminate behavior under impact, it can be considered an index for the expected amount of damage.



(a)



(b)



(c)

Figure 7.24. Velocity-time diagram for the samples with different thicknesses: (a) 2 mm, (b) 3 mm, and (c) 4 mm; (follow-up of curve is estimated).

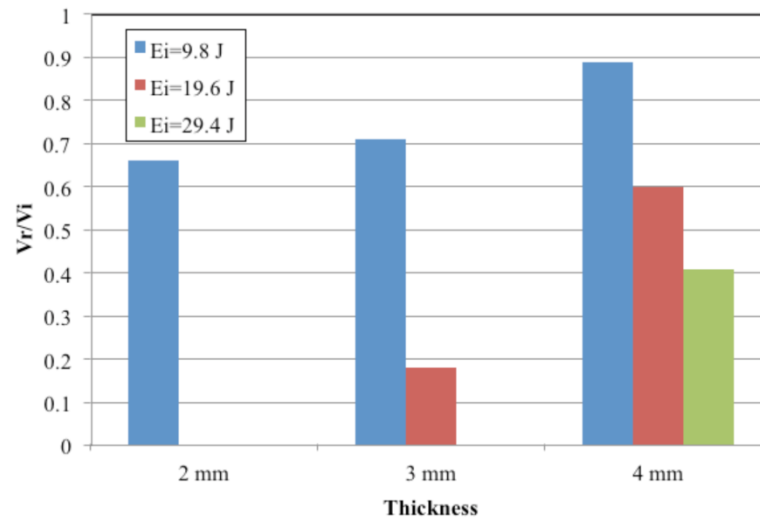


Figure 7.25. Ratio of return velocity to initial velocity versus plate thickness for different impact energies.

7.4.6 Energy-time diagram

The transferred energy respect to contact time (K-t) is illustrated in Figure 7.26 for different impact energy levels. Initial impact energy increase causes to absorbed energy increase till this energy makes more damage progress in the composite plates.

Figure 7.26 indicates that all curves have upward tide in the loading phase and after pick point, which equals initial impactor energy, energy value goes down, this part is the unloading phase. The downward trend continues till the specific amount then the energy value becomes constant. The difference between the final absorbed energy and the maximum energy shows elastic energy. This energy is equal to value that transfers back to the dart and also the return impactor velocity is calculated using elastic energy. The perforated plate is an exception and its trend is dissimilar. For the specimens with 2 mm thickness that is perforated, K-t curve does not increase till the initial impact energy value since the laminate absorbed the critical energy value which is required for perforation and just a fraction of first impact energy. In this case, the initial energy is 19.6 J and the maximum energy equals 13.25 J, the difference is equivalent to the residual energy that causes impactor to move through the plate without rebounding. After perforation phase, the friction between the impactor and the plate dissipates a

portion of the residual dart energy. In the experimental results due to the brake system, which was applied to prevent multiple impacts, the K-t curve is not able to indicate the friction-dissipated energy. Figure 7.27 shows that the curve eventual path was estimated by the dotted line given the friction notwithstanding this value is insignificant.

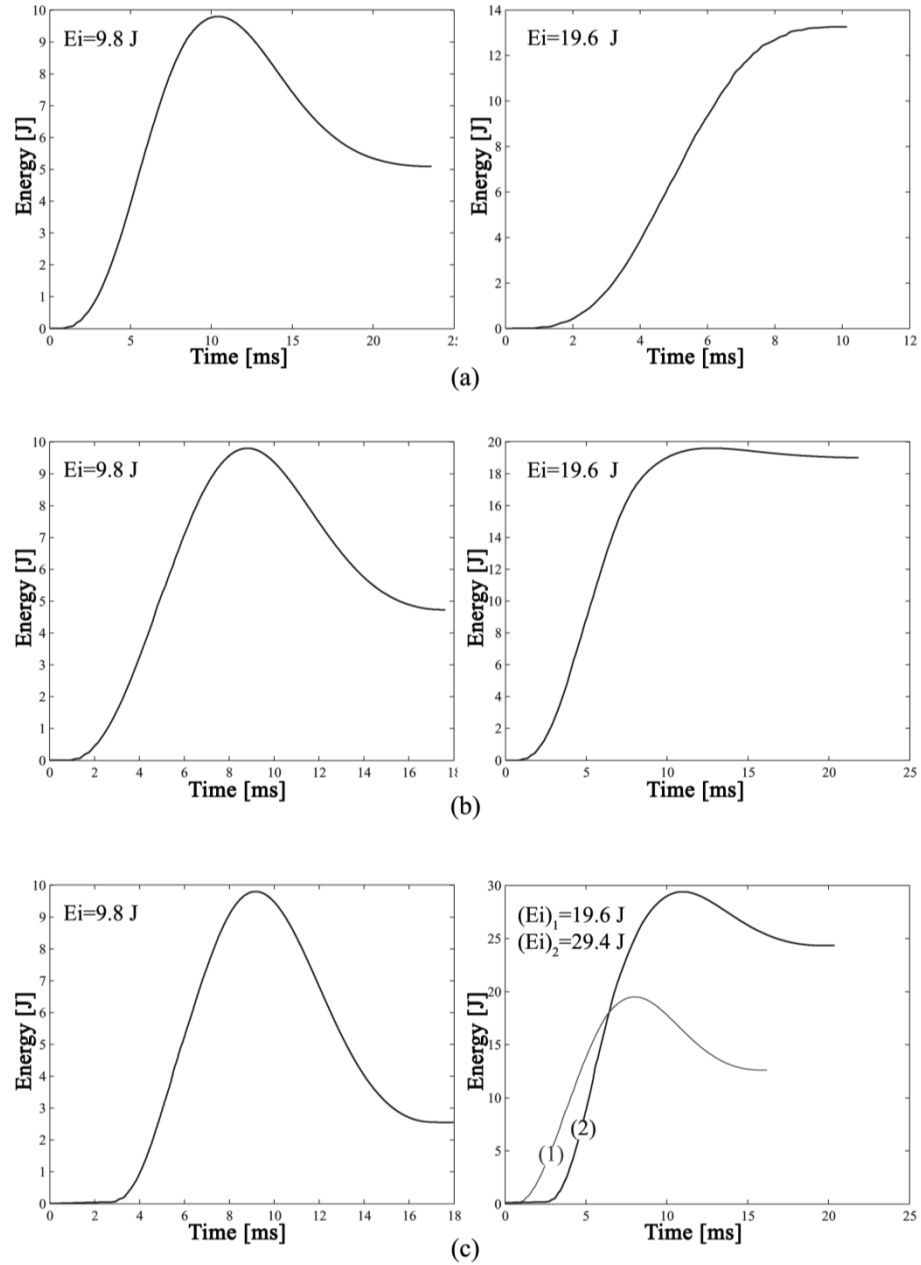


Figure 7.26. Curve of the transferred energy to the composite specimens versus time for different sample thicknesses: (a) 2 mm, (b) 3 mm, and (c) 4 mm.

7.4.7 Energy absorption versus number of layers

Since the response of GFRP composite after low-velocity impact event is important to have a safe component design, in this research the absorbed energy respect to the initial impact energy to the number of layers of laminates was considered. It describes the behavior of glass fiber reinforced composites under low-velocity impact load (Figure 7.28). The curve will decrease after it reaches to maximum value; this point is equal to critical energy amount, which separates the curve to two part, the upward part relates to pre-perforation and downward part estimates the step after perforation. Finally, the critical energy in Figure 7.28 approximates the initial impact energy that causes impactor to perforate the laminated composite given the number of layers. As it is shown in Figure 7.28 a curve has been fitted from the experimental data. The advantage of this curve and its equation is to evaluate the GFRP composites capacity in energy absorption; For instance according to the equation of the fitted curve, the specimen with 3 mm thickness, 5 layers and 25 J initial impact will be perforated, on the other hand the experiments verified it because a plate with 3 mm thickness and 19.6 J was close to the perforating conditions and impactor rebounded from the specimen surface. This matter can be described by Figure 7.26b and Figure 7.28, the graph trend indicated the absorption energy value, in other words if impact energy increases to 25 J, the impactor will stop and the plate will be at the perforating threshold.

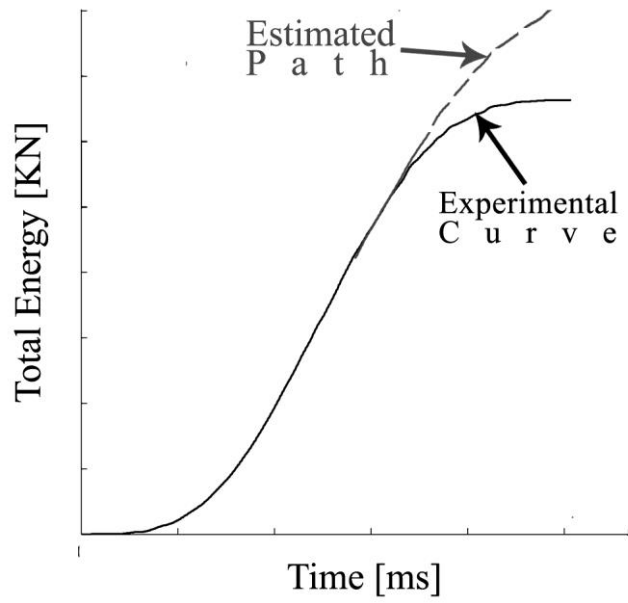


Figure 7.27. The schematic of K-t Curve for 2 mm perforated specimen by 19.6 J impact energy.

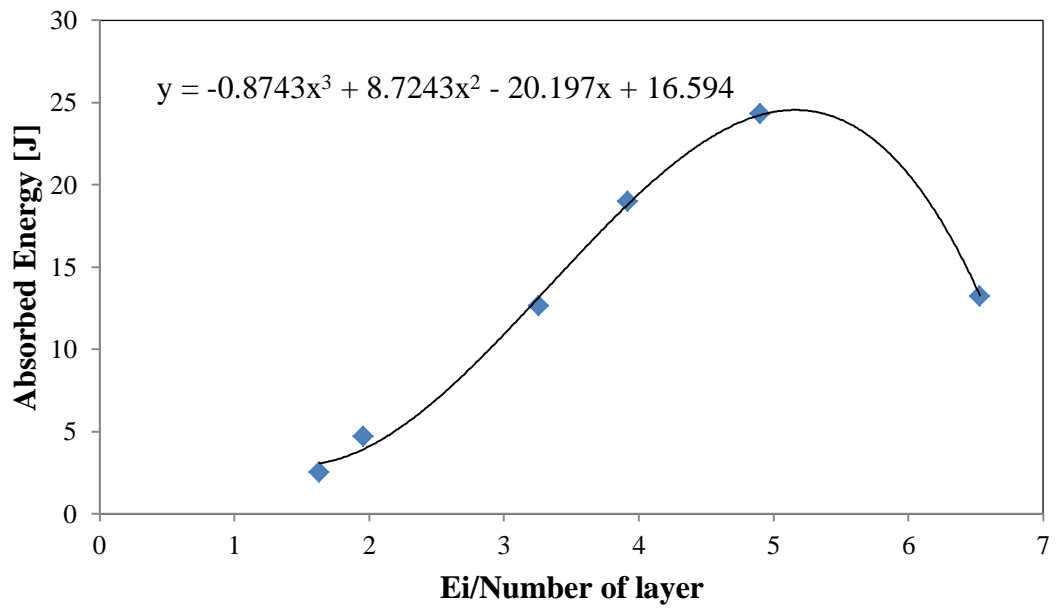


Figure 7.28. Absorption energy respect to ratio of initial impact energy to number of layers.

For the experimental approach, it is verified that impact energy level and thickness value can influence on the dynamic response of composite plates. The graphs of energy-time are used in order to describe the mechanical behavior of the specimens, which is

represented by graph of the absorbed energy versus ratio of impact energy level to number of layers. In Figure 7.28 the upward part can be divided into three regions:

1. Region 1: the specimens have a quasi-elastic behavior, because the fraction of absorbed energy is very low (under 35%) as failure mechanisms are not activated;
2. Region 2: the specimens show some failure mechanisms, which are matrix crack and delamination; so, the fraction of absorbed energy is intermediate between 35% and 75%;
3. Region 3: the specimens show many types of failure mechanisms, for example: fiber rupture, matrix crack and delamination; so, the fraction of absorbed energy is very high (over 75%).

At the region of maximum point in Figure 7.28, the plate is at the perforation onset. The critical energy for perforation of 3mm thickness is calculated by equation

$$y = -0.8743x^3 + 8.7243x^2 - 20.197x + 16.594 \quad \text{Eq. 7.3}$$

where y expresses absorbed energy value and x equals ratio of impact energy level to number of layers. The equation was obtained using fitted curve from experimental data. Also the thickness parameter effects on absorbed energy, the thicker plates absorb less energy, consequently damage will be less than the thin specimens. This method can be implemented for the other composites to determine the saturation energy at the perforation threshold moment.

7.5 Effect of damage on residual tensile properties of GFRP

Tensile residual properties were evaluated after low velocity impact. It is found that the residual tensile properties are decreased progressively as impact energies are increased. This is in consistent with the observation of matrix damage including cracking, debonding and delamination accompanied by fiber breakage. However, the matrix damage would not have a significant effect on the fiber dominated [0/90°] layup since the 0° fibers carrying most of the load remain undamaged. On the other hand, the

fiber breakage caused by higher impact energies would start to affect the laminate, leading to degradation in the residual tensile properties.

Since the development of damage in composites is mostly distributed throughout the specimen it is difficult to monitor the rate of progression. However it can be generally observed in the glass fiber reinforced laminate, as load controlled fatigue cycling progressed, matrix cracking occurred and so the modulus decreased, leading to higher strain values and hence further matrix damage. The fatigue failure mechanism observed was a local progressive failure of the matrix resulting in delamination and final failure by fiber breakage. Matrix cracking, delamination and crack propagation are believed to be the basic damage mechanism in brittle cross-ply composites (Gassan, 2002; Ladeveze et al., 1992; Van Den Oever et al., 1998). Besides the impact damage is in macro-scale. Final failure of the samples under fatigue loading was always a tensile failure initiated at the impact damage area. The final failure crack would propagate perpendicularly across the laminate to both edges. Typical failures can be seen in Figure 7.29, which shows the edges of failed samples.

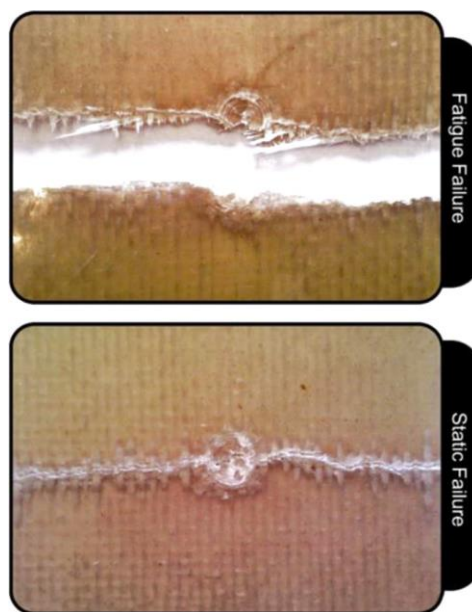


Figure 7.29. Typical failures in GFRP laminates for tension static and fatigue tests.

7.6 The Effects of Impact Energy and Thickness on Fatigue Life of GFRP samples

Fatigue life was assessed for non-impacted and impacted laminates with initial contact energies of 9.8J and 19.6J. Constant stress ratio $R=0$ and stress amplitude of 0.78 of yield stress value in 0.2% strain. Yield stress was chosen as an alternative to ultimate strength due to the brittle behavior of these laminates; if ultimate strength were used for impacted composites, the specimens would fail after few cycles and consequently prediction would not be feasible. The fatigue life of low cycles by initial impact energy is shown in Figure 7.30 for woven fiber laminates.

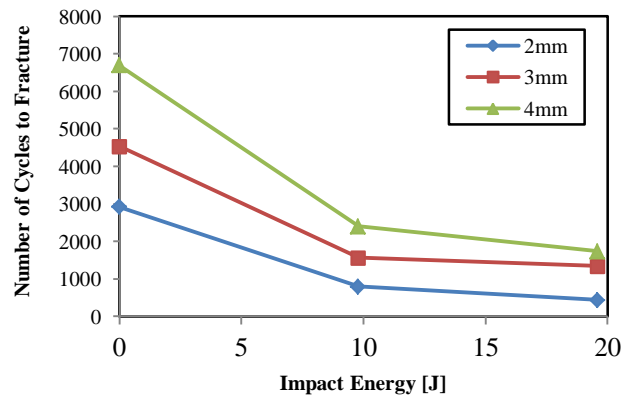


Figure 7.30. Number of cycles to fracture to initial impact energy for different GFRP laminate thicknesses.

Figure 7.30 indicates that the lifespan of glass/epoxy laminate rises when thickness increases, but it decreases drastically in a considerable slope for the samples under low-velocity impact loading. The percentages of life reduction for the damaged plates with initial impact energy of 10J are 72, 65 and 64% for 2, 3 and 4mm thickness, respectively; the trend and curve slopes are approximately similar for all thicknesses.

Figure 7.31 demonstrates that sample life varies linearly with thickness for varying initial energy levels. Curve slope increases with decreasing impact energy, as the amount of impact damage significantly affects the fatigue strength of laminated plates.

The number of cycles to failure for the damaged samples below 9.8 and 19.6J impact energies range from 433 up to 2400, which is less than for non-damaged laminates (2920-6690 cycles) (Figure 7.31). According to Figure 7.30 and Figure 7.31, low-velocity impact has significant influence with over 50% even for thick plates. This means that the fatigue behavior of GFRP composites is mostly characterized by low-velocity impact energy as opposed to thickness.

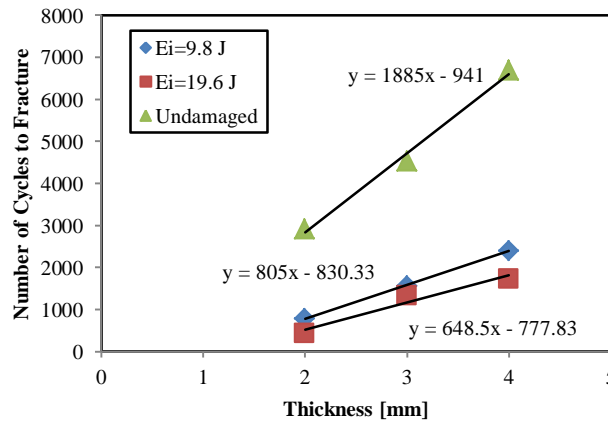


Figure 7.31. Specimen life varies with thickness for different initial impact energy values.

7.7 Modification of the failure criteria of GFRP under low-velocity impact

According to Halverson's damage accumulation relationship and Broutman's linear model, FD in this study is defined as the amount of *Damage Fatigue* as follows:

$$FD = (1 - F_a) \left(\frac{n}{N} \right) \quad \text{Eq. 7.4}$$

FD is the damage index for fatigue, and the results show that F_a is 0.75 for these fatigue tests. The residual strength is predicted by FD after n cycles. The amount of $(1 - F_a/N)$ indicates the slope of FD and it is illustrated for different thicknesses and impact energy levels in Figure 7.32.

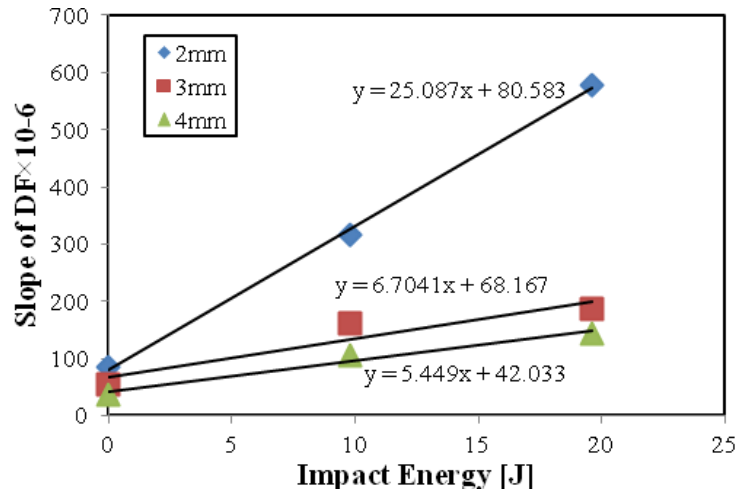


Figure 7.32. FD slope variations to impact energy for different thicknesses.

Figure 7.32 indicates that the *FD* slope changes linearly with impact energy; therefore, the value of *FD* is obtained from only two fatigue tests on GFRP laminates. The plate with 2mm thickness has a higher slope, while the plates with 3 and 4mm thickness have equal slopes since thinner plates are more susceptible to impact damage. The amount of sloping may be indicative of damage intensity.

The damage index of fatigue, and consequently, the final residual strength are calculated from Eq. 7.5 as a function of initial impact energy level. This equation expresses the direct effect of low-velocity impact on fatigue strength at high stress amplitude and tensile mode loading.

$$FD = (cE_i + d)n \quad \text{Eq. 7.5}$$

where *c* and *d* are constant coefficients obtained from the fatigue test.

The experimental results of damage growth show that there are two different stages during the damage progress in non-impact and impacted composites under fatigue loading. During the first stage, the damage spreads slowly with constant rate. During the second stage, the damage starts to grow rapidly due to the fracture of fibers. Again data plotted in Figure 7.32 represents variations of *FD* with impact energy and

laminate thickness when $n=1$. The low value of FD for the non-impact laminates at single cycle indicates that damage including matrix cracking is not contributing much since the fibers along load direction mostly carry fatigue loading. Once fatigue damage value increases, damage is observed in form of delamination, fiber debonding and finally fractures of fibers. Then from the slope of FD curve, the amount of fatigue damage can be easily inferred for any loading cycle n and the damage mode can be detected.

7.8 Effective stress-strain correlation with damage index

A function for the effective stress can be defined using the applied stress and the damage index. The effective stress, σ_{eff} , is obtained for one dimensional stress state by Eq. 7.5 and Eq. 7.6:

$$\sigma_{eff} = \frac{1}{1 - FD} \sigma \quad \text{Eq. 7.6}$$

For two dimensional plane-stress problems, the effective stress vector, $\{\sigma_{eff}\}$, can be expressed as:

$$\{\sigma_{eff}\} = [M]\{\sigma\} \quad \text{Eq. 7.7}$$

Where $\{\sigma\} = \{\sigma_1 \ \sigma_2 \ \tau_{12}\}^T$ are the stress components in the principal orthotropic directions. There is a transformation matrix, which correlates the stress (damaged laminates) to the effective stress (virgin composites). In terms of isotropic and in-plane damage model, the matrix can be written as:

$$[M] = \begin{bmatrix} \frac{1}{1-FD} & 0 & 0 \\ 0 & \frac{1}{1-FD} & 0 \\ 0 & 0 & \frac{1}{1-FD} \end{bmatrix} \quad \text{Eq. 7.8}$$

In order to derive the constitutive equation, for plane stress conditions the effective stress-strain at a local ply or lamina level can be defined as

$$\{\varepsilon\} = [H_0]\{\sigma_{eff}\} \quad \text{Eq. 7.9}$$

where $[H_0]$ is the original compliance matrix for an orthotropic lamina and $\{\varepsilon\} = \{\varepsilon_1 \ \varepsilon_2 \ \varepsilon_3\}^T$ are the strain components. Considering Eq. 7.7 and Eq. 7.9 it can be written the compliance relationship for the damaged state:

$$\{\varepsilon\} = [H_0][M]\{\sigma\} = [H]\{\sigma\} \quad \text{Eq. 7.10}$$

where

$$[H] = \begin{bmatrix} \frac{1}{(1-FD)E_1^0} & -\frac{\nu_{12}^0}{E_1^0} & 0 \\ -\frac{\nu_{21}^0}{E_2^0} & \frac{1}{(1-FD)E_2^0} & 0 \\ 0 & 0 & \frac{1}{(1-FD)G_{12}^0} \end{bmatrix} \quad \text{Eq. 7.11}$$

and for orthotropic material the equation, $\frac{\nu_{12}^0}{E_1^0} = \frac{\nu_{21}^0}{E_2^0}$, can be assumed. For $[H]$ all the elastic parameters are the usual elasticity constants of undamaged lamina.

The effective constitutive matrix, $[C]$, which is a function of the undamaged elastic constants and the damage index, FD , can be obtained by:

$$\begin{aligned}
[C] &= [H]^{-1} \\
&= \frac{1}{D} \begin{bmatrix} (1-FD)E_1^0 & (1-FD)^2\nu_{21}^0E_2^0 & 0 \\ (1-FD)^2\nu_{12}^0E_1^0 & (1-FD)E_2^0 & 0 \\ 0 & 0 & D(1-FD)G_{12}^0 \end{bmatrix}
\end{aligned} \tag{Eq. 7.12}$$

where

$$D = 1 - (1 - FD)^2\nu_{12}^0\nu_{21}^0 \tag{Eq. 7.13}$$

The matrices $[C]$ and $[H]$ are still positive as the amount of FD is less than unity, and $D > 0$. Therefore, it can be concluded that energetically the system remains stable.

7.9 Effective failure criteria based on damage index

The failure based on a maximum stress criterion is predicted using interactive terms considered for the matrix subjected damage modes but not for the fiber subjected longitudinal damage. For the failure equations, similar form of Hashin's criteria (Hashin, 1980) is used as:

$$Fibre\ failure: \left(\frac{\sigma_{eff,1}}{X_{c,t}} \right)^2 - 1 \begin{cases} \geq 0 & failed \\ < 0 & elastic \end{cases} \tag{Eq. 7.14}$$

$$Matrix\ failure: \left(\frac{\sigma_{eff,2}}{Y_{c,t}} \right)^2 + \left(\frac{\tau_{eff,12}}{S} \right)^2 - 1 \begin{cases} \geq 0 & failed \\ < 0 & elastic \end{cases} \tag{Eq. 7.15}$$

where the subscripts c and t show tensile and compressive components respectively. It should be noted that for the tensile state the amount of stress is positive and if this amount is negative, it follows the compressive state.

Eq. 7.14 and Eq. 7.15 are indirect function of damage value FD since σ_{eff} and τ_{eff} are including FD parameter. The difference between Hashin's criteria and the proposed equations is failure of GFRP is finally a function of damage index rather than only the stress value.

7.10 S-N Curve

A laminate with a thickness of 2 mm was considered for evaluating the $S-N$ curve. Fatigue tests were carried out on virgin and impacted plates. Figure 7.33 demonstrates the $S-N$ curve for different energy levels. According to Eq. 2.1, a line has been fitted from experimental data.

The linear relationship satisfies the laminate's fatigue behavior. From this curve it is also possible to calculate m and b . The values of m for the impact energies of 0, 9.8 and 19.6J are -35, -35 and -46, respectively, which are amounts equivalent to the non-perforated laminates. The m and b values are shown in Table 7.4. It is clear that the value of b for impacted composites is less than for non-impacted plates; therefore, it is obvious that impact damage significantly affects the $S-N$ curve.

If it is taken logarithm of both sides of Eq. 2.2 as:

$$\log S = b_1 + m_1 \log N \quad \text{Eq. 7.16}$$

where b_1 and m_1 are defined as:

$$\begin{cases} b_1 = \frac{\log k_1}{k_2} \\ m_1 = -\frac{1}{k_2} \end{cases} \quad \text{Eq. 7.17}$$

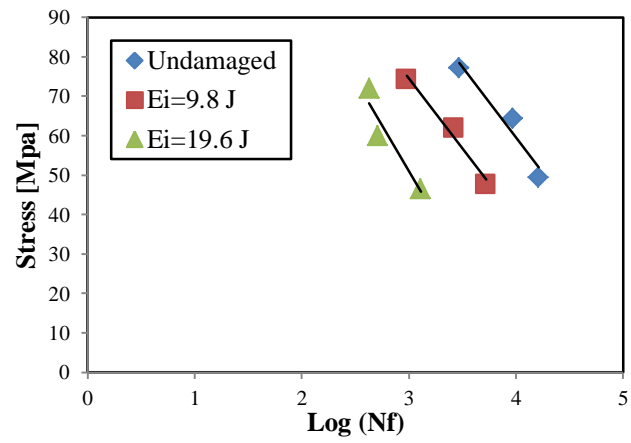


Figure 7.33. The stress-fatigue life curve for woven E-glass/epoxy with 2mm thickness.

Table 7.4: Lamina stiffness and strength properties of GFRP (Hosseinzadeh et al., 2006).

Initial impact energy [J]	m	b
0 (Undamaged)	35	202.3
9.8	35	180.8
19.6	46	191.5

CHAPTER 8: CONCLUSION AND SUGGESTION FOR FURTHER WORK

The mechanical behavior of GFRP composite and HA, which represent two types of brittle biomaterials were determined using experimental, semi-empirical and numerical methods. The most significant conclusions and suggestions for future work are mentioned in this chapter.

8.1 Conclusion

The mechanical properties of HA were identified with not only elastoplastic material model but also irregular porous geometrical model. The solid models besides the porous models were considered to represent the influence of porosity through the numerical results.

The extraction of the elastoplastic properties of hydroxyapatite from nanoindentation tests has been studied by analytical means, direct FE model and inverse FE technique for the solid structure. The nanoindentation experiments were carried out at various sintering temperatures. FE solution-based force and displacement control were validated by experimental results. The inverse technique and analytical method predicted good estimation of hardening parameters. The plastic properties of hydroxyapatite were calculated with the proposed algorithm presented in chapter 5. HA samples showed the highest elastic modulus and hardness at 1200°C, and the numerical model was in good agreement with the experimental results. The work hardening exponent n varied from 0.21 to 0.39 and the strength coefficient ranged from 4.92 to 8.05 GPa. The results show that the sintering temperature is an important factor inducing the phase stability and the hardness of bovine hydroxyapatite ceramics. High temperature sintering at 1200 °C and 1300 °C results in highly crystallized materials, which feature good mechanical properties and lowest porosity. The finite element results were more similar with

nanoindentation experimental data for harder samples, especially for the peak E and K values, whereas the minimum value of n was at 1250 °C.

A proposed method has been presented to create irregular porous structure geometry. Inspired by the random colloid-aggregation model which explains the formation mechanism of random porous media, Voronoi tessellation is first generated to partition the space into a collection of compartments, selective compartments are then merged together to imitate the random colloid-aggregations. Through this Voronoi cell merging, irregular convex and concave polygons are obtained and the vertices of which are modeled as control points of closed B-Spline curves. The fitted B-Spline curves are then employed to represent the boundaries of the irregular-shaped pores.

The proposed representation and modeling method try to mimic the porous geometry which are independent on any pre-existing objects. The method presented a model with computing efficiency consideration and reduction of difficulty. This significantly improved the ease of irregular porous structure modeling while at the same time properly maintained the irregularity that are widely found in natural objects. Compared with other existing CAD modeling approaches, the proposed approach can easily construct porous structures which look natural and realistic. To our knowledge there seems to be no similar methods that can achieve comparable results using such simple approaches.

Elastoplastic material model and irregular porous structure were implemented into FE-model in order to determine the distinction of mechanical behavior for the solid and the porous HA samples. 2D and 3D finite element analysis has been done using the generated porous geometry models for porous HA samples under nanoindentation loading. The numerical results were compared between the solid and the porous geometries. The results revealed that the number and distribution of pores affected on stress distribution through HA model, in other words mechanical response of a structure

depended on porosity. In force-displacement curve this change can be seen on maximum force and indentation depth.

We also demonstrated that combining the proposed representation with stochastic geometry, unlimited generically similar, yet geometrically and topologically different porous structures can be designed with little effort. This non-uniqueness and versatility are advantageous instead of limitations since in the real world there are no exactly similar porous structures (e.g. rocks, sandstones and bones etc.) as well.

The behavior of woven fabric composite laminates under low-velocity impact was experimentally investigated. Bending stiffness, impact force, impact velocity, deflection, and damage were assessed during and after the impact. The experimental results revealed that the response of the glass fiber reinforced plastic laminates (GFRPs) to low-velocity impact is very sensitive to thickness and impact energy level. The results are primarily presented for perforated laminates as well as at the perforation threshold. The damage process was studied by investigating the F-d graph for a range of thicknesses. Variations in bending stiffness and maximum impact force were used to assess the damage to GFRPs. The impact mechanics of fiber glass/epoxy composite under low-velocity were also simulated using MSC.MARC ® MENTAT®. The simulated force-time data was then contrasted against the experimental results. The predicted load carrying capacity was found to be slightly lower than the experimental values, whereas the contact time was overestimated. The result discrepancies are attributed to insufficient information on the real mechanical properties and contact conditions.

Preliminary attempts at predicting the fatigue life of an impact-damage GFRP laminate are described through presenting a fatigue damage model that has been modified for virgin GFRP composites. The fatigue test indicates that the lifespan of laminated composite materials decreases considerably following low-velocity impact.

Increasing the initial impact energy results in a more gradual reduction in the intensity of fatigue life, while the percentage of impact damage effect on the life value obtained is similar to 9.8J of initial energy at high stress amplitudes. Thicker laminates possess higher fatigue strength, but fatigue life decreases drastically subsequent to impact.

The modified model also seems to serve as a valid descriptor of the laminate's fatigue response after sustaining damage due to a low-velocity impact event. Fatigue damage FD is presented to take low-velocity impact for GFRP laminates into consideration when evaluating the fatigue damage value and residual strength after n cycles. Besides, the $S-N$ curve was proposed for the calculation of fatigue life value. A linear relationship governs the $S-N$ curve for GFRP laminates. Fatigue damage index changes linearly and exponentially with impact energy and

In conclusion, the effect of low-velocity impact is momentous and should be considered in the designing stage. Even by increasing laminate thickness, the impact influence is higher than that of thickness on the fatigue behavior of glass/epoxy laminates.

A continuum damage mechanics based model was prepared for the layered composites in form of compliance relationship and failure criterion. The presented modified model can predict damage threshold under impact loading using the absorbed energy and energy level for perforation.

The results presented here are useful not only for hydroxyapatite indentation but also for other mechanical analyses with different loadings on HA. Besides the model can work for HA not only as a bulk material even in a case HA is coated on another material. Although this study was accomplished on a nanoscale, a proper material model (elastoplastic) was characterized in order to implement it to the finite element model for various analyses.

8.2 Suggestions for further work

- For practical bio-application of HA, mechanical properties simulated model could be extended to dynamic loading.
- In order to obtain more accurate results, the non-linear fatigue damage failure can be developed to evaluate the effect of low-velocity impact on GFRP composites. This study needs more number of tests, as the unknown coefficients, which are used in non-linear formula, required more experimental data.
- To discover the effect of multi-impact on damage propagation. Mostly the previous research worked on repeated impact on single point but actually multi impact on different points is more realistic. In this case a pattern for damage propagation can be investigated, plus a comprehensive model is required to calculate damage accumulation.

REFERENCES

- Abdelaal, O. A., & Darwish, S. M. (2013). Review of rapid prototyping techniques for tissue engineering scaffolds fabrication *Characterization and Development of Biosystems and Biomaterials* (pp. 33-54): Springer.
- Abrate, S. (1991). *Impact on laminated composite materials* (Vol. 44).
- Abrate, S. (1991). Impact on laminated composite materials. *Appl Mech Rev*, 44(4), 155-190.
- Acharya, R. C., van der Zee, S. E., & Leijnse, A. (2004). Porosity–permeability properties generated with a new 2-parameter 3D hydraulic pore-network model for consolidated and unconsolidated porous media. *Advances in water resources*, 27(7), 707-723.
- Adachi, T., Osako, Y., Tanaka, M., Hojo, M., & Hollister, S. J. (2006). Framework for optimal design of porous scaffold microstructure by computational simulation of bone regeneration. *Biomaterials*, 27(21), 3964-3972.
- Ahn, J.-H., & Kwon, D. (2001). Derivation of plastic stress-strain relationship from ball indentations: Examination of strain definition and pileup effect. *JOURNAL OF MATERIALS RESEARCH-PITTSBURGH-*, 16(11), 3170-3178.
- Aichholzer, O., Aurenhammer, F., Albers, D., & Gärtner, B. (1996). *A novel type of skeleton for polygons*: Springer.
- Ajdari, A., Babaei, S., & Vaziri, A. (2011a). Mechanical properties and energy absorption of heterogeneous and functionally graded cellular structures. *Procedia Engineering*, 10, 219-223.

Ajdari, A., Nayeb-Hashemi, H., & Vaziri, A. (2011b). Dynamic crushing and energy absorption of regular, irregular and functionally graded cellular structures. *International Journal of Solids and Structures*, 48(3), 506-516.

Ali, M., Qamhiyah, A., Flugrad, D., & Shakoor, M. (2008). Theoretical and finite element study of a compact energy absorber. *Advances in Engineering Software*, 39(2), 95-106.

Ashby, M. (2006). The properties of foams and lattices. *Philosophical Transactions of the Royal Society of London A: Mathematical, Physical and Engineering Sciences*, 364(1838), 15-30.

Banhart, J. (2005). Aluminium foams for lighter vehicles. *International journal of vehicle design*, 37(2), 114-125.

Barrios, M., & Van Sciver, S. (2013). Thermal conductivity of rigid foam insulations for aerospace vehicles. *Cryogenics*, 55, 12-19.

Baucom, J., & Zikry, M. (2005). Low-velocity impact damage progression in woven E-glass composite systems. *Composites Part A: Applied Science and Manufacturing*, 36(5), 658-664.

Beheshty, M., Harris, B., & Adam, T. (1999). An empirical fatigue-life model for high-performance fibre composites with and without impact damage. *Composites Part A: Applied Science and Manufacturing*, 30(8), 971-987.

Belingardi, G., Cavatorta, M. P., & Paolino, D. S. (2008). Repeated impact response of hand lay-up and vacuum infusion thick glass reinforced laminates. *International Journal of Impact Engineering*, 35(7), 609-619.

Belingardi, G., Gugliotta, A., & Vadori, R. (1997). Fragmentation of composite material plates submitted to impact loading: comparison between numerical and experimental results. *Key Engineering Materials*, 144, 75-88.

Bembey, A., Oyen, M., Bushby, A., & Boyde, A. (2006). Viscoelastic properties of bone as a function of hydration state determined by nanoindentation. *Philosophical Magazine*, 86(33-35), 5691-5703.

Bourret, J., Tessier-Doyen, N., Nait-Ali, B., Pennec, F., Alzina, A., Peyratout, C., & Smith, D. (2013). Effect of the pore volume fraction on the thermal conductivity and mechanical properties of kaolin-based foams. *Journal of the European Ceramic Society*, 33(9), 1487-1495.

Briscoe, B., Evans, P., Biswas, S., & Sinha, S. (1996). The hardnesses of poly (methylmethacrylate). *Tribology International*, 29(2), 93-104.

Broutman, L., & Sahu, S. (1972). A new theory to predict cumulative fatigue damage in fiberglass reinforced plastics. *Composite material: Testing and Design, ASTM STP*, 1012, 170.

Bucaille, J.-L., Stauss, S., Felder, E., & Michler, J. (2003). Determination of plastic properties of metals by instrumented indentation using different sharp indenters. *Acta materialia*, 51(6), 1663-1678.

Cai, S., & Xi, J. (2008). A control approach for pore size distribution in the bone scaffold based on the hexahedral mesh refinement. *Computer-aided design*, 40(10), 1040-1050.

Cairns, D. S., & Lagace, P. A. (1992). A consistent engineering methodology for the treatment of impact in composite materials. *Journal of reinforced plastics and composites*, 11(4), 395-412.

Caprino, G., Lopresto, V., Scarponi, C., & Briotti, G. (1999). Influence of material thickness on the response of carbon-fabric/epoxy panels to low velocity impact. *Composites Science and Technology*, 59(15), 2279-2286.

Chang, H., Joo, S. H., & Pak, C. (2007). Synthesis and characterization of mesoporous carbon for fuel cell applications. *Journal of Materials Chemistry*, 17(30), 3078-3088.

Chantarapanich, N., Puttawibul, P., Sucharitpwatskul, S., Jeamwatthanachai, P., Inglam, S., & Sitthiseripratip, K. (2012). Scaffold library for tissue engineering: a geometric evaluation. *Computational and mathematical methods in medicine*, 2012.

Cheah, C., Chua, C., Leong, K., & Chua, S. (2003a). Development of a tissue engineering scaffold structure library for rapid prototyping. Part 1: investigation and classification. *The International Journal of Advanced Manufacturing Technology*, 21(4), 291-301.

Cheah, C., Chua, C., Leong, K., & Chua, S. (2003b). Development of a tissue engineering scaffold structure library for rapid prototyping. Part 2: parametric library and assembly program. *The International Journal of Advanced Manufacturing Technology*, 21(4), 302-312.

Cheah, C.-M., Chua, C.-K., Leong, K.-F., Cheong, C.-H., & Naing, M.-W. (2004). Automatic algorithm for generating complex polyhedral scaffold structures for tissue engineering. *Tissue Engineering*, 10(3-4), 595-610.

Chen, Y., Zhou, S., & Li, Q. (2011). Microstructure design of biodegradable scaffold and its effect on tissue regeneration. *Biomaterials*, 32(22), 5003-5014.

Cheng, Y.-T., & Cheng, C.-M. (1998). Scaling approach to conical indentation in elastic-plastic solids with work hardening. *Journal of Applied Physics*, 84(3), 1284-1291.

Cheng, Y.-T., Li, Z., & Cheng, C.-M. (2002). Scaling relationships for indentation measurements. *Philosophical Magazine A*, 82(10), 1821-1829.

Chester, R. J., & Clark, G. (1992). Modelling of impact damage features in graphite/epoxy laminates.

Ching, W., Rulis, P., & Misra, A. (2009). Ab initio elastic properties and tensile strength of crystalline hydroxyapatite. *Acta Biomaterialia*, 5(8), 3067-3075.

Chou, P., & Croman, R. (1977). Degradation and sudden-death models of fatigue of graphite/epoxy composites. *Composite materials: testing and design, ASTM STP*, 674, 431-454.

Collombet, F., Lalbin, X., & Lataillade, J. (1997). Damage prediction of laminated composites under heavy mass-low velocity impact. *Key Engineering Materials*, 141, 743-776.

Crupi, V., Epasto, G., & Guglielmino, E. (2013). Comparison of aluminium sandwiches for lightweight ship structures: Honeycomb vs. foam. *Marine structures*, 30, 74-96.

Dao, M., Chollacoop, N., Van Vliet, K., Venkatesh, T., & Suresh, S. (2001). Computational modeling of the forward and reverse problems in instrumented sharp indentation. *Acta materialia*, 49(19), 3899-3918.

David-West, O., Nash, D., & Banks, W. (2008). An experimental study of damage accumulation in balanced CFRP laminates due to repeated impact. *Composite Structures*, 83(3), 247-258.

De Giorgi, M., Carofalo, A., Dattoma, V., Nobile, R., & Palano, F. (2010). Aluminium foams structural modelling. *Computers & structures*, 88(1), 25-35.

De Groot, K. (1980). Bioceramics consisting of calcium phosphate salts. *Biomaterials*, 1(1), 47-50.

De Moraes, W., Monteiro, S., & d'Almeida, J. (2005). Evaluation of repeated low energy impact damage in carbon–epoxy composite materials. *Composite structures*, 67(3), 307-315.

Derby, B. (2012). Printing and prototyping of tissues and scaffolds. *Science*, 338(6109), 921-926.

Enab, T. A., & Bondok, N. E. (2013). Material selection in the design of the tibia tray component of cemented artificial knee using finite element method. *Materials & Design*, 44, 454-460.

Evans, R. E., & Masters, J. E. (1987). A new generation of epoxy composites for primary structural applications: materials and mechanics. *ASTM STP*, 937, 413-421.

Farley, G. L., & Jones, R. M. (1992). Prediction of the energy-absorption capability of composite tubes. *Journal of Composite Materials*, 26(3), 388-404.

Findik, F. (2012). Improvements in spinodal alloys from past to present. *Materials & Design*, 42, 131-146.

Fischer-Cripps, A. C. (2011). *Nanoindentation*: Springer Science & Business Media.

Fortune, S. (1987). A sweepline algorithm for Voronoi diagrams. *Algorithmica*, 2(1-4), 153-174.

Gabbrielli, R., Turner, I., & Bowen, C. R. (2008). Development of modelling methods for materials to be used as bone substitutes. *Key Engineering Materials*, 361, 903-906.

Gassan, J. (2002). A study of fibre and interface parameters affecting the fatigue behaviour of natural fibre composites. *Composites Part A: Applied Science and Manufacturing*, 33(3), 369-374.

German, R. M. (1984). Powder metallurgy science. *Metal Powder Industries Federation*, 105 College Rd. E, Princeton, N. J. 08540, U. S. A, 1984. 279.

German, R. M. (2005). *Powder metallurgy and particulate materials processing: the processes, materials, products, properties, and applications*: Metal powder industries federation Princeton, NJ.

Giannakopoulos, A., Larsson, P.-L., & Vestergaard, R. (1994). Analysis of Vickers indentation. *International Journal of Solids and Structures*, 31(19), 2679-2708.

Gibson, L. J., & Ashby, M. F. (1997). *Cellular Solids: Structure and Properties*.

Gökçe, A., Findık, F., & Kurt, A. O. (2011). Microstructural examination and properties of premixed Al–Cu–Mg powder metallurgy alloy. *Materials Characterization*, 62(7), 730-735.

Goller, G., Oktar, F., Agathopoulos, S., Tulyaganov, D., Ferreira, J., Kayali, E., & Peker, I. (2006). Effect of sintering temperature on mechanical and microstructural properties of bovine hydroxyapatite (BHA). *Journal of sol-gel science and technology*, 37(2), 111-115.

Gomez, C., Shokoufandeh, A., & Sun, W. (2007). Unit-cell based design and modeling in tissue engineering applications. *Computer-Aided Design and Applications*, 4(5), 649-659.

Gottesman, T., & Girshovich, S. (1997). Impact damage assessment and mechanical degradation of composites. *Key Engineering Materials*, 141, 3-18.

Guillén, T., Zhang, Q.-H., Tozzi, G., Ohrndorf, A., Christ, H.-J., & Tong, J. (2011). Compressive behaviour of bovine cancellous bone and bone analogous materials, microCT characterisation and FE analysis. *Journal of the mechanical behavior of biomedical materials*, 4(7), 1452-1461.

Halford, G. R., Lerch, B. A., Saltsman, J. F., & Arya, V. K. (1993). Proposed framework for thermomechanical fatigue (TMF) life prediction of metal matrix composites (MMCs). *Thermomechanical fatigue behavior of materials, ASTM STP*, 1186, 176-194.

Halverson, H. G., Curtin, W. A., & Reifsnider, K. L. (1997). Fatigue life of individual composite specimens based on intrinsic fatigue behavior. *International journal of fatigue*, 19(5), 369-377.

Harris, B., Gathercole, N., Reiter, H., & Adam, T. (1996). Constant-stress fatigue response and life-prediction for carbon-fibre composites. *Progress in durability analysis of composite systems. Rotterdam: Balkema*, 63-73.

Haug, E., & De Rouvray, A. (1993). *Crash response of composite structures*. Paper presented at the Structural Crashworthiness and Failure: Proceedings of the Third International Symposium on Structural Crashworthiness held at the University of Liverpool, England, 14-16 April 1993.

- He, L.-H., Standard, O. C., Huang, T. T., Latella, B. A., & Swain, M. V. (2008). Mechanical behaviour of porous hydroxyapatite. *Acta Biomaterialia*, 4(3), 577-586.
- Helgason, B., Taddei, F., Pálsson, H., Schileo, E., Cristofolini, L., Viceconti, M., & Brynjólfsson, S. (2008). A modified method for assigning material properties to FE models of bones. *Medical engineering & physics*, 30(4), 444-453.
- Herliansyah, M., Hamdi, M., Ide-Ektessabi, A., Wildan, M., & Toque, J. (2009). The influence of sintering temperature on the properties of compacted bovine hydroxyapatite. *Materials Science and Engineering: C*, 29(5), 1674-1680.
- Herrmann, M., Schwarzer, N., Richter, F., Frühauf, S., & Schulz, S. (2006). Determination of Young's modulus and yield stress of porous low-k materials by nanoindentation. *Surface and Coatings Technology*, 201(7), 4305-4310.
- Hollister, S. J. (2005). Porous scaffold design for tissue engineering. *Nature materials*, 4(7), 518-524.
- Hollister, S. J. (2009). Scaffold design and manufacturing: from concept to clinic. *Advanced Materials*, 21(32-33), 3330-3342.
- Hosseinzadeh, R., Shokrieh, M. M., & Lessard, L. (2006). Damage behavior of fiber reinforced composite plates subjected to drop weight impacts. *Composites Science and Technology*, 66(1), 61-68.
- Huber, O., & Klaus, H. (2009). Cellular composites in lightweight sandwich applications. *Materials Letters*, 63(13), 1117-1120.
- Hutmacher, D. W., Sittinger, M., & Risbud, M. V. (2004). Scaffold-based tissue engineering: rationale for computer-aided design and solid free-form fabrication systems. *TRENDS in Biotechnology*, 22(7), 354-362.

- Ilyushin, A. (1973). *Mechanics of a Continuous Medium*: DTIC Document.
- Inami, T., Tanimoto, Y., Minami, N., Yamaguchi, M., & Kasai, K. (2015). Color stability of laboratory glass-fiber-reinforced plastics for esthetic orthodontic wires. *The Korean Journal of Orthodontics*, 45(3), 130-135.
- Jacobs, J., Sumner, D., & Galante, J. (1993). Mechanisms of bone loss associated with total hip replacement. *The Orthopedic clinics of North America*, 24(4), 583-590.
- JCPDS File No. 9-432 (hydroxyapatite), P. D. (1988). Joint committee on powder diffraction standards *ASTM, Philadelphia, Pa* (pp. 9-185).
- Jinawath, S., Polchai, D., & Yoshimura, M. (2002). Low-temperature, hydrothermal transformation of aragonite to hydroxyapatite. *Materials Science and Engineering: C*, 22(1), 35-39.
- Joschek, S., Nies, B., Krotz, R., & Göpferich, A. (2000). Chemical and physicochemical characterization of porous hydroxyapatite ceramics made of natural bone. *Biomaterials*, 21(16), 1645-1658.
- Joseph, E., & Perreux, D. (1994). Fatigue behaviour of glass-fibre/epoxy-matrix filament-wound pipes: tension loading tests and results. *Composites Science and Technology*, 52(4), 469-480.
- Kachanov, L. (1986). *Introduction to continuum damage mechanics* (Vol. 10): Springer.
- Kaur, J., Sharma, N., & Singh, H. (2012). In vitro evaluation of glass fiber post. *Journal of clinical and experimental dentistry*, 4(4), e204.

Kim, J.-S., & Chung, S.-K. (2007). A study on the low-velocity impact response of laminates for composite railway bodyshells. *Composite structures*, 77(4), 484-492.

Kim, T.-W., & Solovyov, L. A. (2006). Synthesis and characterization of large-pore ordered mesoporous carbons using gyroidal silica template. *Journal of Materials Chemistry*, 16(15), 1445-1455.

Kindervater, C., Johnson, A., Kohlgrüber, D., Lützenburger, M., & Pentecôte, N. (2000). *Crash and impact simulation of aircraft structures—hybrid and FE based approaches*. Paper presented at the European congress on computational methods in applied sciences and engineering, Proceedings of the ECCOMAS.

Kiselev, A., & Yumashev, M. (1990). Deformation and failure under impact loading. model of a thermoelastoplastic medium. *Journal of Applied Mechanics and Technical Physics*, 31(5), 775-782.

Komlev, V., Peyrin, F., Mastrogiacomo, M., Cedola, A., Papadimitropoulos, A., Rustichelli, F., & Cancedda, R. (2006). Kinetics of in vivo bone deposition by bone marrow stromal cells into porous calcium phosphate scaffolds: an X-ray computed microtomography study. *Tissue Engineering*, 12(12), 3449-3458.

Kondaurov, V. (1988). Continual fracture of non-linearly elastic bodies. *Journal of Applied Mathematics and Mechanics*, 52(2), 237-243.

Kostopoulos, V., Markopoulos, Y., Giannopoulos, G., & Vlachos, D. (2002). Finite element analysis of impact damage response of composite motorcycle safety helmets. *Composites Part B: Engineering*, 33(2), 99-107.

Krishnamurthy, D., Johansson, E. O., Lee, J. W., & Kjeang, E. (2011). Computational modeling of microfluidic fuel cells with flow-through porous electrodes. *Journal of Power Sources*, 196(23), 10019-10031.

Kumar, R., Prakash, K., Cheang, P., & Khor, K. (2005). Microstructure and mechanical properties of spark plasma sintered zirconia-hydroxyapatite nano-composite powders. *Acta materialia*, 53(8), 2327-2335.

Ladeveze, P., & LeDantec, E. (1992). Damage modelling of the elementary ply for laminated composites. *Composites Science and Technology*, 43(3), 257-267.

Larsson, P.-L., Giannakopoulos, A., Söderlund, E., Rowcliffe, D., & Vestergaard, R. (1996). Analysis of Berkovich indentation. *International Journal of Solids and Structures*, 33(2), 221-248.

Latour, R. A., & Black, J. (1993). Development of FRP composite structural biomaterials: Fatigue strength of the fiber/matrix interfacial bond in simulated in vivo environments. *Journal of Biomedical Materials Research*, 27(10), 1281-1291.

Leong, K., Chua, C., Sudarmadji, N., & Yeong, W. (2008). Engineering functionally graded tissue engineering scaffolds. *Journal of the mechanical behavior of biomedical materials*, 1(2), 140-152.

Li, Z., Yu, J., & Guo, L. (2012). Deformation and energy absorption of aluminum foam-filled tubes subjected to oblique loading. *International Journal of Mechanical Sciences*, 54(1), 48-56.

Mamalis, A., Manolakos, D., Ioannidis, M., & Papapostolou, D. (2006). The static and dynamic axial collapse of CFRP square tubes: finite element modelling. *Composite structures*, 74(2), 213-225.

Mao, H., & Mahadevan, S. (2002). Fatigue damage modelling of composite materials. *Composite Structures*, 58(4), 405-410.

Mercer, C., He, M. Y., Wang, R., & Evans, A. G. (2006). Mechanisms governing the inelastic deformation of cortical bone and application to trabecular bone. *Acta Biomaterialia*, 2(1), 59-68.

Metsger, D., Rieger, M., & Foreman, D. (1999). Mechanical properties of. *Journal of Materials Science: Materials in Medicine*, 10(1), 9-17.

Meyer, U., Handschel, J., Meyer, T., & Wiesmann, H. P. (2009). *Fundamentals of tissue engineering and regenerative medicine*: Springer.

Michailidis, N., Stergioudi, F., Omar, H., & Tsipas, D. (2010a). FEM modeling of the response of porous Al in compression. *Computational Materials Science*, 48(2), 282-286.

Michailidis, N., Stergioudi, F., Omar, H., & Tsipas, D. (2010b). An image-based reconstruction of the 3D geometry of an Al open-cell foam and FEM modeling of the material response. *Mechanics of materials*, 42(2), 142-147.

Mikkor, K., Thomson, R., Herszberg, I., Weller, T., & Mouritz, A. (2006). Finite element modelling of impact on preloaded composite panels. *Composite structures*, 75(1), 501-513.

Mitrevski, T., Marshall, I., Thomson, R., Jones, R., & Whittingham, B. (2005). The effect of impactor shape on the impact response of composite laminates. *Composite structures*, 67(2), 139-148.

Mitrovic, M., Hahn, H. T., Carman, G. P., & Shyprykevich, P. (1999). Effect of loading parameters on the fatigue behavior of impact damaged composite laminates. *Composites Science and Technology*, 59(14), 2059-2078.

Murr, L., Amato, K., Li, S., Tian, Y., Cheng, X., Gaytan, S., . . . Wicker, R. (2011). Microstructure and mechanical properties of open-cellular biomaterials prototypes for total knee replacement implants fabricated by electron beam melting. *Journal of the mechanical behavior of biomedical materials*, 4(7), 1396-1411.

Murugan, R., Kumar, T. S., & Rao, K. P. (2002). Fluorinated bovine hydroxyapatite: preparation and characterization. *Materials letters*, 57(2), 429-433.

Naderi, S., Hassan, M., & Bushroa, A. (2015). Alternative methods to determine the elastoplastic properties of sintered hydroxyapatite from nanoindentation testing. *Materials & Design*, 67, 360-368.

Naik, N., & Shirao, P. (2004). Composite structures under ballistic impact. *Composite structures*, 66(1), 579-590.

Naumann, M., Koelpin, M., Beuer, F., & Meyer-Lueckel, H. (2012). 10-year Survival Evaluation for Glass-fiber-supported Postendodontic Restoration: A Prospective Observational Clinical Study. *Journal of Endodontics*, 38(4), 432-435.

Nicholas, T. (1995). An approach to fatigue life modeling in titanium-matrix composites. *Materials Science and Engineering: A*, 200(1), 29-37.

Okabe, A., Boots, B., Sugihara, K., & Chiu, S. N. (2009). *Spatial tessellations: concepts and applications of Voronoi diagrams* (Vol. 501): John Wiley & Sons.

Oliver, W. C., & Pharr, G. M. (1992a). Improved technique for determining hardness and elastic modulus using load and displacement sensing indentation experiments. *Journal of Materials Research*, 7(6), 1564-1583.

Oliver, W. C., & Pharr, G. M. (1992b). An improved technique for determining hardness and elastic modulus using load and displacement sensing indentation experiments. *Journal of materials research*, 7(06), 1564-1583.

Oliver, W. C., & Pharr, G. M. (2004). Measurement of hardness and elastic modulus by instrumented indentation: Advances in understanding and refinements to methodology. *Journal of Materials Research*, 19(01), 3-20.

Ooi, C., Hamdi, M., & Ramesh, S. (2007). Properties of hydroxyapatite produced by annealing of bovine bone. *Ceramics international*, 33(7), 1171-1177.

Park, H., & Kong, C. (2013). Experimental study on barely visible impact damage and visible impact damage for repair of small aircraft composite structure. *Aerospace Science and Technology*.

Pasko, A., Fryazinov, O., Vilbrandt, T., Fayolle, P.-A., & Adzhiev, V. (2011). Procedural function-based modelling of volumetric microstructures. *Graphical Models*, 73(5), 165-181.

Pearce, P. (1990). *Structure in Nature is a Strategy for Design*.

Pereira, J. R., do Valle, A. L., Ghizoni, J. S., Lorenzoni, F. C., Ramos, M. B., & dos Reis SÓ, M. V. (2013). Push-out bond strengths of different dental cements used to cement glass fiber posts. *The Journal of prosthetic dentistry*, 110(2), 134-140.

Podshivalov, L., Fischer, A., & Bar-Yoseph, P. (2011). 3D hierarchical geometric modeling and multiscale FE analysis as a base for individualized medical diagnosis of bone structure. *Bone*, 48(4), 693-703.

Prokopiev, O., & Sevostianov, I. (2006). Dependence of the mechanical properties of sintered hydroxyapatite on the sintering temperature. *Materials Science and Engineering: A*, 431(1), 218-227.

Rabotnov, Y. N. (1979). Mechanics of deformable solids: Nauka, Moscow.

Raj, S. V. (2011). Microstructural characterization of metal foams: An examination of the applicability of the theoretical models for modeling foams. *Materials Science and Engineering: A*, 528(15), 5289-5295.

Reifsnider, K., Case, S., & Duthoit, J. (2000). The mechanics of composite strength evolution. *Composites Science and Technology*, 60(12), 2539-2546.

Ren, L.-M., Todo, M., Arahira, T., Yoshikawa, H., & Myoui, A. (2012). A comparative biomechanical study of bone ingrowth in two porous hydroxyapatite bioceramics. *Applied Surface Science*, 262, 81-88.

Requicha, A. A., & Voelcker, H. B. (1982). Solid Modeling: A Historical Summary and Contemporary Assessment. *IEEE Computer Graphics and Applications*, 2(2), 9-24.

Ross, C., & Sierakowski, R. (1973). Studies on the impact resistance of composite plates. *Composites*, 4(4), 157-161.

Sanz-Herrera, J., García-Aznar, J., & Doblaré, M. (2009). On scaffold designing for bone regeneration: a computational multiscale approach. *Acta Biomaterialia*, 5(1), 219-229.

Schaefer, D. W., & Keefer, K. D. (1986). Structure of random porous materials: silica aerogel. *Physical review letters*, 56(20), 2199.

Scheffler, M., & Colombo, P. (2006). *Cellular ceramics: structure, manufacturing, properties and applications*: John Wiley & Sons.

Schroeder, C., Regli, W. C., Shokoufandeh, A., & Sun, W. (2005). Computer-aided design of porous artifacts. *Computer-aided design*, 37(3), 339-353.

Shen, H., & Brinson, L. (2011). A numerical investigation of porous titanium as orthopedic implant material. *Mechanics of materials*, 43(8), 420-430.

Singh, R., Lee, P., Lindley, T., Kohlhauser, C., Hellmich, C., Bram, M., . . . Dashwood, R. (2010). Characterization of the deformation behavior of intermediate porosity interconnected Ti foams using micro-computed tomography and direct finite element modeling. *Acta Biomaterialia*, 6(6), 2342-2351.

Sirivithayapakorn, S., & Keller, A. (2003). Transport of colloids in saturated porous media: A pore-scale observation of the size exclusion effect and colloid acceleration. *Water Resources Research*, 39(4).

Starly, B., Fang, Z., Sun, W., Shokoufandeh, A., & Regli, W. (2005). Three-dimensional reconstruction for medical-CAD modeling. *Computer-Aided Design and Applications*, 2(1-4), 431-438.

Subramanian, S., Reifsnider, K., & Stinchcomb, W. (1995). A cumulative damage model to predict the fatigue life of composite laminates including the effect of a fibre-matrix interphase. *International Journal of Fatigue*, 17(5), 343-351.

Suchanek, W., & Yoshimura, M. (1998). Processing and properties of hydroxyapatite-based biomaterials for use as hard tissue replacement implants. *Journal of Materials Research*, 13(01), 94-117.

Sun, W., Darling, A., Starly, B., & Nam, J. (2004). Computer-aided tissue engineering: overview, scope and challenges. *Biotechnology and applied biochemistry*, 39(1), 29-47.

Sun, W., & Lal, P. (2002). Recent development on computer aided tissue engineering—a review. *Computer methods and programs in biomedicine*, 67(2), 85-103.

Sun, W., Starly, B., Nam, J., & Darling, A. (2005). Bio-CAD modeling and its applications in computer-aided tissue engineering. *Computer-aided design*, 37(11), 1097-1114.

Symons, D. D., & Davis, G. (2000). Fatigue testing of impact-damaged T300/914 carbon-fibre-reinforced plastic. *Composites Science and Technology*, 60(3), 379-389.

Tai, N., Ma, C., Lin, J., & Wu, G. (1999). Effects of thickness on the fatigue-behavior of quasi-isotropic carbon/epoxy composites before and after low energy impacts. *Composites Science and Technology*, 59(11), 1753-1762.

Teoh, S., & Chui, C. (2008). Bone material properties and fracture analysis: Needle insertion for spinal surgery. *Journal of the mechanical behavior of biomedical materials*, 1(2), 115-139.

Tita, V., De Carvalho, J., & Vandepitte, D. (2008). Failure analysis of low velocity impact on thin composite laminates: Experimental and numerical approaches. *Composite Structures*, 83(4), 413-428.

Tsamasphyros, G. J., & Bikakis, G. S. (2013). Analytical modeling to predict the low velocity impact response of circular GLARE fiber-metal laminates. *Aerospace Science and Technology*.

Uda, N., Ono, K., & Kunoo, K. (2009). Compression fatigue failure of CFRP laminates with impact damage. *Composites Science and Technology*, 69(14), 2308-2314.

Van den Oever, M., & Peijs, T. (1998). Continuous-glass-fibre-reinforced polypropylene composites II. Influence of maleic-anhydride modified polypropylene on fatigue behaviour. *Composites Part A: Applied Science and Manufacturing*, 29(3), 227-239.

Vergés, E., Ayala, D., Grau, S., & Tost, D. (2008). 3D reconstruction and quantification of porous structures. *Computers & Graphics*, 32(4), 438-444.

Vicente, J., Beltrán, F., & Martinez, F. (2000). *Simulation of impact on composite fuselage structures*. Paper presented at the European Congress on Computational Methods in Applied Science and Engineering (ECOMAS), Barcelona.

Wang, J., & Shaw, L. L. (2010). Grain-Size Dependence of the Hardness of Submicrometer and Nanometer Hydroxyapatite. *Journal of the American Ceramic Society*, 93(3), 601-604.

Wang, P. E., & Chaki, T. (1993). Sintering behaviour and mechanical properties of hydroxyapatite and dicalcium phosphate. *Journal of Materials Science: Materials in Medicine*, 4(2), 150-158.

Weight, T. F., & Methods, A. T. (2001). Means of a Falling Dart (Tup or Falling Mass) ASTM D 5628-96. *Standard Test Method for Impact Resistance of Falt, Rigid*

Plastic Specimen By Means of a Falling Dart (2001). Annual Book of ASTM Standards, 630-639.

Wettergreen, M., Bucklen, B., Starly, B., Yuksel, E., Sun, W., & Liebschner, M. (2005a). Creation of a unit block library of architectures for use in assembled scaffold engineering. *Computer-aided design*, 37(11), 1141-1149.

Wettergreen, M., Bucklen, B., Sun, W., & Liebschner, M. (2005b). Computer-aided tissue engineering of a human vertebral body. *Annals of biomedical engineering*, 33(10), 1333-1343.

Wong, K. H., Davis, T. P., Barner-Kowollik, C., & Stenzel, M. H. (2007). Honeycomb structured porous films from amphiphilic block copolymers prepared via RAFT polymerization. *Polymer*, 48(17), 4950-4965.

Yang, J. N. (1978). Fatigue and residual strength degradation for graphite/epoxy composites under tension-compression cyclic loadings. *Journal of Composite Materials*, 12(1), 19-39.

Yetkin, S. H., Unal, H., Mimaroglu, A., & Findik, F. (2013). Influence of process parameters on the mechanical and foaming properties of PP polymer and PP/TALC/EPDM composites. *Polymer-Plastics Technology and Engineering*, 52(5), 433-439.

Yoo, D.-J. (2011). Computer-aided porous scaffold design for tissue engineering using triply periodic minimal surfaces. *International Journal of Precision Engineering and Manufacturing*, 12(1), 61-71.

Yuanjian, T., & Isaac, D. (2007). Impact and fatigue behaviour of hemp fibre composites. *Composites Science and Technology*, 67(15), 3300-3307.

Yuanjian, T., & Isaac, D. (2008). Combined impact and fatigue of glass fiber reinforced composites. *Composites Part B: Engineering*, 39(3), 505-512.

Zeleniakienė, D., Griškevičius, P., & Leišis, V. The comparative analysis of 2D and 3D microstructural models stresses of porous polymer materials: ISSN.

Zhang, D., Sun, Y., Chen, L., & Pan, N. (2013). A comparative study on low-velocity impact response of fabric composite laminates. *Materials & Design*.

Zhao, G., & Cho, C. (2007). Damage initiation and propagation in composite shells subjected to impact. *Composite structures*, 78(1), 91-100.

Zhou, G., & Greaves, L. (2000). Damage resistance and tolerance of thick laminated woven roving GFRP plates subjected to low-velocity impact. *Composite Materials and Structures*, 133-183.

Zysset, P. K., Edward Guo, X., Edward Hoffer, C., Moore, K. E., & Goldstein, S. A. (1999). Elastic modulus and hardness of cortical and trabecular bone lamellae measured by nanoindentation in the human femur. *Journal of biomechanics*, 32(10), 1005-1012.

LIST OF PUBLICATIONS

Published Papers

	Title	Year
1	Low-velocity impact damage of woven fabric composites: Finite element simulation and experimental verification	2014
Authors	MA Hassan, S Naderi, AR Bushroa	
Journal	Materials & Design 53, 706-718	
2	An empirical modified fatigue damage model for impacted GFRP laminates	2014
Authors	S Naderi, MA Hassan, AR Bushroa	
Journal	Acta Astronautica 103, 119-128	
3	Alternative Methods to Determine the Elastoplastic Properties of Sintered Hydroxyapatite from Nanoindentation Testing	2015
Authors	S Naderi, MA Hassan, AR Bushroa	
Journal	Materials & Design 67, 360-368	
4	Influence of Pore Size on Effective Mechanical Properties of Porous Hydroxyapatite Bioceramics using Computer-Aided Approach	2015
Authors	S Naderi, MA Hassan, AR Bushroa	
Conference	Cermodel 2015, Modelling and simulation Meet Innovation In ceramics Technology	

Related Published Paper

	Title	Year
1	Effect of curvature and thickness of aluminum shells on the energy absorption in low velocity impact	2012
Authors	MA Hassan, M Hamdi, S Naderi, F Zahedi	
Journal	Advanced Materials Research 488, 40-45	

Papers in Review Process

	Title	Year
1	A study on damage evolution based on absorbed energy in GFRP laminates due to low-velocity impact	2015
Authors	S Naderi, MA Hassan, AR Bushroa	
Journal	Journal of Sains Malaysiana	

Paper to be submitted soon

	Title	Year
1	Study on Effect of Porosity on Mechanical Properties of Hydroxyapatite Using Finite Element Model	2015
Authors	S Naderi, MA Hassan, AR Bushroa	
Journal	-	
2	Evaluation of the effect of Dental Cements on Mechanical Properties of Teeth Restored With Various Dental Posts	2015
Authors	S Naderi, MA Hassan, AR Bushroa	
Journal	-	